Low-spin states in $^{102-108}$Zr in the Interacting Boson Model context

Camino Rodríguez Triguero

Ph.D. 2013

School of Computing, Engineering and Mathematics

University of Brighton

A mi abuelo, Miguel, mi prima, Eva, y Pipo. Os echo de menos.

Abstract

The region of the nuclear chart around A$\sim$100 is an area of structural changes where different shapes coexist and therefore, an interesting place to study structural evolution and test nuclear models. Within the element that populate this region, zirconium is one which is expected to present well deformed states, but for which little experimental data has been measured so far. The structure of the $^{102-108}$Zr nuclei has been studied using the Interacting Boson Model (IBM). Energy states and transition probabilities have been predicted and tested using the limited amount of existing experimental data. However, the results of these calculations produced several possibilities, so knowledge about non-yrast states is needed in order to deepen the understanding of the structural changes in zirconium nuclei. Therefore, a series of experiments to measure non-yrast states of $^{102-108}$Zr are required. A new technique, for separating different states of nuclei, has been developed and tested at the University of Jyväskylä, using the IGISOL III facility for the known case of ^{100}Nb β-decay into ^{100}Mo. This technique has been successfully extended to allow the separate study of the gamma-ray decay of states populated by the different parent states. Lower spin states of $^{102-108}$Zr are populated via beta-decay from $^{102-108}$Y. In order to measure the non-yrast states of $^{102-108}$Zr post-trap online spectroscopy will be used at IGISOL IV. IGISOL IV is the improved version of IGISOL III and is currently under construction. Part of my Ph.D. consisted of helping with the development of IGISOL IV, the improvements of this facility are explained in this thesis alongside its operation and several tests performed during 2012.

Contents

List of Figures

"So you don't have unique answers to your questions?"
"Adson, if I had, I would teach theology in Paris."
"Do they always have a right answer in Paris?"
"Never", said William, "but there they are quite confident of their errors."

Umberto Eco, *Il nome della rosa.*

Acknowledgements

I would like to thank my supervisors; Professors Alison Bruce and Zsölt Podolyàk for their supervision and support. Especially to Professor Bruce, who had the dubious honour of dealing with me almost every day during my PhD (proving she has great patience). I have grown 'fond' of her green pen.

Thanks to all the Nuclear Physics Group of the University of Brighton: Dr Ana M. Denis Bacelar, Dr Oliver J. Roberts, and soon to be Dr Frank Browne for all their help, support and bad jokes. To the rest of the people at the University of Brighton whom I had the luck to work, have coffee, talks, lunch with, and all the things that have made my life funny and interesting.

I would also like to thank all the people working at IGISOL facility between 2009 and 2013. Thank you for welcoming me into your group during the long Finnish winter, and all the other times I have been there. Thank you for teaching me, and give me the opportunity to learn what is like to work in a nuclear physics facility, special mention to the long days of painting and cleaning diffusion oil pumps. In particular I would like to thank Dr Iain Moore, for all his help and support.

Thank you to all the people who have contributed in making me reach this point in my life. Thank you for the good, the bad and ugly.

And, finally, to my parents... A mis padres. Gracias por todo. Por quererme, por cuidarme y por vuestro apoyo, aunque no siempre estéis de acuerdo.

I declare that the research contained in this thesis, unless otherwise formally indicated within the text, is the original work of the author. The thesis has not been previously submitted to this or any other university for a degree, and does not incorporate any material already submitted for a degree.

Camino Rodríguez Triguero

16/07/2013

Chapter 1

Introduction

There are several theoretical models of the atomic nucleus, divided into two main categories: microscopic models, in which the degrees of freedom are those of the particles constituting of the nucleus, and collective models, which describe the properties of the nucleus as a whole. A major question remains in how to reconcile both points of view. How do you explain collective properties from a microscopic point of view? In the search for a better understanding, scientists are currently challenging the limits of nuclear matter stability, pursuing new data which might enlighten the complicated nuclear structure. Exotic-nuclei research has produced an increasing amount of new experimental data, uncovering a wide range of new nuclear behaviour that is not fully understood and, providing a testing ground for nuclear models and highlighting the need for a theory able to explain these exotic configurations.

Some nuclear properties, such as the nucleons' separation energy, exhibit sudden changes at certain numbers of nucleons, indicating the existence of large gaps between energy levels. These "magic numbers" of nucleons, which are more stable configurations, constitute the origin of the shell model [1]. Closed-shell configurations greatly simplify the description of the system, allowing an interpretation in which only valence nucleons are taken into account. The nuclear shell model was developed based on empirical data within a restricted area of the nuclear chart,

close to the stable isotopes. Due to the acquisition of new data on exotic nuclei, the idea of the magic numbers validity across the entire nuclear chart has been disputed in recent years [2, 3, 4]. Therefore, the evolution of shell structure along the nuclear landscape has become one of the main unknowns in nuclear physics.

Away from closed shells, where several valence nucleons exist, other structural representations prevail. Here collective motion dominates, changing the nucleus from a spherical equilibrium shape to a deformed one. Structures are often explainable on the basis of geometric or dynamical symmetries, where the main two archetypes are the harmonic vibrator and the symmetric rotor [5].

Across the nuclear landscape, transitions from spherical to deformed shape occur. Although these transitions are often sudden, an intermediate condition of shape coexistence is also possible. At present there are no simple theoretical models able to describe these regions. In absentia of an appropriate structural framework, the empirical observation is essential. The nucleus is an unique laboratory to examine the quantum basis of shape coexistence, since it can exhibit properties associated with both single-nucleon and collective motion.

The Interacting Boson Model (IBM) [6] treats the nucleus as a system of bosons (pairs of fermions coupled to spin 0 or 2 in its simplest version, IBM-1) and comprises a microscopic description able to explain collective properties. Such a system of bosons, constitutes a unitary group which can undergo different decompositions, leading to three different dynamical symmetries. These limits include rotational and vibrational paradigms, linking with the geometrical model description. Motivated by the shell model, the bosons are interpreted as pairs of nucleons in the valence shell, thus the number of bosons for a given nucleus is fixed and depends on the definition of closed shells. Therefore, in principle, it should be possible to fit neighbouring nuclei using the same Hamiltonian but different numbers of bosons; an approach which has been successful in some cases [7]. The advantage of using the IBM framework is that it provides an easy way to perform calculations for low spin states not only at the three limits, but in the transition between them, examples of which can be found at references: [8, 9, 10].

The region of the nuclear chart A$\sim$100 is one of structural change, where different shapes coexist [11, 12]. Large deformed ground states and shape transitions from nearly spherical to well deformed prolate shapes have been observed in Sr, Zr and Mo [13, 14, 15]. Evidence of triaxiality has also been found in Mo and Ru isotopes [16] while, heavier Sr and Zr isotopes display an axially symmetric well deformed shape. In addition, nuclei in the region as well have long lived isomers [17, 18], providing new opportunities to study unusual nuclear states [19].

This thesis is dedicated to the study of the nuclear structure of $^{102-108}$Zr isotopes. Zirconium nuclei in the A$\sim$100-110 region have been measured to have well-deformed shapes [20], isomeric states [17, 21] and are predicted to exhibit different configurations [22]. Chapter 2 briefly explains the basic nuclear models needed in order to understand the nuclear deformation phenomenon. It also gives an overview of the experimental indicators of deformation and structural evolution in the area of interest. Chapter 3 applies the Interacting Boson Model (IBM) to the study of $^{102-108}$Zr. Given that almost no data is available for $^{104-108}$Zr, the need to acquire new data in order to test and refine, not only the IBM but also, other nuclear models is highlighted. This leads to the last two chapters, which are dedicated to the experimental technique and facility in which Zirconium data will be collected in the future. Chapter 4 focuses on a new technique, for separating different states of nuclei [23], which has been developed and tested at the University of Jyväskylä, using the IGISOL III facility. The isomeric cleaning technique has been extended to allow the separate study of the gamma-ray decay following the β-decay of different parent states and, was tested for the known case of ^{100}Nb decay into ^{100}Mo [18]. It is known that lower spin states of ^{102,108}Zr are populated via beta-decay from ^{102,108}Y [17, 24]. In order to measure the non-yrast states and other structural information, a series of experiments using post-trap online spectroscopy at the IGISOL IV will be performed. Therefore, the last Chapter, 5, is dedicated to IGISOL IV, an upgraded version of the IGISOL III facility. The development of the IGISOL IV facility and its current status, paying particular attention to the work in which the author played a prominent part will be presented.

Chapter 2

Physics Motivation

From the point of view of quantum mechanics, the phenomenon of deformation is a prerequisite to collective rotation. It does not make sense to speak about rotation of a spherical object given that such a system will be invariant under rotations. Nuclear rotation and vibrations, and, therefore, nuclear deformation, are well explained in the context of the geometrical model. Given that the structure of neutron rich zirconium nuclei is known to be well deformed for several isotopes, it is essential to understand the nature of nuclear surface deformation. On the other hand, the zirconium isotopes studied in this thesis, are situated in the shape transition region around A$\sim$100, which shows a structural evolution from spherical to well deformed states. For this reason, the present chapter is focused on two topics: the basics of the collective nuclear model and nuclear deformation, and the structural evolution of the region of interest, with partial emphasis on the experimental and theoretical analysis of the zirconium nuclei.

2.1 Collective nuclear models

Postulated by N. Bohr and Kalckar in 1937 [25], the liquid drop model arose from a comparison between the high density spectrum of sharp resonances, in slow-neutron-capture reactions, and the vibrational modes of a drop of incom-

pressible fluid. As the shell structure of the nucleus was later experimentally demonstrated, the need to reconcile individual particle and collective degrees of freedom lead to the development of the collective model. The description of the nucleus as a collective identity able to undergo vibrations and rotations, was proposed by J. Rainwater [26] and developed by A. Bohr and B. R. Mottelson [5, 27]. This model includes aspects of Shell and liquid drop models, explaining certain electromagnetic properties of the nucleus that previous models had failed to describe.

2.1.1 The vibrational modes of a spherical nucleus

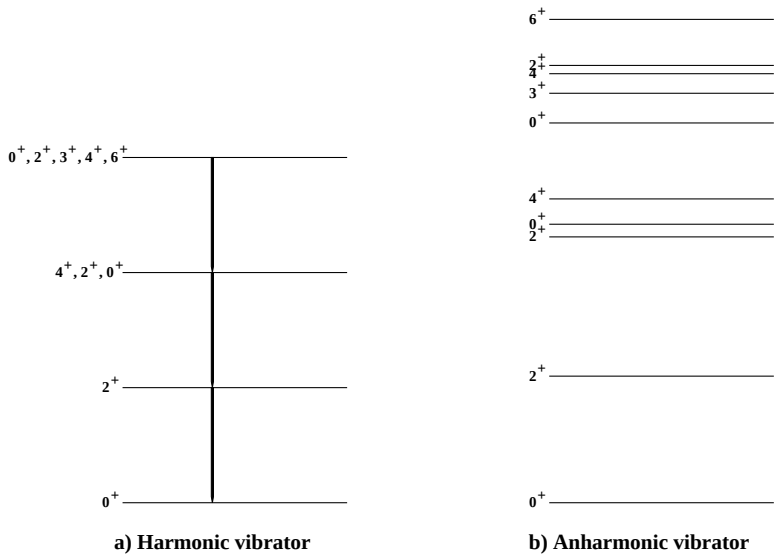

Figure 2.1: Low-lying levels of the: a) harmonic vibrator model; b) anharmonic vibrator model.

Imagine the nucleus as a liquid drop of radius R_0 vibrating with small oscillations around a spherical equilibrium configuration. While the average shape is spherical, the instantaneous form is not. Therefore, one can describe the changes in the nuclear surface, due to the nuclear vibrations, through the following parametrization [28]:

$$R(\theta,\phi) = R_0\left(1 + \sum_{\lambda=0}\sum_{\mu=-\lambda}^{\mu=+\lambda} \alpha^*_{\lambda\mu}(t) Y_{\lambda\mu}(\theta,\phi)\right) \tag{2.1}$$

where λ describes the multipolarity of the shape, R_0 is the radius of the spherical nucleus, $Y_{\lambda\mu}$ are the spherical harmonics and $\alpha_{\lambda\mu}$ are the time-dependent expansion coefficients which describe the vibrations of the nuclei. $\lambda = 0$ corresponds to a compression mode which is at high energy, $\lambda = 1$ do not corresponds to a deformation but to a shift of the center of mass, $\lambda = 2$ represents a quadrupole deformation, $\lambda = 3$ an octupole deformation, etc. As the $\lambda = 0$ component is constant and the $\lambda = 1$ term (dipolar vibration) gives a null average displacement of the centre of mass, the lowest relevant shape component, in terms of deformation, is the quadrupole one, for which the radius can be described by setting $\lambda = 2$ in eq. 2.1 (quadrupole approximation). The vibration quantum is called a phonon by analogy to quantum electrodynamic theory; a single unit of vibrational energy. $\lambda = 1$ is called a dipole phonon and carries one unit of angular momentum, $\lambda = 2$ is a quadrupole phonon and carries two units of angular momentum, etc. Since the quadrupole deformation is the most important one, it is useful to write the Hamiltonian for a quadrupole oscillator. By analogy to the classical harmonic oscillator is possible to write a quantized Hamiltonian as a function of the creation and annihilation operators b_μ and $b^\dagger_\mu$ as follows:

$$\hat{H} = \hbar\omega\left(\sum_{\mu=-2}^{2} b^\dagger_\mu b_\mu + \frac{5}{2}\right). \tag{2.2}$$

Introducing the phonon number operator $\hat{N} = \left(\sum b^\dagger_\mu b_\mu\right)$ with eigenvalue N, the energy spectrum will be given by:

$$E_N = \hbar\omega(N + 5/2), \tag{2.3}$$

Therefore, the ground state is a state with N=0, N=1 corresponds to the first exited state, N=2 corresponds to the second excited state and so on.

For an even-even nucleus adding one phonon ($\lambda = 2$) to the 0^+ ground state, gives only a 2^+ state, adding a second phonon leads to a triplet of states with spins $J^\pi = 0^+, 2^+, 4^+$, etc. Fig. 2.1 shows the level scheme for a typical vibrational nucleus in the cases of a) an harmonic vibrator, which is the case described here and, b) an anharmonic vibrator, which includes two-body residual interactions which have the effect to break the degeneracy of the multiple phonon excitations.

2.1.2 Rotational model and deformed shapes

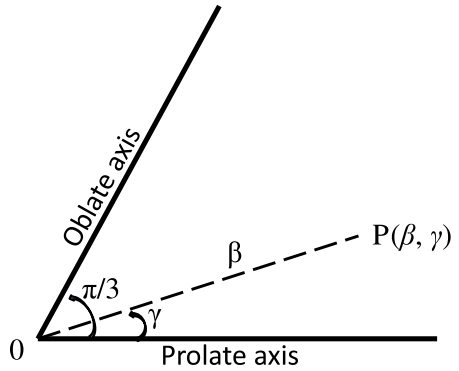

Figure 2.2: The origin of the frame of reference represents the spherical shape, and the point, P, represent an asymmetric deformed nuclear shape. The modulus of the vector OP is the magnitude of the deformation, β, and the angle with respect to the horizontal axis is the asymmetry parameter, γ.

Rotational motion is only observed in nuclei with non-spherical equilibrium shapes, thus the nuclei which present this behaviour are known as deformed nuclei. As

in the case of the vibrational motion the lowest applicable shape component is a quadrupole distortion. Therefore, we shall focus on the case $\lambda = 2$:

$$R = R_0 \left(1 + \sum_{\mu=-2}^{2} \alpha_{2\mu}^{*} Y_{2\mu}(\theta, \phi) \right). \tag{2.4}$$

It is possible to express $\alpha_{2\mu}$ in terms of the Euler angles and two variables β and γ, so that the nuclear shape can be described in a two dimensional β-γ plane, using polar coordinates. Fig 2.2 shows the point P as a function of β, which represents the length of the vector (magnitude of quadrupole deformation), and γ, its angular coordinate (degree of axial symmetry). The variation of the nuclear radius as function of these two parameters can be expressed as follows:

$$\delta R_\kappa = R - R_0 = \sqrt{\tfrac{5}{4\pi}} \beta R_0 \cos(\gamma - \tfrac{\kappa 2\pi}{3}), \quad \kappa = 1, 2, 3. \tag{2.5}$$

Where the indices 1,2 and 3 correspond to the body-fixed frame axes x, y and z. In the case of $\gamma = 0^o$, the nucleus is compressed in the x and y directions and extended in the z direction, assuming what is called a prolate (rugby ball) shape; if $\gamma = 2\pi/3$ and $\gamma = 4\pi/3$, the nucleus is compressed in the y and z directions and extended in the xz and xy planes, respectively, turning into an oblate (disk-like) shape. Both nuclear shapes are shown in fig. 2.3. Note that eq. 2.5 implies that δR_κ is invariant under cyclic permutations of values of γ which are multiples of $\pi/3$ and that γ, $\gamma - 2\pi/3$ and $\gamma - 4\pi/3$ describe the same nuclear surface, and that γ and $-\gamma$ also define the same surface.

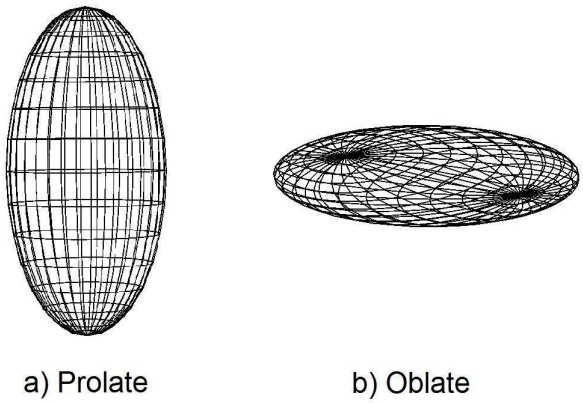

Figure 2.3: Representation of the two different deformed nuclear shapes.

2.1.2.1 Rotational Energies

Consider an axially symmetric nucleus undergoing rotational motion. Such a nucleus will have a total angular momentum, I, which has a projection on the symmetry axis denoted by K. The Hamiltonian for a rigid rotor is:

$$H_{rot} = \sum_{k_i=1}^{3} \frac{\hat{I}^2}{2\mathscr{I}_i}, \tag{2.6}$$

where $\mathscr{I}_i$ is the moment of inertia [29] [30] and k_i are the three directions of the system of reference. If the nucleus is axially symmetric, two moments of inertia are equal and, for K=0 the expectation value of H_{rot} can be written as:

$$E_{rot} = \frac{\hbar^2}{2\mathscr{I}} I(I+1). \tag{2.7}$$

This expression gives the energy of a rotating object in quantum mechanics and can be used to reproduce the energy spectrum of a rotational nucleus. Different

values of I result in different rotational energies of the nucleus. The resulting nuclear states form a sequence called a rotational band. The ground state of an even-even nuclei has a spin-parity of 0^+ and the reflection symmetry of the nuclei imposes even values of I, therefore the energy levels for a rotational nucleus are expected to be:

$$\begin{aligned} E(0^+) &= 0, \\ E(2^+) &= 6\tfrac{\hbar^2}{2\mathscr{I}} \\ E(4^+) &= 20\tfrac{\hbar^2}{2\mathscr{I}} \\ E(6^+) &= 42\tfrac{\hbar^2}{2\mathscr{I}} \end{aligned} \tag{2.8}$$

and so on. The ratio $E(4^+)/E(2^+) \sim 3.3$ is one of the best signatures for rotational motion and deformation, as will be discussed in section 2.2.

2.1.3 Rotations and vibrations of deformed nuclei

The last special case of collective motion in this section is the rotational-vibrational model. Nuclei with an axially deformed minimum present small oscillations in both the γ and β degrees of freedom. Therefore, in general, it is possible to describe the Hamiltonian as:

$$H = H_{vib} + H_{rot}. \tag{2.9}$$

The explicit expression of the Hamiltonian is a function which depends on the deformation parameters, β and γ, the total angular momentum, I, and its projection on the symmetry axis, K. The representation, in terms of the shape and angle variables, provides a simple description of the situation in which the nucleus oscillates around a nonspherical equilibrium shape. In this case, the motion of the nucleus is composed of rotations and intrinsic shape vibrations:

$$E_{n_\beta n_\gamma IK} = \hbar\omega_\beta(n_\beta + \frac{1}{2}) + \hbar\omega_\gamma(2n_\gamma + \frac{1}{2} \mid K \mid +1) + \frac{\hbar^2}{2\mathscr{I}}[I(I+1) - K^2], \quad (2.10)$$

where n_β and n_γ are the number of quanta of vibration added in the β and γ directions respectively. Due to the ambiguity in the choice of intrinsic axes, the symmetrization of the wave function leads to the condition that only even values of K are possible. Given that the wave function only depends on $\mid K \mid$, it is enough to consider positive values of K. Fig. 2.4 shows the band structure of the spectra generated by eq. 2.10 for an even-even nucleus. The bands are defined by a set of quantum numbers (K, n_β, n_γ). The ground state band correspond to (0,0,0); the β-band to (010) (contains one quantum in β direction) and, the γ-band is characterized by K=2.

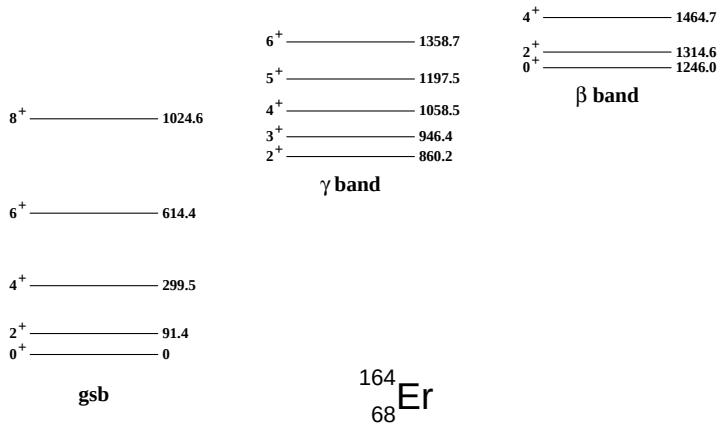

Figure 2.4: Ground, γ and β bands of a standard deformed nucleus, ^{164}Er [31].

2.2 The deformation region A∼100

In the study of nuclear structure some of the most interesting regions are those of structural change, where the spherical shapes evolve into deformed configurations. One of those regions has mass number A∼100, where the nuclear shape is predicted to change quite dramatically [22].

From an empirical point of view the main observables are the ratio between the energy of the first excited 4^+ state and the energy of the first exited 2^+ state, $R_{4/2}$=E(4_1^+)/E(2_1^+); the energy of the first excited 2^+ state and, the reduced transition probability, B(E2:$2_1^+ \rightarrow 0_1^+$), where the subscript 1 refers to the lowest energy state with a given spin and parity.

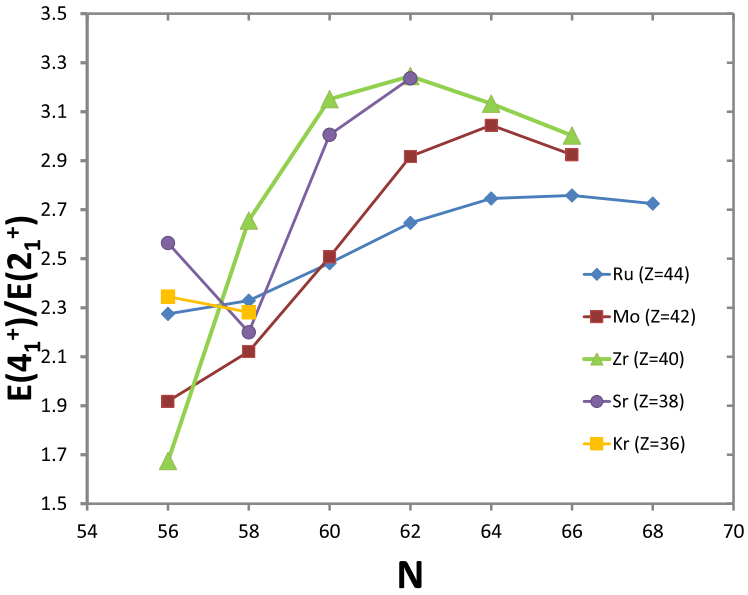

Figure 2.5: The energy ratio $R_{4/2}$ as a function of N, for even-A Ru, Mo, Zr, Sr and Kr nuclei.

From the energy spectra in the previous section it is easy to follow that the value of the energy ratio $R_{4/2}$ can vary from 2 for a spherical vibrator to 3.33 for a prolate symmetric rotor, so is a key indicator of nuclear deformation. Fig. 2.5 shows the evolution of the E(4_1^+)/E(2_1^+) values in the A$\sim$100 region as a function of the neutron number for Ru, Mo, Zr, Sr and Kr nuclei. As is illustrated in the figure, the ratio changes from a minimum value around N = 58 to a maximum, of approximately 3.3, for N = 62, 64; indicating the existence of well deformed symmetric rotors in the cases of zirconium and strontium.

Fig. 2.6 shows that the energy of the first exited 2_1^+ state decreases as collectivity (deformation) increases. The main changes in E(2_1^+) occur in Sr and Zr in which the excitation energy decreases, indicating a transition between a spherical shape

and a deformed rotor. The fast change in the deformation of the zirconium isotopes is what makes it more interesting when compared with the other nuclei in the region.

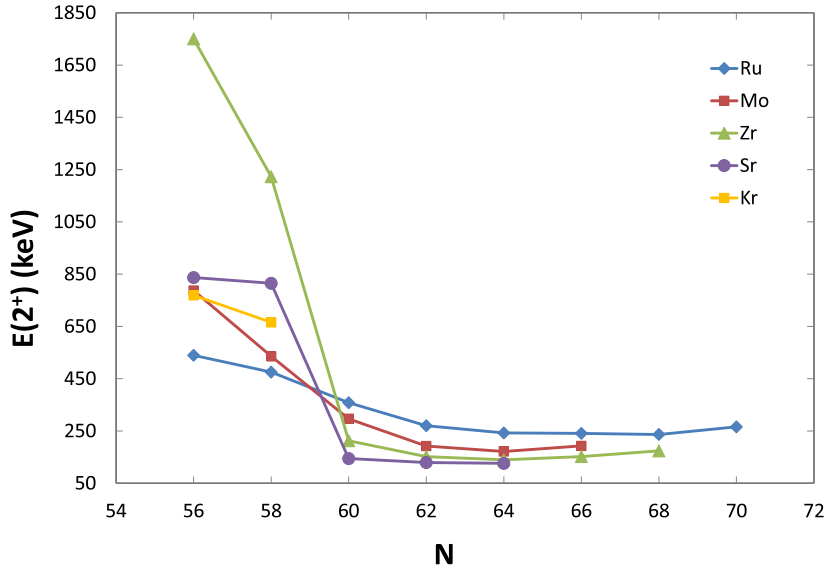

Figure 2.6: The energy of the first excited 2^+ state, as a function of N, for even-A Ru, Mo, Zr, Sr and Kr nuclei.

The energy of the first excited 2^+ state can be used to calculate a β_2 deformation by using Grodzin's formula [32]:

$$E(2_1^+) = \frac{1225}{A^{7/3}\beta_2^2} \tag{2.11}$$

where the $E(2_1^+)$ energy is in MeV and the subscript 2 correspond to the quadrupole term ($\lambda = 2$ in the previous section). The results of this calculation in the region of interest are presented in Fig. 2.7 which shows a maximum for the N = 62, 64 nuclei.

$B(E2{:}2_1^+ \rightarrow 0_1^+)$ is a key observable since it is directly related to the quadrupole moment and hence the degree of deformation. The deformation parameter, β_2, can be calculated from the half-lives of the first 2_1^+ state via the transition probability, λ, defined as:

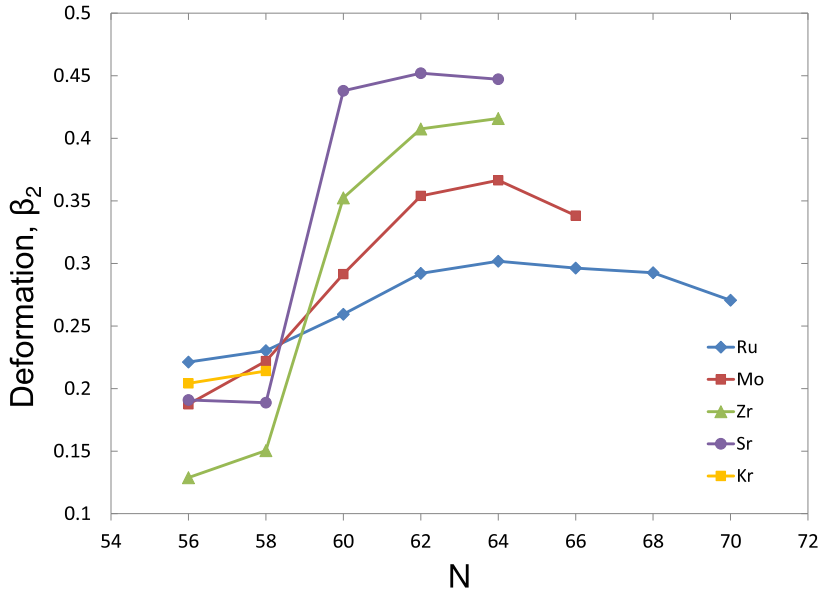

Figure 2.7: The deformation parameter β_2, calculated using Grodzin's formula, as a function of N, for even-A Ru, Mo, Zr, Sr and Kr nuclei.

$$\lambda = \frac{ln2}{T_{1/2}}. \tag{2.12}$$

The transition probability, λ, is also related to the reduced transition probability for an electric multipole transition B(EL:initial state→final state). In the present case, the transition studied is an electric quadrupole transition from the first excited 2^+ state to the first 0^+state, B(E2:$2_1^+ \rightarrow 0_1^+$), which is related to its transition probability in the following way [33]:

$$\lambda(E2) = 1.22 \cdot 10^9 E_\gamma^5 B(E2) \tag{2.13}$$

where E_γ is measured in MeV, λ in s^{-1} and the B(E2) value is in e^2fm^4. For an axially symmetric nucleus ($\gamma = 0^o$) the B(E2) value is also related to the intrinsic quadrupole moment Q_0 [34] by:

$$B(E2 : 2_1^+ \rightarrow 0_1^+) = \frac{e^2 Q_0^2}{16\pi}. \tag{2.14}$$

Finally, the quadrupole moment is related to the deformation parameter through the formula [34]:

$$Q_0 = \frac{3}{\sqrt{5\pi}} Z R_0 \beta_2 (1 + 0.16\beta_2) \tag{2.15}$$

to second order in β_2. It is assumed that R_0 is the radius of the spherical nucleus given by the equation: $R_0 = 1.2A^{1/3}$, in fm. Fig. 2.8 shows the results calculated for Ru, Mo, Zr and Sr nuclei using this formula. In the cases of Zr and Sr a large increase in the value of the deformation parameter occurs between N=58 and N=60.

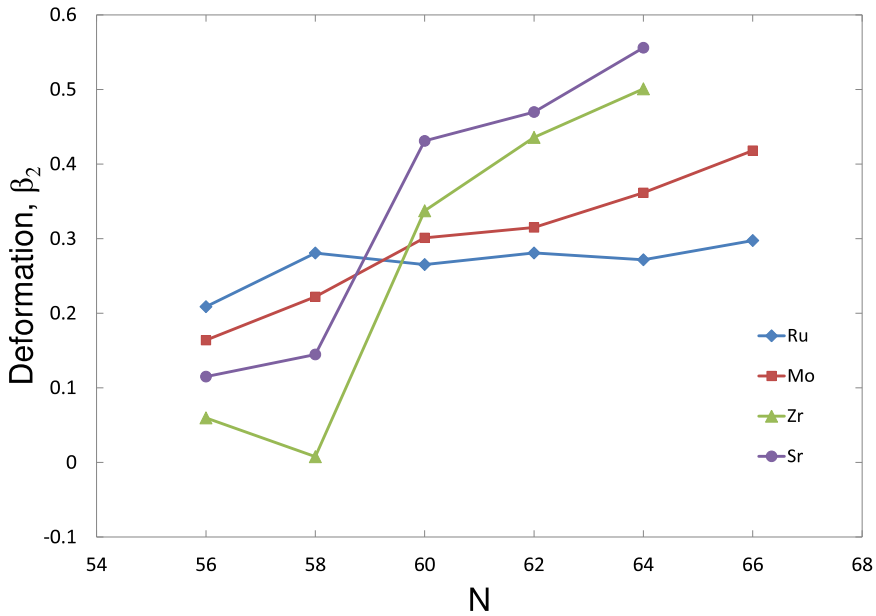

Figure 2.8: The deformation parameter β_2, calculated from the half-lives [35, 36, 37, 38, 39, 40, 41], as a function of N.

A more direct measurement of the shape is via the change in the nuclear mean-square radius $\delta < r_2 >^{A,A'}$, which can be expressed as a function of β_2 by [42]:

$$\delta < r^2 >^{A,A'} = \delta < r^2 >_{sph} + < r^2 >_{sph} \frac{5}{4\pi} \sum_i \delta < \beta_i > \qquad (2.16)$$

where $< r^2 >_{sph}$ is the mean-square radius of a spherical nuclei of the same volume, $\delta < r^2 >_{sph}$ is the change in the mean-square radius respect to the spherical shaped nucleus, and i denotes the multipole order. From isotope shift measurements it is possible to obtain information about $\delta < r^2 >^{A,A'}$ in the region of interest. Fig. 2.9 shows the difference in the mean square charge radii relative to N=50 for krypton [43], rubidium [44], strontium [45, 46], yttrium[42], zirconium[47] and molybdenum[11]. The figure clearly shows a large increase in $\delta < r^2 >^{N,50}$ around N=60, especially for Zr, Y, Sr and Rb. This has been interpreted as the onset of deformation [42].

The experimental data presented in figs. 2.5, 2.6, 2.7, 2.8 and 2.9 shows a sudden shape change around N=60, especially in the cases of Sr and Zr which jump from spherical to well-deformed prolate configurations. Figs. 2.5, 2.6, 2.7, 2.8 and 2.9 also show that the zirconium nuclei are the isotopes with the greater degree of deformation (fig. 2.5 shows the $R_{4/2}$ value close to the value for a perfect rotor for ^{102,104,106}Zr). Moreover fig. 2.8 shows that half-life measurements of the first 2^+ states indicate that the quadrupole deformation increases toward N=64. However the evolution of the structure of the ground state beyond ^{108}Zr remains unknown, as does the structural information about non-yrast states beyond ^{102}Zr. Currently, the only information available comes from several theoretical calculations, which are still unproven. J. Skalski et al., using global shape calculations with the Nilsson-Strutinsky method and the cranked Woods-Saxon average potential [22], concluded that nuclei with oblate and prolate ground states are expected to coexist in this region of the nuclear chart. In the case of Zr nuclei (Z=40) with 60<N<72, Skalski's calculations indicate well-deformed prolate ground-states, with oblate structures at excitation energies around 1 MeV. Also, specifically for ^{106}Zr, Salski predicted a prolate ground state with a deformation $\beta_2 = 0.37$ and

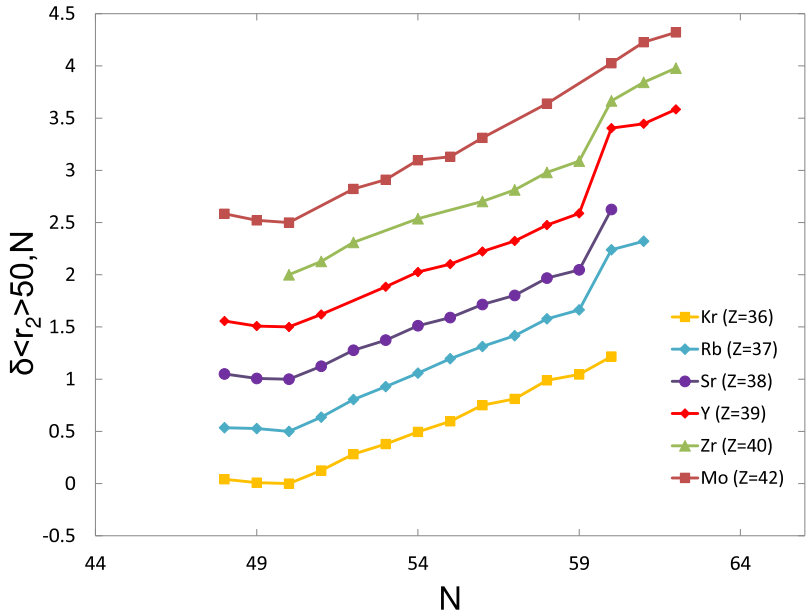

Figure 2.9: The difference in the mean square charge radii relative to N=50 for krypton [43], rubidium [44], strontium [45, 46], yttrium[42], zirconium[47] and molybdenum[11] as a function of the neutron number, N. Each isotope chain is separated by 0.5 fm^2 in the figure, with the intention of making it clearer.

the oblate minimum at an excitation energy of 1.4 MeV. On the other hand, Chasman et al. [48], using the liquid drop model and the shell-correction approach with the Woods-Saxon potential, predict that the transition to oblate shape will occur at the mid shell isotone ^{106}Zr. Further calculations by Xu et al. [49], based on a non axial deformed WS potential in the framework of the cranked shell model using the total Routhian surface show coexisting prolate ($\beta_2 \sim 0.35$) and oblate ($\beta_2 \sim 0.2$) minima for zirconium isotopes with $66 \leq N \leq 76$. Xu also concluded that the oblate shape is stabilised at high spin, by the addition of angular momentum due to the alignment of pairs of $g_{9/2}$ protons and $h_{11/2}$ neutrons.

Therefore the experimental and theoretical information to date suggests a picture of shape coexistence in the zirconium isotopes and, at the same time, highlights the need for new experimental information in order to understand the structural evolution of these nuclei. As suggested in the introduction, the Interacting Boson Model is a theoretical approach, which has been applied with success to study the

low spin states of the nuclei in transitional regions [8, 9, 10]. The interpretation of the zirconium isotopes within this model, will be the subject of the next chapter.

Chapter 3

The Zr isotopes within the IBM context

The interacting boson model (IBM) [6] is a theory used to study medium and heavy nuclei in a relatively easy way. Based on the shell model but reducing its complexity by combining the nucleons in pairs (bosons), it has many similar properties to the collective models (described in section 2.1). This model is able to determine quantitatively several properties of the atomic nucleus such as the nuclear moment, the energy levels of the nucleus and their transition probabilities. It has been widely used in the past in order to study exotic nuclei [7, 10, 50, 51].

Within the IBM-1 theoretical framework [52], a series of calculations have been performed to provide a prediction and explanation of the low spin states of ^{102,104,106,108}Zr. The IBM-1 programs used previously in [51] [7] and the last available experimental data, have been combined to study the structural evolution of zirconium nuclei in the region A$\sim$100.

This chapter is structured as follows: Section 3.1 provides a brief introduction to the IBM-1. In the following sections, the methodology used to perform the IBM calculations for the case of ^{102,104,106}Zr and its results are explained. As the same procedure is used in the three zirconium isotopes, it is only discussed in detail in the case of ^{102}Zr, while for ^{104,106}Zr only the results are presented. Finally, some

general conclusions are highlighted and new data on ^{108}Zr is discussed.

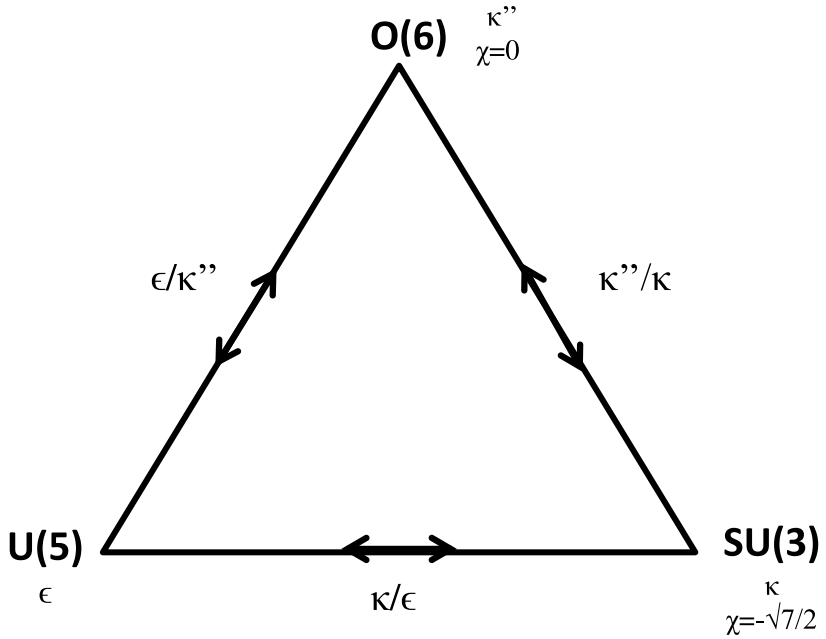

Figure 3.1: Casten triangle.The parameters of the Casten triangle are based on a simplified three-dimensional IBM Hamiltonian:$H = \epsilon \hat{n_d} + \kappa \hat{Q^\chi} \cdot \hat{Q^\chi} + \kappa'' \hat{P^\dagger} \cdot \hat{P}$. Each vertex represents one of the three symmetry limits of the IBM. The value of the coefficients giving each dynamical symmetry are indicated, as well as the ratio between the coefficients which give the change between two limits (along the sides of the triangle).

3.1 Interacting Boson Model

The Interacting Boson Model (IBM) or Interacting Boson Approximation (IBA) [53] describes the collective excitations of even-even nuclei as a result of interaction between bosons. In its simplest version, IBM-1, fermions (no distinction is made between protons and neutrons) are coupled in pairs of angular momenta 0 and 2, known as s and d bosons. Therefore, low-lying collective states of the nuclei can be described as a result of the interaction between these two types of bosons. In the IBM, closed shells of either protons or neutrons are neglected, thus the excitation spectra of the nuclei depends only on the valence space. It is

possible to define the creation and annihilation operators of the s and d bosons as follows [52]:

$$\begin{aligned} s|n_s>&=\sqrt{n_s}|n_s-1>, \qquad s^\dagger|n_s>=\sqrt{n_s+1}|n_s+1> \\ d_\mu|n_{d_\mu}>&=\sqrt{n_{d_\mu}}|n_{d_\mu}-1>, \quad d_\mu^\dagger|n_{d_\mu}>=\sqrt{n_{d_\mu}+1}|n_{d_\mu}+1> \end{aligned} \tag{3.1}$$

where n_d and n_s are the number of d and s bosons respectively and μ=2,1,...,-2. The 36 bilinear products of the boson creation and annihilation operators satisfy the commutation relations of the unity Lie algebra in six dimensions, U(6). In addition, it is possible to express the Hamiltonian of a physical system described by the bosons as a combination of these 36 operators. Such a Hamiltonian, in the multipole expansion, it is often written in two forms:

$$H=\epsilon\hat{n_d}+\kappa\hat{Q^\chi}\cdot\hat{Q^\chi}+\kappa'\hat{L}\cdot\hat{L}+\kappa''\hat{P^\dagger}\cdot\hat{P}+c_3\hat{T_3}\cdot\hat{T_3}+c_4\hat{T_4}\cdot\hat{T_4}, \tag{3.2}$$

or

$$H=\epsilon\hat{n_d}+\kappa\hat{Q^\chi}\cdot\hat{Q^\chi}+\kappa'\hat{L}\cdot\hat{L}+\kappa''\hat{P^\dagger}\cdot\hat{P}+c_3\hat{T_3}\cdot\hat{T_3}+\lambda\hat{n_d}^2, \tag{3.3}$$

where $\epsilon,\kappa,\kappa',\kappa'',\lambda,c_3$ and c_4 are free parameters, $\hat{n_d}=d^\dagger\cdot d$ is the number of d-bosons and the last term, $\hat{n_d}^2$, leads to a so-called τ-compression which varies the moment of inertia proportionally to the angular momentum [54]. $L_\mu\equiv\sqrt{10}\hat{[d^\dagger\times d]}^{(1)}_\mu$ is the angular momentum operator and, the operators $\hat{T_3}$ and $\hat{T_4}$ are defined as follows $\hat{T^{}_{3,\mu}}\equiv[d^\dagger\times d]^{(3)}_\mu$ and $\hat{T^{}_{4,\mu}}\equiv[d^\dagger\times d]^{(4)}_\mu$. Finally, the quadrupole operator is $\hat{Q^\chi}\equiv[d^\dagger\times s+s^\dagger\times d]^{(2)}_\mu+\chi[d^\dagger\times d]^{(2)}_\mu$ and, in the Consistent-Q Formalism [55], the operator for electric quadrupole transitions is $\hat{T_\mu}=e_b\hat{Q^\chi_\mu}$.

The 36 IBM operators which constitute the Hamiltonian conform the Lie algebra $U(6)$. The decomposition of $U(6)$ into different subalgebras leads to separate symmetries, three of which are interesting from a physical point of view, $U(5)$, $SU(3)$ and $O(6)$. The $U(5)$ symmetry represents an anharmonic vibrator, the $SU(3)$ a symmetric rotor and the $O(6)$ an gamma-soft rotor. The three symmetries generate different spectra, examples of which can be found in [53]. The Hamiltonians, corresponding to each of these three limits, in multipole expansion are:

$$\begin{array}{ccc} U(5) & \rightarrow & H = \epsilon \hat{n_d} + \kappa' \hat{L} \cdot \hat{L} + c_3 \hat{T_3} \cdot \hat{T_3} + c_4 \hat{T_4} \cdot \hat{T_4}, \\ SU(3) & \rightarrow & H = \kappa \hat{Q^\chi} \cdot \hat{Q^\chi} + \kappa' \hat{L} \cdot \hat{L}, \\ O(6) & \rightarrow & H = \kappa' \hat{L} \cdot \hat{L} + \kappa'' \hat{P^\dagger} \cdot \hat{P} + c_3 \hat{T_3} \cdot \hat{T_3}. \end{array} \tag{3.4}$$

In reality, most nuclei do not satisfy the particular constraints of one of these symmetries, so that to perform realistic calculations a deviation from these limits, or a transition between them, will be required. The three limits are illustrated in fig. 3.1 and can be used as reference points to develop a more realistic description of the low lying collective states of a single nucleus or series of nuclei [53]. The figure shows a symmetry triangle. Based on a simplified 3D-Hamiltonian, each vertex represents one of the analytic limits of the IBM, the three sides represent a transition path between two limits while the inner space of the triangle represents the body of more general solutions that can be obtained from the general Hamiltonian 3.2/3.3. The structure of a particular transition along the sides will be determined, at any point, by the ratio between the two parameters which characterize the symmetries in question.

From this discussion it is clear that the IBM provides an easy way to study transition regions (besides the three basic symmetries) as a function of a small set of parameters, constituting a significant simplification compared to other nuclear models.

Before discussing the calculations presented in this chapter, it is convenient to make a brief introduction to the programs employed. During this study, three programs have been used: fiti, ibm and ibmt. The first code, fiti, fits of the parameters in the IBM1 Hamiltonian, which can be written in the two forms discussed in section 3.1, in order to reproduce experimental energy levels and, calculates E2 reduced transition probabilities; ibm calculates the energy levels for a given set of parameters; and ibmt, uses the output provided by the ibm code to calculate the reduced transition probabilities. The calculations performed for the isotopes ^{102,104,106}Zr were performed with the fiti code and reproduced with ibm and ibm1t. In the case of ^{108}Zr, the three programs were used to provide original results based on two different approaches.

3.2 Results for ^{102}Zr and methodology:

For a given nucleus, the total number of bosons, N, is defined as half the number of valence particles or holes counted from the nearest proton and neutron closed shell [34]. This means that the number of bosons is fixed for a given nucleus and limits the maximum spin that can be calculated with this theory. This also means that two nuclei with different numbers of neutrons and protons but the same total number of bosons could be predicted to have exactly the same behaviour (if they had the same values of the parameters in the Hamiltonian). In order to avoid this problem, the relevant parameters have been adjusted following the convention adopted in [51]. Namely, a procedure which separately considers chains of isotones (N= 62) and isobars (A=102), and provides a different set of parameters in each case. Tables 3.1 and 3.3 show respectively the experimental energies and transition probabilities used for each nucleus in the isobaric (^{102}Pd (N=5),^{102}Ru (N=7),^{102}Mo (N=9),^{102}Zr (N=11)) and isotonic chains (^{106}Ru (N=9),^{104}Mo (N=10),^{102}Zr (N=11)), to fit the low spin states in ^{102}Zr.

In addition to the six parameters in each Hamiltonian in eq. 3.2 and 3.3, χ and e_b also have to be determined. Ergo there are eight possible parameters to minimize. Although these parameters might vary with the boson number, in order to keep

Nucleus	J^π	E_1	E_2	E_3	Nucleus	J^π	E_1	E_2	E_3
^{102}Pd	0^+	0	1593	1658					
(N=5)	2^+	556	1534	1994					
	3^+	2112							
	4^+	1276	2138						
	5^+								
	6^+	2111							
	7^+								
	8^+	3340							
	9^+								
	10^+	3340							
^{102}Ru	0^+	0	944	1968	^{106}Ru	0^+	0	991	
(N=7)	2^+	475	1103	1581	(N= 9)	2^+	270	792	
	3^+	1522				3^+	1092		
	4^+	1106	1799			4^+	715	1307	
	5^+					5^+	1641		
	6^+	1873				6^+	1296	1908	
	7^+					7^+	2284		
	8^+	2706				8^+	1973		
	9^+					9^+			
	10^+	3434				10^+	2705		
^{102}Mo	0^+	0	698	1334	^{104}Mo	0^+	0	886	
(N=9)	2^+	297	848	1250	(N= 10)	2^+	192	812	
	3^+	1245				3^+	1028		
	4^+	744	1398			4^+	561	1215	
	5^+					5^+	1476		
	6^+	1327				6^+	1080	1724	
	7^+					7^+	2037		
	8^+	2019				8^+	1722		
	9^+					9^+			
	10^+	2418				10^+	2455		
^{102}Zr	0^+	0	895		^{102}Zr	0^+	0	895	
(N=11)	2^+	152	1036	1211	(N=11)	2^+	152	1036	1211
	3^+					3^+			
	4^+	478	1387	1538		4^+	478	1387	1538
	5^+					5^+			
	6^+	965	1652	1829		6^+	965	1652	1829
	7^+					7^+			
	8^+	1595				8^+	1595		
	9^+					9^+			
	10^+	2351				10^+	2351		

Table 3.1: Experimental energies (in keV) for levels in neutron-rich A=102 isobaric and N=62 isotonic chains [38, 39, 40] used in the characterization of the parameters for ^{102}Zr.

the number of free parameters to a minimum they are taken as constant for a given chain [51]. Therefore the structural changes within a chain depends only on the boson number N.

The first task is to establish the value of χ. Using the Hamiltonian proposed in [51] (given by eq. 3.2 with κ' and κ'' equal to zero) and the experimental data shown in tables 3.3 and 3.1, for the isobaric chain, it is possible to calculate the root mean square (rms), of the difference between the calculated and experimental energies and B(E2) values, in the following way [7]:

$$\Delta(E) = \sqrt{\frac{1}{N_E}\sum_i (E^i_{ex} - E^i_{th})^2}, \tag{3.5}$$

$$\Delta(E2) = \sqrt{\frac{1}{N_{E2}}\sum_i (B(E2)^i_{ex} - B(E2)^i_{th})^2}, \tag{3.6}$$

where N_E and N_{E2} are the number of energy levels and B(E2) values used in the fit respectively. The value of $\chi = -0.6$ was found to be the one which gave smaller values of both standards deviations. This calculation was repeated with different Hamiltonians and it was found that the value of χ which minimizes both standard deviations almost does not vary on changing the Hamiltonian. Therefore a value of $\chi = -0.6$ was used for all the calculations, and the next step is determine the appropriate Hamiltonian.

As a starting point, the Hamiltonian corresponding to each of the three limits of the IBM was tried. For each one, the initial values of the parameters ($\epsilon, \kappa, \kappa', \kappa$", c_3, c_4 or λ) were varied in order to find a global minimum. As the results displayed in table 3.2 show, all the three cases give a big rms deviation in terms of energy, so it is possible to conclude that we are looking for a transitional Hamiltonian.

Symmetries	Hamiltonian	$\Delta(E)_A(keV)$	$\Delta(E2)_A(me^2b^2)$
SU(3)	$H = \kappa\hat{Q}^\chi \cdot \hat{Q}^\chi + \kappa'\hat{L} \cdot \hat{L}$	471	108
O(6)	$H = \kappa'\hat{L} \cdot \hat{L} + \kappa''\hat{P}^\dagger \cdot \hat{P} + c_3\hat{T}_3 \cdot \hat{T}_3$	483	84
U(5)	$H = \epsilon\hat{n_d} + \kappa'\hat{L} \cdot \hat{L} + c_3\hat{T}_3 \cdot \hat{T}_3 + c_4\hat{T}_4 \cdot \hat{T}_4$	312	121

Table 3.2: The table shows the rms deviation for the experimental energies and reduced transition probabilities for the ^{102}Zr isobaric chain in the case of the three IBM-1 limits.

It was found that two or three-term Hamiltonians gave a poor result while more than four term Hamiltonians lead to unstable solutions. Therefore, a four-term Hamiltonian was decided to be the best option. In the multipolar expansion, there are two possible Hamiltonians with six terms each, as defined in equations 3.2 and 3.3. Given that five of the six terms are common, combinatorics give twenty five possible four-term Hamiltonians, which are shown in table 3.4. The table shows the minimum energy and transition probability standard deviations obtained for each of the Hamiltonians listed, by varying the parameters in each Hamiltonian. All twenty five possibilities were tried for the isobaric chain, while only the Hamiltonians which provided smaller values of energy rms deviation were used for the isotonic chain.

Transition	^{102}Pd	^{102}Ru	^{102}Mo	^{102}Zr	^{104}Mo	^{106}Ru
$2_1^+ \to 0_1^+$	0.0926(64)	0.1276(20)	0.1979(63)	0.3924(871)	0.2233(184)	0.1976(296)
$4_1^+ \to 2_1^+$	0.1445(70)	0.1889(315)	0.2543(508)	_	0.3208(98)	_
$0_2^+ \to 2_1^+$	_	0.1005(160)	0.1935(760)	_	0.3184(100)	_
$2_2^+ \to 2_1^+$	_	0.1454(181)	_	_	_	_

Table 3.3: Experimental B(E2) values (in units e^2b^2) used in the calculation of e_b [38, 39, 40].

	$\hat{n_d}$	$\hat{P}^\dagger\hat{P}$	$\hat{Q}^\chi\hat{Q}^\chi$	$\hat{L}\hat{L}$	$\hat{T}_3\hat{T}_3$	$\hat{T}_4\hat{T}_4$	${\hat{n_d}}^2$	$\Delta(E)_A$ (keV)	$\Delta(E2)_A$ (me^2b^2)	$\Delta(E)_N$ (keV)	$\Delta(E2)_N$ (me^2b^2)
1	X	X	X			X		165	74	161	75
2	X	X	X	X				160	77	95	64
3	X	X	X		X			155	53	98	99
4	X	X		X	X			231	91		
5	X	X		X		X		192	58		
6	X	X			X	X		192	68		
7	X		X	X	X			167	56	98	99
8	X		X	X		X		166	83	128	147
9	X		X		X	X		146	63	97	138
10	X			X	X	X		312	140		
11		X	X	X		X		325	99		
12		X	X	X	X			454	175		
13		X		X	X	X		336	103		
14			X	X	X	X		327	87		
15		X	X		X	X		414	131		
16	X	X	X				X	214	72		
17	X	X		X			X	231	88		
18	X	X			X		X	237	94		
19	X		X	X			X	123	82	115	140
20	X		X		X		X	170	55		
21	X			X	X		X	312	135		
22		X	X	X			X	462	198		
23		X		X	X		X	441	95		
24			X	X	X		X	442	195		
25		X	X		X		X	495	84		

Table 3.4: The minimised root mean square values obtained by varying the parameters in each Hamiltonian. The first column assigns a number to each Hamiltonian; columns two to the eight indicate which terms of the general Hamiltonian are considered in a particular calculation; finally, the last four columns show the root mean square for the energy levels and B(E2) values (using $e_b = 0.11$ eb), the first two for the ^{102}Zr isobaric chain and the last two for the ^{102}Zr isotonic chain.

	Isotones (N=62)						
	$\hat{n_d}$	$\hat{P}^\dagger\hat{P}$	$\hat{Q}^\chi\hat{Q}^\chi$	$\hat{L}\hat{L}$	$\hat{T}_3\hat{T}_3$	$\hat{T}_4\hat{T}_4$	$\hat{n_d}^2$
2	0.8867	0.2803	0.0312	0.0143			
3	1.0837	0.0735	-0.0291		-0.1443		
7	0.8710		-0.0336	0.0035	-0.1330		
9	1.1195		-0.0353		-0.1178	-0.1060	
19	0.6739		-0.0277	0.0167			-0.0752

	Isobars (A=102)						
	$\hat{n_d}$	$\hat{P}^\dagger\hat{P}$	$\hat{Q}^\chi\hat{Q}^\chi$	$\hat{L}\hat{L}$	$\hat{T}_3\hat{T}_3$	$\hat{T}_4\hat{T}_4$	$\hat{n_d}^2$
2	0.9032	0.2629	0.0401	0.0146			
3	0.9318	-0.0657	-0.0420		-0.1664		
7	0.9140		-0.0296	0.0012	-0.1296		
9	1.055		-0.0304		-0.1098	-0.0734	
19	0.8534		-0.0283	0.0108			-0.0791

Table 3.5: The value of the coefficients for the Hamiltonians 2, 3, 7, 9 and 19 in the ^{102}Zr calculation. The first column assigns a number to each Hamiltonian; columns two to eight indicate the different terms of the general Hamiltonian considered in a particular calculation.

At this point, Hamiltonians 2,3,7,9 and 19 were used to calculate the reduced effective charge, e_b, using all the reduced transition probabilities available in a given chain. These are shown in table 3.3. For a given Hamiltonian, the matrix elements are provided by the fit. As the B(E2) value is given by:

$$B(E2; I \to I') = e_b^2 \frac{| < I'||Q^\chi||I > |^2}{(2I+1)} \tag{3.7}$$

the value of e_b is calculated to minimize the difference between the theoretical and experimental reduced transition probabilities. The value was calculated by making an average of the quantities obtained for each chain using the five Hamiltonians mentioned earlier. The result was $e_b = 0.11$.

The different results for the rms deviation in energy and reduced transition probability give an idea of the precision of this procedure. Inspection of the calculated

rms deviations indicates that the Hamiltonians labelled as 2, 3, 7, 9, 19 give better fits, although there is not enough difference to chose a particular one over the others. The value of the calculated coefficients for each of these Hamiltonian are shown in table 3.5. The presence of the $\hat{n_d}$ and $\hat{Q^\chi}\hat{Q^\chi}$ terms in these Hamiltonians suggest a region of transition between U(5) and SU(3) symmetries, while the small value of χ and the existence of a $\hat{P}^\dagger\hat{P}$ term in two of the five Hamiltonians indicates a certain degree of O(6) symmetry is also present.

	Isobars (A=102)					
Transition	Experimental	H_2	H_3	H_7	H_9	H_{19}
$2_1^+ \to 0_1^+$	0.3924(871)	0.2347	0.3464	0.3320	0.4119	0.4585
$4_1^+ \to 2_1^+$		0.3385	0.5144	0.5022	0.5940	0.6431
$2_2^+ \to 0_2^+$		0.0703	0.1318	0.0517	0.0312	0.0794
$2_3^+ \to 0_2^+$		0.1021	0.0962	0.2020	0.2501	0.2389
	Isotones (N=62)					
Transition	Experimental	H_2	H_3	H_7	H_9	H_{19}
$2_1^+ \to 0_1^+$	0.3924(871)	0.2536	0.3727	0.3777	0.4529	0.4387
$4_1^+ \to 2_1^+$		0.3567	0.5389	0.5432	0.6354	0.6108
$2_2^+ \to 0_2^+$		0.1914	0.1653		0.0441	0.0382
$0_2^+ \to 2_2^+$				0.0263		
$2_3^+ \to 0_3^+$		0.1905	0.2441	0.2357	0.2203	0.3072

Table 3.6: Experimental and theoretical B(E2) values (in units of e^2b^2) for transitions in ^{102}Zr. The upper half of the table shows the results calculated by fitting the parameters of the Hamiltonians using the experimental data available in the isobaric chain, while the bottom half shows the values obtained using the known data in the isotonic chain. A value of $e_b = 0.11$ is used in all the cases.

Figures 3.2 and 3.3 show the calculated energy levels of ^{102}Zr using the Hamiltonians 2, 3, 7, 9 and 19 alongside the experimental data. The calculated values for the yrast states are close to the experimental data in all cases, while the results become less precise as we move higher in energy, beyond the second spin

0^+ state. All calculated transition probabilities are shown in tables 1 and 2 in appendix A. Figures 3.2 and 3.3 also show the stronger transition probabilities, namely the transitions which values are bigger than 0.09 e^2b^2. The levels in the figures are grouped in bands according to the calculated transition probabilities. The calculated set of levels are 0_1^+, 2_1^+, 4_1^+, 6_1^+, 0_2^+, 2_2^+, 4_2^+, 6_2^+, 0_3^+, 2_3^+, 4_3^+ and 6_3^+. Although the initial intention was to represent all the levels, the 0_3^+ level was removed in most of the cases plotted in the figures due to small transition probabilities connecting this level with the others. Given that figures 3.2 and 3.3 show that the β-band is lower in energy than the γ-band for the particular case of ^{102}Zr and that is a common feature of the nuclei populating this region, we can conclude looking at the figures that the results obtained using Hamiltonian 7 are the only ones which verify this fact using both chains.

Table 3.6 shows the results for some reduced transition probabilities. For both isobaric and isotonic chains, Hamiltonian 2 gives weaker B(E2) values while 9 and 19 predict stronger transitions. Four of the five Hamiltonians (3, 7, 9 and 19) provide a prediction which agrees within the error with the only transition probability measured so far. The difference between the results of the calculations obtained using different Hamiltonians and either the isobaric or isotonic chain gives an idea of the limitations of the method.

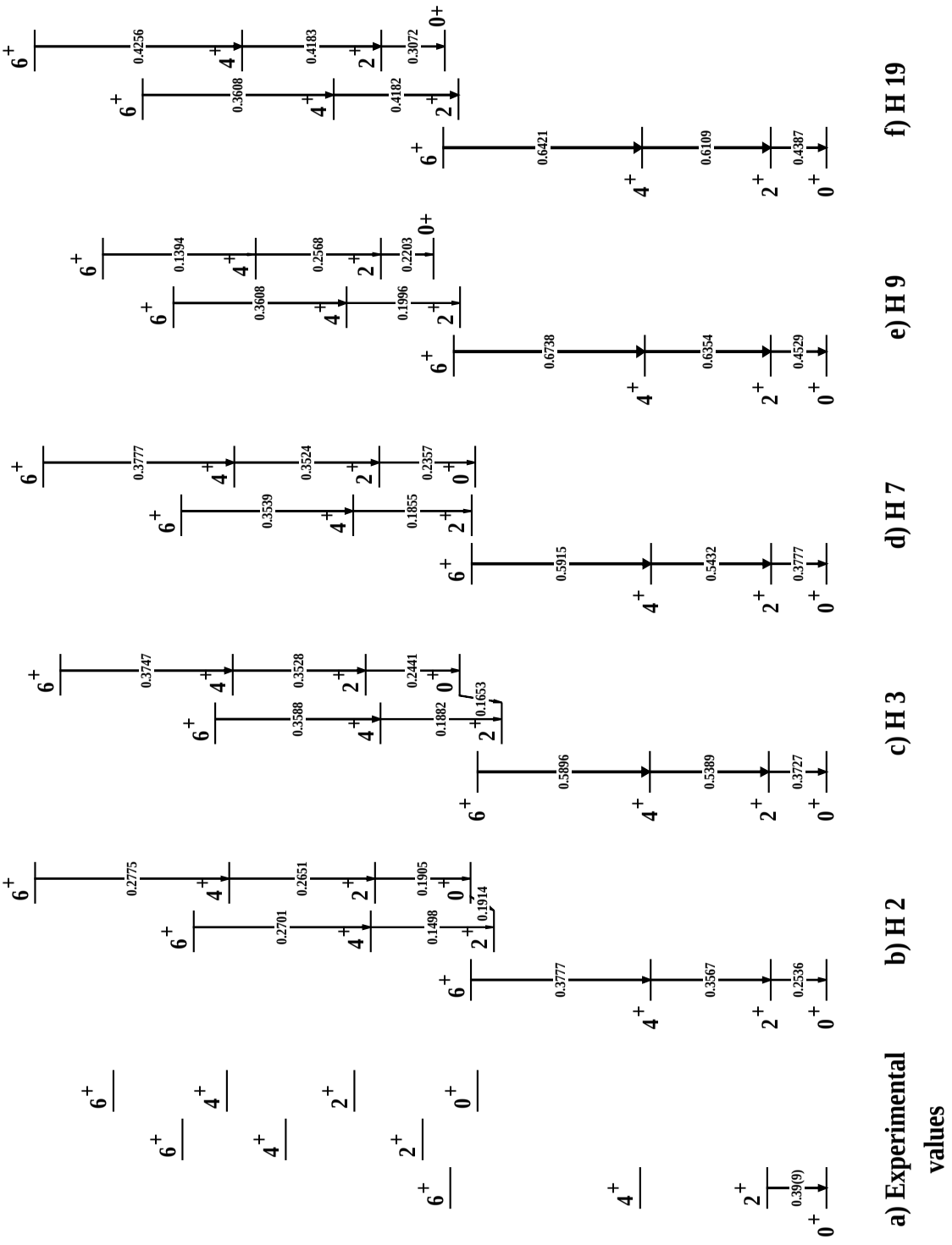

Figure 3.2: Experimental and theoretical energy levels of ^{102}Zr. The parameters in each Hamiltonian are obtained by minimizing the rms deviation with respect to the energy levels of the isotonic chain. The levels are grouped in bands according to the calculated transition probabilities, which are given in units of e^2b^2.

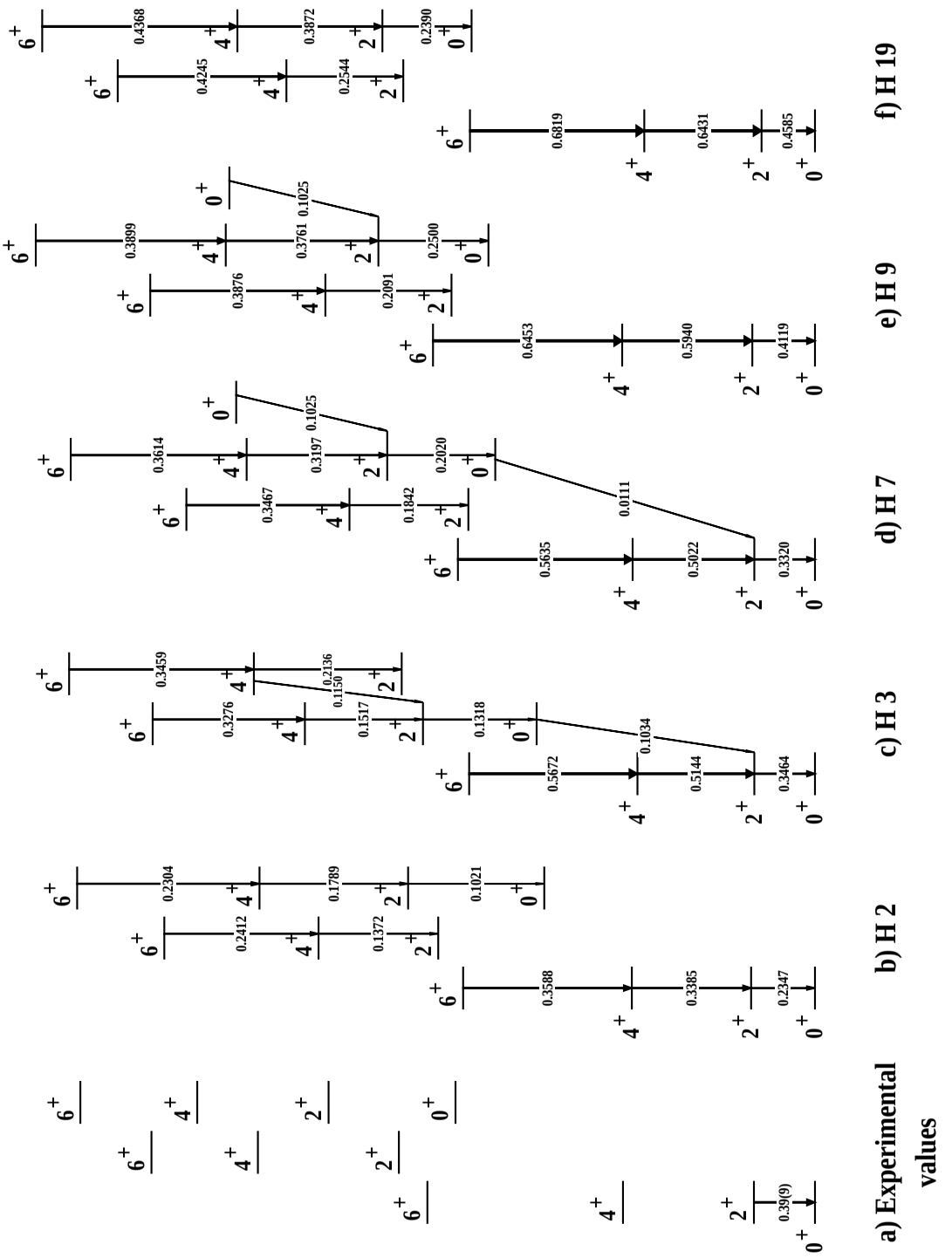

Figure 3.3: Experimental and theoretical energy levels of ^{102}Zr. The parameters in each Hamiltonian are obtained by minimizing the rms deviation with respect to the energy levels of the isobaric chain. The levels are grouped in bands according to the calculated transition probabilities, which are given in units of e^2b^2.

3.3 Results for ^{104}Zr:

In order to make a calculation of the energy levels and transition probabilities in ^{104}Zr, data in two separate chains of nuclei have been used. The nuclei of the isotonic chain (N=64) are: ^{110}Pd, ^{108}Ru, ^{106} Mo and ^{104}Zr; while the isobaric chain (A=104) is composed of ^{104}Ru, ^{104}Mo and ^{104}Zr. The experimental energy levels and B(E2) values used to fit the parameters in the Hamiltonian are shown in tables 3 and 4, in appendix A, respectively. Following the procedure explained in the previous section, the values obtained for e_b and χ were 0.1 and -0.3. The value of the effective boson charge is similar to the one in the case of ^{102}Zr, but the value of χ is significantly lower. Twenty-five four-term Hamiltonians were tested and table 3.7 shows the root mean square deviation for the Hamiltonians which have the smaller values (3, 7, 9, 19, 20). The root mean square deviations obtained in all twenty five possibilities are shown in table 5, in appendix A. It is observed that a very similar set of Hamiltonians as for ^{102}Zr have been found to provide the fits to the available data with smaller value of root mean square deviations. The calculated coefficients for this set of Hamiltonians are provided in table. 3.8. The table shows how the coefficients have a bigger value when calculated using the data of the isotonic chain, excluding k' in Hamiltonian 7 and λ in 20. The results of the energy calculations and the stronger associated transition probabilities for this set of Hamiltonians, using the data of the isobaric and isotonic chains, are plotted fig. 3.4 and fig. 3.5 respectively. As in the previous section the levels are grouped in bands; with the exception of Hamiltonians 7 and 19 which have some levels which do not appear to fit into a band structure, given that their associated transition probabilities are weak. They are easily recognizable because no transitions are indicated between them since the calculated value of those transitions are smaller than 0.9 e^2b^2. The complete set of calculated transition probabilities are in tables 6 and 7, in the appendix A. For ^{104}Zr, the only calculation which shows the β-band lower than the γ-band, is the one performed using the Hamiltonian 3 and the isotonic chain. Although one might expect that ^{104}Zr will have a β-band lower in energy than the γ-band, there are no data available at the moment which can confirm this hypothesis, so

	$\hat{n_d}$	$\hat{P}^\dagger\hat{P}$	$\hat{Q}^\chi\hat{Q}^\chi$	$\hat{L}\hat{L}$	$\hat{T}_3\hat{T}_3$	$\hat{T}_4\hat{T}_4$	$\hat{n_d}^2$	$\Delta(E)_N$ (keV)	$\Delta(E2)_N$ (me^2b^2)	$\Delta(E)_A$ (keV)	$\Delta(E2)_A$ (me^2b^2)
3	X	X	X		X			80	84	76	80
7	X		X	X	X			79	83	67	78
9	X		X		X	X		80	83	73	74
19	X		X	X			X	80	90	54	80
20	X		X		X		X	79	84	63	73

Table 3.7: ^{104}Zr. The minimum root mean square values obtained varying the parameters in Hamiltonians 3, 7, 9, 19, 20. From left to right: the first column assigns a number to each Hamiltonian; columns two to eight indicate which terms of the general Hamiltonian are considered in a particular calculation; finally, the last four columns show the root mean square for the energy levels and B(E2) values, the first two for the isobaric chain and the last two for the isotonic chain.

no Hamiltonian can be discarded.

Table 3.9 shows the main calculated B(E2) values as well as the only reduced transition probability in ^{104}Zr which has been experimentally measured. The calculated $2_1^+ \rightarrow 0_1^+$ transition probabilities are smaller than the experimental value. Although none of the values for this transition agree with the experimental data within one standard deviation, this result is not unexpected given that the $2_1^+ \rightarrow 0_1^+$ reduced transition probability value for ^{104}Zr is 0.2 units higher than the corresponding values for this transition of the rest of the nuclei considered in both chains, as is shown in table 3, appendix 6. The value of e_b needed to fit the $2_1^+ \rightarrow 0_1^+$ transition probability would have to be 0.12, 0.02 bigger than the calculated. This indicates the importance to measure other transition probabilities in ^{104}Zr. The table also shows a considerable difference between the predictions obtained using the two different chains, especially in the case of the two last transitions listed in the table.

Table 3.5 shows that there is a difference between the parameters obtained for the same Hamiltonian using different data sets and, therefore, for the energy levels calculated with the same Hamiltonian for the different chains. This is highlighted by the energy levels shown in figures 3.4 and 3.5 where the difference between

			Isotones	(N=64)			
	$\hat{n_d}$	$\hat{P}^\dagger\hat{P}$	$\hat{Q}^\chi\hat{Q}^\chi$	$\hat{L}\hat{L}$	$\hat{T}_3\hat{T}_3$	$\hat{T}_4\hat{T}_4$	${\hat{n_d}}^2$
3	1.2114	0.0394	-0.0545		-0.2167		
7	1.2038		-0.0586	-0.0013	-0.2275		
9	1.1532		-0.0595		-0.2379	0.0289	
19	1.159		-0.0440	0.0176			-0.1412
20	1.1611		-0.0559		-0.2066		-0.0071
			Isobars	(A=104)			
	$\hat{n_d}$	$\hat{P}^\dagger\hat{P}$	$\hat{Q}^\chi\hat{Q}^\chi$	$\hat{L}\hat{L}$	$\hat{T}_3\hat{T}_3$	$\hat{T}_4\hat{T}_4$	${\hat{n_d}}^2$
3	0.7948	-0.0186	-0.0394		-0.1098		
7	0.9490		-0.0447	-0.0026	-0.1443		
9	0.8030		-0.00408		-0.1297	0.0348	
19	0.8681		-0.0385	0.0123			-0.0991
20	0.9604		-0.0459		-0.1285		-0.0203

Table 3.8: The value of the coefficients for the Hamiltonians 3, 7, 9, 19 and 20 in the ^{104}Zr calculation. The first column assigns a number to each Hamiltonian; columns two to the eight indicate the different terms of the general Hamiltonian considered in a particular calculation.

the calculated energies for each chain can be seen. The calculation performed with the data in the isobaric chain gives a lower energy for the 2_1^+, 4_1^+ and 6_1^+ energy levels than the ones calculated with the isobaric chain (and also than the experimental values), while the rest of the states are predicted to have a higher energy in the calculation performed with the data of the isotonic chain.

	Isobars (A=104)					
Transition	Experimental	H_3	H_7	H_9	H_{19}	H_{20}
$2_1^+ \to 0_1^+$	0.5301(796)	0.3297	0.3384	0.3192	0.3569	0.3558
$4_1^+ \to 2_1^+$		0.4797	0.4863	0.4641	0.4974	0.5078
$2_2^+ \to 0_2^+$		0.0222	0.0218	0.0226	0.0114	0.0205
$2_3^+ \to 0_2^+$		0.2244	0.2380	0.2212	0.2404	0.2509
	Isotones (N=64)					
Transition	Experimental	H_3	H_7	H_9	H_{19}	H_{20}
$2_1^+ \to 0_1^+$	0.5301(796)	0.3508	0.3473	0.3399	0.2592	0.3499
$4_1^+ \to 2_1^+$		0.4932	0.4881	0.4781	0.3564	0.4929
$2_2^+ \to 0_2^+$		0.0026	0.0016			
$0_2^+ \to 2_2^+$				0.0466	0.0069	0.0071
$2_3^+ \to 0_2^+$		0.0569	0.0310	0.2043	0.0777	0.0316

Table 3.9: Experimental and theoretical B(E2) values (in units of e^2b^2) for transitions in ^{104}Zr. The upper half of the table shows the results calculated by fitting the parameters to the isobaric chain while the bottom half shows the predictions obtained by fitting the parameters to the isotonic chain. A value of $e_b = 0.1$ has been used in all the cases.

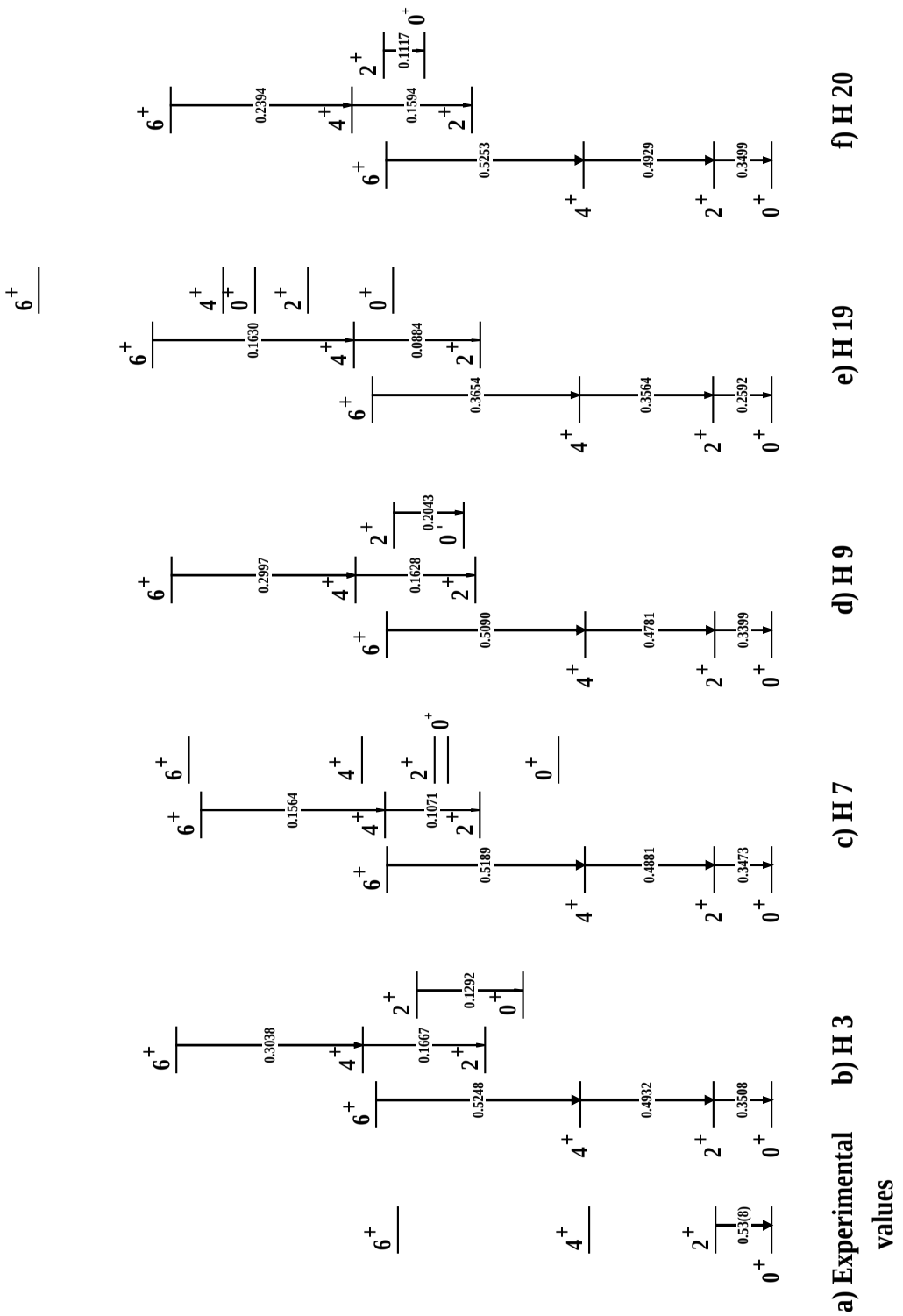

Figure 3.4: Experimental and theoretical energy levels of ^{104}Zr. The parameters in each Hamiltonian are obtained by minimizing the rms deviation with respect to the energy levels of the isotonic chain. The levels are grouped in bands according to the calculated transition probabilities, which are given in units of e^2b^2.

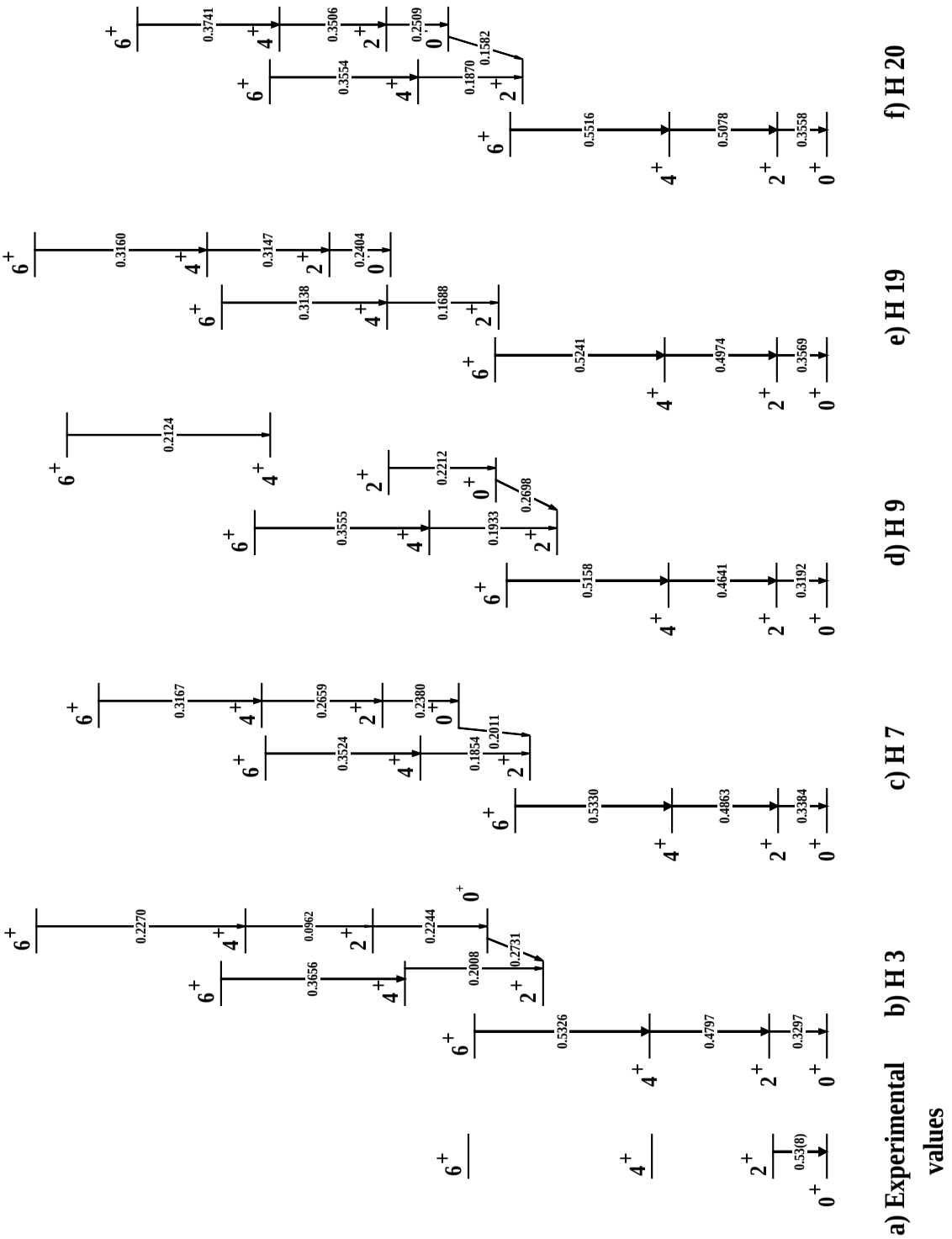

Figure 3.5: Experimental and theoretical energy levels of ^{104}Zr. The parameters in each Hamiltonian are obtained by minimizing the rms deviation with respect to the energy levels of the isobaric chain. The levels are grouped in bands according to the calculated transition probabilities, which are given in units of e^2b^2.

3.4 Results for ^{106}Zr:

In the case of ^{106}Zr the data used for the isotonic chain (N=66) includes the nuclei: ^{112}Pd, ^{110}Ru, ^{108}Mo and ^{106}Zr, and for the isobaric chain (A=106): ^{106}Ru, ^{106}Mo and ^{106}Zr. The experimental data used in this fit is shown in table 8 (B(E2)s) and table 9 (energy levels), in appendix A. The values of e_b and χ calculated with these data are 0.09 and -0.3 respectively. The value of e_b is slightly lower than in the two previous cases but the value of χ is the same as for ^{104}Zr.

Table 3.10 shows the Hamiltonians with smaller root mean square standard deviations for both chains, while the results for all the tested Hamiltonians are shown in table 10 of appendix A. The Hamiltonians which provide lower root mean square values are: 2, 3, 7, 9, 19 and 20 and their coefficients are shown in table 3.11. Therefore, there is a set of Hamiltonians (3, 7, 9 and 19) providing lower rms values common to the three zirconium isotopes.

Figures 3.6 and 3.7 show the energy levels obtained by varying the parameters in each Hamiltonian to minimize the rms energy using the data in the isotonic (N=66) and isobaric (A=106) chains respectively, as well as the stronger transition probabilities. The main calculated reduced transition probabilities for the chosen Hamiltonians are shown in table 3.12. As in the previous cases, the calculations made with the two chains provide different results; but there is no experimental data available to compare them with. All the calculated transition probabilities are shown in tables 12 and 13, in appendix A. The levels shown are grouped into bands except for some set of no bands levels shown for the calculation performed with the isobaric chain and the Hamiltonian 19. The figures clearly show that the calculations performed with the isotonic chain gives a better fit to the energies of the ground state band than the calculations performed using the isobaric chain. The latter produces notably lower energies than the experimentally observed yrast levels and gives higher energy levels than fig. 3.6 for non-yrast states. All the calculations performed with the isobaric chain present a β-band lower in energy than the γ-band, as do the calculations performed with Hamiltonians 3, 7 and 9 and the isotonic chain.

	$\hat{n_d}$	$\hat{P}^\dagger\hat{P}$	$\hat{Q}^\chi\hat{Q}^\chi$	$\hat{L}\hat{L}$	$\hat{T}_3\hat{T}_3$	$\hat{T}_4\hat{T}_4$	$\hat{n_d}^2$	$\Delta(E)_N$ (keV)	$\Delta(E2)_N$ (me^2b^2)	$\Delta(E)_A$ (keV)	$\Delta(E2)_A$ (me^2b^2)
2	X	X	X	X				68	143	88	138
3	X	X	X		X			64	148	86	152
7	X		X	X	X			62	145	87	150
9	X		X		X	X		56	166	89	149
19	X		X	X			X	53	164	98	121
20	X		X		X		X	61	142	87	151

Table 3.10: ^{106}Zr. The minimum root mean square values obtained by varying the initial parameters in Hamiltonians 2, 3, 7, 9, 19, 20. From left to right: the first column assigns a number to each Hamiltonian; columns two to the eight indicate which terms of the general Hamiltonian are considered in a particular calculation; finally, the last four columns show the root mean square for the energy levels and B(E2) values, the first two for the isotonic (N=66) chain and the last two for the isobaric (A=106) chain.

			Isotones	(N=66)			
	$\hat{n_d}$	$\hat{P}^\dagger\hat{P}$	$\hat{Q}^\chi\hat{Q}^\chi$	$\hat{L}\hat{L}$	$\hat{T}_3\hat{T}_3$	$\hat{T}_4\hat{T}_4$	$\hat{n_d}^2$
2	0.8652	0.2502	0.0361	0.0178			
3	1.2325	0.1067	-0.0246		-0.1456		
7	0.9585		-0.0313	0.0032	-0.1413		
9	1.1716		-0.0244		-0.0712	-0.1348	
19	0.7297		-0.0201	-0.0160			-0.0622
20	0.9980		-0.0315		-0.1725		-0.0173
			Isobars	(A=106)			
	$\hat{n_d}$	$\hat{P}^\dagger\hat{P}$	$\hat{Q}^\chi\hat{Q}^\chi$	$\hat{L}\hat{L}$	$\hat{T}_3\hat{T}_3$	$\hat{T}_4\hat{T}_4$	$\hat{n_d}^2$
2	1.2130	0.5273	0.0396	0.0133			
3	0.9558	0.0685	-0.0385		-0.1297		
7	0.9168		-0.0434	-0.0008	-0.1432		
9	0.8681		-0.0431		-0.1431	0.0164	
19	1.1124		-0.0472	0.0166			-0.1457
20	0.9039		-0.0428		-0.1355		-0.0042

Table 3.11: The value of the coefficients for the Hamiltonians 2, 3, 7, 9, 19 and 20 in the ^{106}Zr calculation. The first column assigns a number to each Hamiltonian; columns two to the eight indicate the different terms of the general Hamiltonian considered in a particular calculation.

	Isobars (A=106)					
Transition	H_2	H_3	H_7	H_9	H_{19}	H_{20}
$2_1^+ \to 0_1^+$	0.2708	0.3353	0.3273	0.3211	0.2066	0.3302
$4_1^+ \to 2_1^+$	0.3814	0.4767	0.4656	0.4574	0.2856	0.4697
$0_2^+ \to 2_2^+$	0.1436	0.1343	0.1124	0.1224	0.0095	0.1130
$2_3^+ \to 0_2^+$	0.2124	0.2418	0.2349	0.2297	0.0607	0.2372
	Isotones (N=66)					
Transition	H_2	H_3	H_7	H_9	H_{19}	H_{20}
$2_1^+ \to 0_1^+$	0.2360	0.3015	0.2829	0.3579	0.3522	0.2628
$4_1^+ \to 2_1^+$	0.3433	0.4396	0.4173	0.5028	0.4949	0.3920
$0_2^+ \to 2_2^+$		0.2301	0.1697	0.0764		0.1854
$2_2^+ \to 0_2^+$	0.0322				0.0212	
$2_3^+ \to 0_2^+$	0.1761	0.2211	0.2015	0.2430	0.2334	0.1935

Table 3.12: Calculated B(E2) values (in units of e^2b^2) for transitions in ^{106}Zr. The upper half of the table shows the calculations made with the isobaric chain data while, the bottom half shows the results obtained with the isotonic chain data. A value of $eb = 0.09$ was used in all the cases.

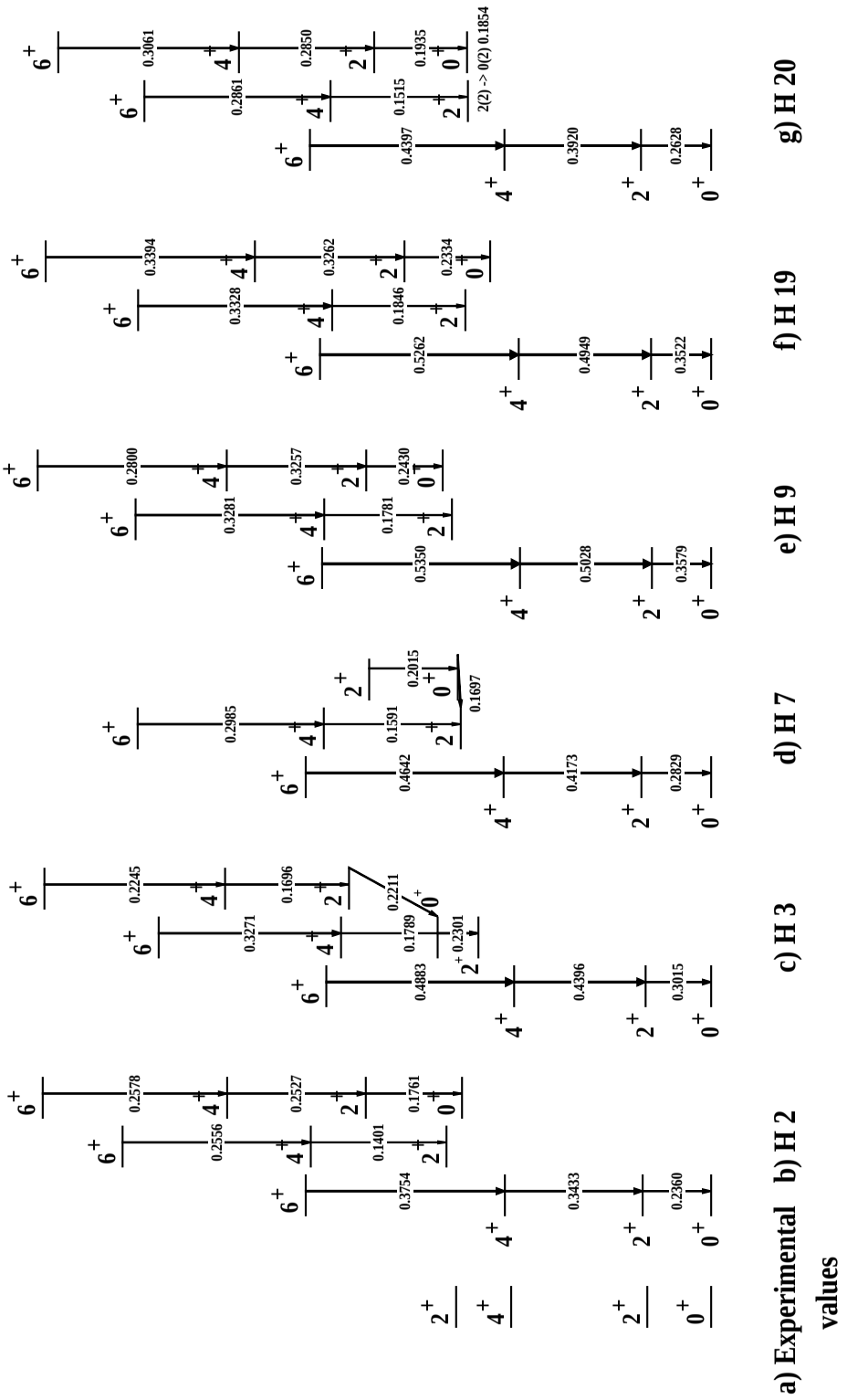

Figure 3.6: Experimental and theoretical energy levels of ^{106}Zr. The parameters in each Hamiltonian are obtained by minimizing the rms deviation with respect to the energy levels of the isotonic chain. The levels are grouped in bands according to the calculated transition probabilities, which are given in units of e^2b^2.

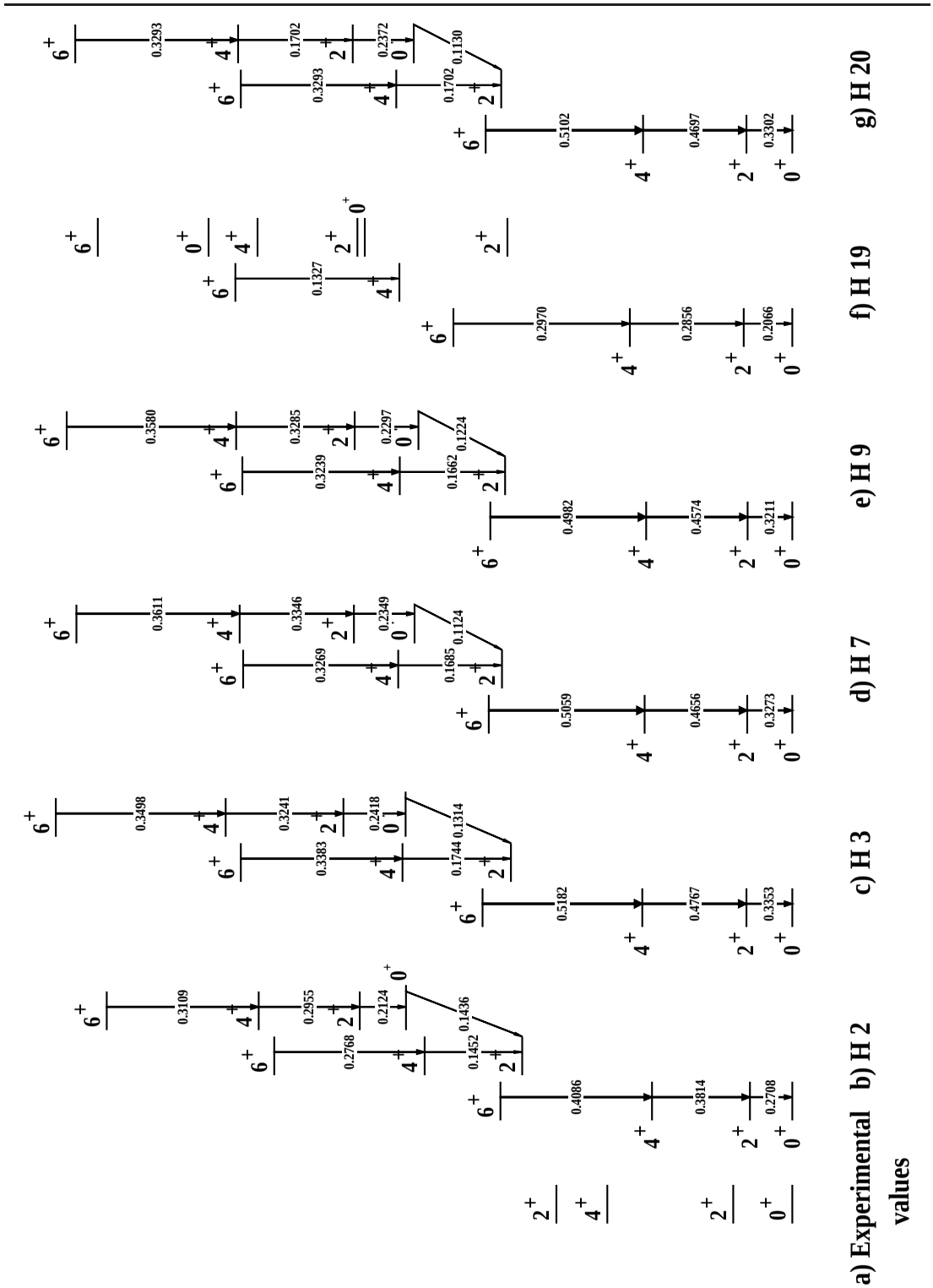

Figure 3.7: Experimental and theoretical energy levels of ^{106}Zr. The parameters in each Hamiltonian are obtained by minimizing the rms deviation with respect to the energy levels of the isobaric chain. The levels are grouped in bands according to the calculated transition probabilities, which are given in units of e^2b^2.

3.5 Conclusions:

After examining the results for $^{102-104-106}$Zr, it is observed that there is a clear dependence of this method on the available experimental data. All the results discussed in this chapter for the three nuclei considered show definite differences depending on whether the isobaric or isotonic chain data are used. It is also important to highlight the fact that because the IBM depends strongly on the number of bosons, all the calculations depend on the definition of closed shells, and therefore the existence of magic numbers in this region of deformation is assumed. Finally, all the cases show a strong dependence on the Hamiltonian chosen. For the three isotopes a similar set of four-term Hamiltonians was found to produce the best results in terms of standard deviation and, in fact, tables 3.4, 3.7 and 3.10 show that there are four Hamiltonians which were selected for all of the nuclei: 3, 7, 9 and 19. All these Hamiltonians contain the two terms: $\epsilon\hat{n_d}$ and $\kappa\hat{Q}^{\chi}$. The first of these is inherent of a vibrator and, the second one is inherent to a symmetric rotor.

The nuclei of this region are know for having a structure in which the band-head of the beta-band has an energy lower than the band-head of the gamma-band. The calculations for ^{102}Zr showed that only the results obtained using the Hamiltonian 7 calculate a beta band which is lower than the gamma band for both chains (isotonic and isobaric) of data. Therefore this is the best Hamiltonian for this nucleus. Given that there is no data about non-yrast states of $^{104-106}$Zr it is not possible to extent this argument. Even if we assume that the beta band will be lower than the gamma band for $^{104-106}$Zr, the results are still inconclusive. Only Hamiltonian 3 combined with the isotonic chain gives such a result for ^{104}Zr, while Hamiltonians 2, 19 and 20 combined with the isotonic chain do so in the case of ^{106}Zr.

Therefore, it is important to collect new data in order to refine these calculations to provide a better interpretation of the nuclear structure of zirconium in the IBM context. An increased set of data will hopefully contribute to choosing one Hamiltonian over the others, and will provide a useful tool in order to study the

changes in the nuclear shape due to the shell configurations, and thus the nuclear structure.

3.6 Extension to ^{108}Zr

A recent measurement of ^{108}Zr [17] has produced the level scheme shown in fig. 3.8. In order to compare this new data with the theory, a series of calculations have been performed. Given the small amount of experimental data available in this case, calculations are more tricky than for the previous zirconium isotopes considered. Therefore two different approaches have been tested: On one hand, it is possible to make an extrapolation of the parameters for a given Hamiltonian, based on the results for ^{102,104,106}Zr. As discussed in the previous section, there are four Hamiltonians which were selected for all of the zirconium nuclei studied: 3, 7, 9 and 19, therefore these are the only ones considered for ^{108}Zr. Unfortunately, this method is only available for the first three, since the ibm code, which calculates the energy states for a given set of parameters, only contains Hamiltonians of the form 3.2. Fig. 3.9 shows the evolution of the parameters of Hamiltonian 7, as a function of the mass number. The values of the parameter for ^{102,104,106}Zr are shown in black, while the extrapolated values to ^{108}Zr are shown in red. The difficulty in extrapolating the parameters to ^{108}Zr is that we only have three masses to try to establish a systematic trend. Inputting these parameters into the programs provides results for both energy levels and transitions. Due to the lack of experimental data, it is not possible to calculate the values for e_b and χ as before, and therefore it has been decided to use the same ones as in the case of ^{106}Zr.

Alternatively it is possible to use fiti to made a calculation based on the data available for the zirconium isotopic chain (^{102,104,106,108}Zr) in the same way as discussed in previous sections. Given the lack of experimental information for reduced transition probabilities in this chain, it was decided that the values of e_b=0.09 and χ=-0.3 would be used, as they were the values obtained for ^{106}Zr. The Hamiltonians used were 3, 7, 9 and 19, as in the previous case. Together both

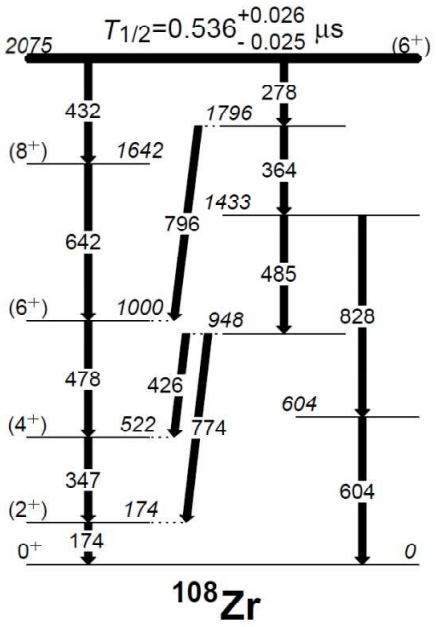

Figure 3.8: Proposed level scheme of ^{108}Zr [17].

methods provide seven possible outcomes which have been compared with the experimental data shown in fig. 3.8 [17]. Based on this comparison, it has been concluded that the best calculation uses Hamiltonian 7 and the isotopic chain experimental data. Fig. 3.9 shows these parameters in blue. There is a clear difference between these coefficients and the extrapolated ones (shown in red). The difficulty of fitting the parameters by minimizing the standard deviation is the small amount of data, which for three of the four nuclei in the isotopic chain, consists only of the low spin energy levels of the ground state band. Therefore one would expect larger discrepancy between theory and experimental data for states of higher spin and energy.

Fig. 3.10 shows the results of fitting Hamiltonian 7 to the experimental data in the isotopic chain. The first two bands in the theoretical level scheme have been arranged to emulate the experimental data shown in fig. 3.8. These two bands are extremely similar to the ones obtained with pure SU(3) symmetry. In fact the calculations provide an almost perfect rotational ground state band

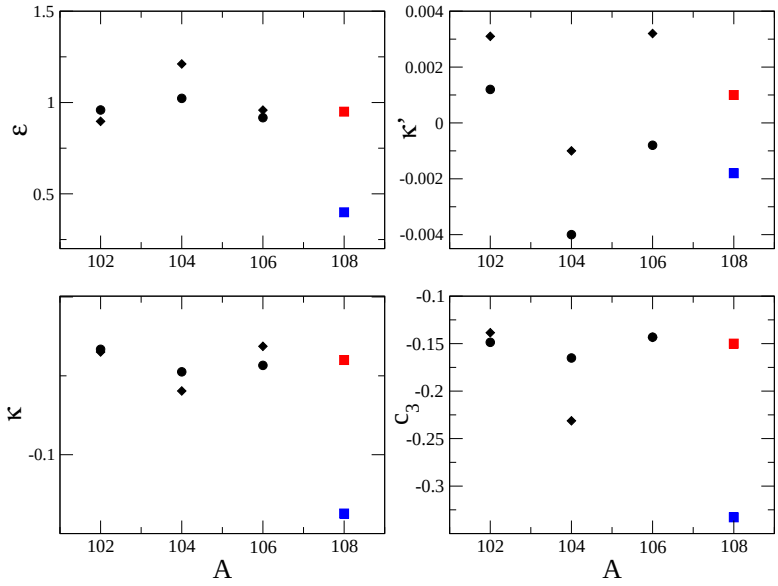

Figure 3.9: Calculated coefficients, in keV, of the Hamiltonian 7 for ^{102,104,106}Zr (black); extrapolated coefficients to ^{108}Zr (red) and, calculated coefficients for ^{108}Zr (blue).

with $R_{4/2}^{IBM}$=3.35, while the experimental data provides a 'less rotational' value, $R_{4/2}^{exp}$=3. Fig. 3.10 also shows a third set of states represented by dotted lines, which is not a property of a rotational object. Even if it is possible arrange the energy levels in a way to correspond to the first two bands of the figure with the ground state and γ bands, there is no similarity between the third band and the beta band described in sec. 2.1.3.

The most striking feature of fig. 3.8 is the measurement of an isomeric 6^+ state of $T_{1/2}$=0.536(26) μs. Shi *etal.* at [56] have explained this isomeric state as a two quasineutron state of high K-value. In an extension of previous configuration-constrained potential-energy-surface calculations [49], a possible K-isomeric state of K^π=6^+ and energy of 1.997 MeV is calculated, in good agreement with the experimental data. Other authors point out the possibility that this state is an isomer due to a tetrahedral shape [20]. Using the ibmt code and assuming that this isomeric state is the second 6^+ state, E2 transition probabilities for the $6_2^+ \rightarrow 8_1^+$ and $6_2^+ \rightarrow 5_1^+$ transitions have been calculated and are shown in

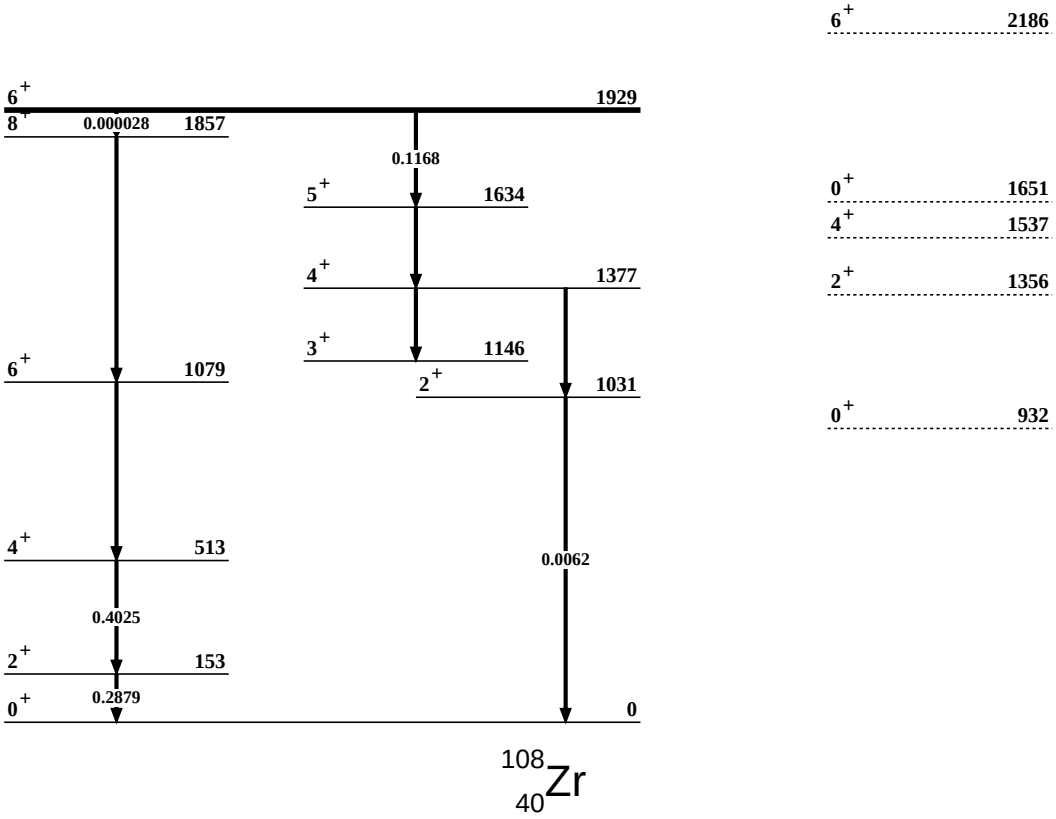

Figure 3.10: Calculated level scheme of ^{108}Zr. The labels at the arrows indicate calculated E2 transition probabilities in units of e^2b^2.

fig. 3.10. Although the value of B(E2:$6_2^+ \rightarrow 8_1^+$) is very small, that is not the case for the B(E2:$6_2^+ \rightarrow 5_1^+$). Using equation 2.13 shown in section 4.3, the calculated B(E2:$6_2^+ \rightarrow 5_1^+$) and the calculated energy difference betwen the 6_2^+ level and the 5_1^+ level as the energy of the gamma-ray transition between both, a half-life of 2.17 ns has been calculated for the 6_2^+ energy state. The transition $6_2^+ \rightarrow 8_1^+$ has not been taken in account due to its small probability. Although this value does not agree with the measured half life for the 6_2^+ [17], one should consider that the calculations are base on the level scheme shown in fig. 3.8 which is the only data published at the present. Recently, other measurements of ^{108}Zr have taken place at RIKEN during the experiment NP 0702 RIBF26. The result of this research will enlighten our knowledge of the structure of ^{108}Zr and provide a new test of the calculations presented in this chapter.

Chapter 4

Experimental Method

This chapter is structured in three parts: Section 4.1 explains the IGISOL III facility, where the zirconium isotopes are planned to be measured; section 4.2 explains why it is possible to perform this research using the IGISOL facility; finally, section 4.3 explains the post-trap on line spectroscopy technique, that will be used in the forthcoming attempts to measure zirconium at IGISOL IV, and presents the results of using this method in the case of ^{100}Mo.

The zirconium isotope of interest for the present work is ^{102}Zr. Levels in ^{102}Zr have been studied subsequent to the beta decay of ^{102}Y [21, 57, 58], uranium induced fission [16, 59] and spontaneous fission of californium [60, 61]. The beta decay studies have been complicated because of the existence of two decaying states with very similar half lives in ^{102}Y: a low spin state ($T_{1/2}$=0.30(1) s) [57] and a high spin one ($T_{1/2}$=0.36(3) s) [58]. Therefore, a method able to distinguish between the decay of the two states is needed. A new technique to separate different states of nuclei has recently been developed [23], at the IGISOL facility of the University of Jyväskylä. This now has been extended and applied for the first time with gamma spectroscopy, in a proof of principle experiment for the well known decay of the two states of ^{100}Nb into ^{100}Mo [18]. It is proposed that further experiments will produce a beam of a single state of ^{102}Y, in a similar way to the one used to produce the two separate states of the ^{100}Nb, so the separate

measurement of the different decay paths will be possible.

4.1 IGISOL III

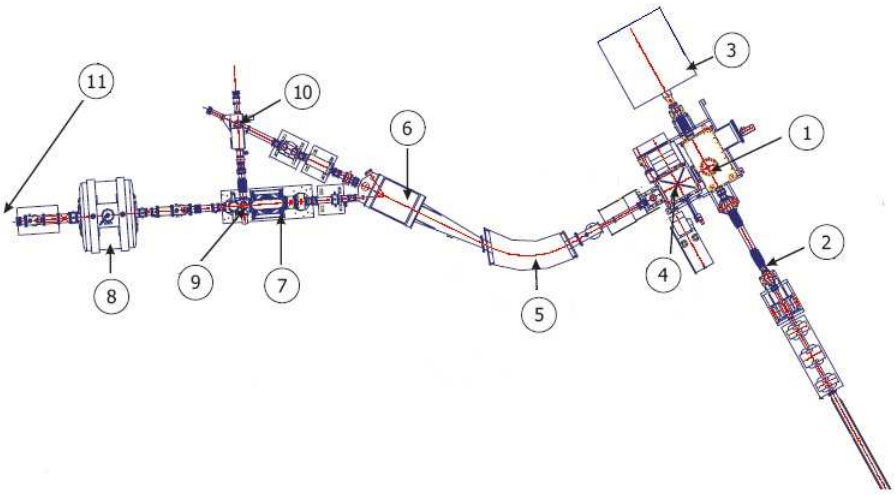

Figure 4.1: Layout of the IGISOL facility. The following parts are numbered:1) target chamber, 2) primary beam line, 3) beam dump, 4) extraction chamber, 5) dipole magnet, 6) beam switchyard, 7) RFQ cooler and buncher, 8) Penning traps, 9) four-way quadrupole deflector, 10) beam line to collinear laser set-up, and 11) detector set-up location (adapted from [62]).

The nuclei of interest are produced at the Ion Guide Isotope Separator On-Line (IGISOL III) facility at the University of Jyväskylä, Finland [63]. Fig. 4.1 shows a layout of the facility. A proton primary beam is produced in an ion source and accelerated by the K-130 cyclotron. Protons are impinged, through the primary beam line (labelled as 2 in fig. 4.1) on a thin target (1 in the figure) producing a fission reaction. Fission products recoiling from the target are thermalised, stopped and converted into 1^+ ions by a helium buffer gas. Following extraction from the gas cell, ions are transported through a radiofrequency sextupole device (SPIG) [64] (situated between the target and the extraction chambers) to the extraction

chamber (labelled as 4 in fig. 4.1). From the extraction chamber, the secondary beam is subjected to a first mass selection inside the dipole magnet (5), before it enters the swichyard (6), to be transferred into the ion beam cooler-buncher (RFQ) (labelled as 7 in fig. 4.1) [65] . Inside the RFQ, ions are thermalised, bunched and injected into the JYFL double Penning trap (8 in the figure) [66]. Here, the mass of the ions is selected using Ramseys technique [67], which allows the selection of the mass by selecting the frequency of the radiofrequency fields. After the JYFLTRAP, several detection set ups are possible (11).

4.1.1 Principle of the ion guide method

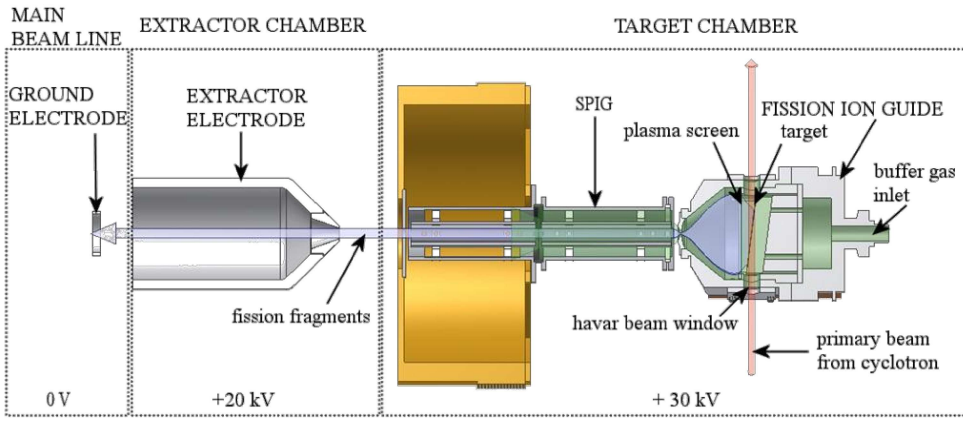

Figure 4.2: Fission ion guide and extraction system (SPIG + extraction electrode) [68].

Fig. 4.2 shows the fission ion guide placed in the target chamber alongside the SPIG and the extraction electrode. The primary beam enters the ion guide by the havar beam window. Radioactive nuclei are produced in a fission reaction and recoil out of the thin production target. The fact that the fission products are produced with an almost isotropic spatial distribution, makes it possible to separate them from the incident primary beam. Some of them travel through the plasma screen and are stopped in a helium-filled chamber, where they lose kinetic energy by collisions with the gas (thermalization). Thereupon, the products are transported, due to the gas flow, out of the gas cell. This same gas flow is

responsible for guiding the ions, through the radio frequency sextupole, SPIG, into the beam line of the mass separator [64]. After the SPIG, the ions are guided through the extraction electrode into the secondary beam line. Although some buffer gas is always going into the SPIG with the produced ions, the diffusion oil pumps drain the helium out.

4.1.2 JYFLTRAP

In addition to the ion guide, the most important component of the IGISOL is the JYFLTRAP [66]. It consists of a radiofrequency quadrupole cooler and two Penning traps (labelled as 7 and 8 respectively on fig. 4.1) inside a superconducting solenoid [23].

4.1.3 Ion beam cooler

Prior to entering the RFQ-cooler, the kinetic energy of the ions in the beam is reduced from 30 keV to about 100 eV. The RFQ-cooler is an ion trap which confines the ions using only electric fields, following the principle of a segmented linear Paul trap [69]. The device is filled with helium gas (0.01-0.1 mbar) so the ions entering the cooler are thermalized. The combination of the buffer gas with the quadrupole field has the effect of cooling and centering the ions, which are accumulated around the trap axis, directed to the exit of the RFQ-cooler [65] and extracted as bunches.

4.1.4 Penning Trap system

In the JYFLTRAP, two Penning traps are used. The first Penning trap, the purification trap, is used for isobaric cleaning and the second Penning trap, the precision trap, is used for isomeric cleaning and high precision mass measurements [23]. The main difference between the two traps is that the purification trap is filled with a buffer gas (helium) while the precision trap is situated in ultra-high

vacuum ($<10^{-7}$ mbar). Further information on the effect of the buffer gas can be founded in reference [69].

Fig. 4.3 represents the motion of a charged particle in a Penning Trap. A magnetic field confines the particles in the radial direction (ρ), while the axial direction (z) confinement is executed by an electrostatic quadrupole field. The motion of the ions inside the trap is a combination of an axial motion, which constitutes an oscillation around the trap centre, and a radial motion, which can be expressed as a sum of two independent eigenmotions: the magnetron motion with frequency ω_+ and the reduced cyclotron motion with frequency ω_- [66]. Both eigenmotions are circular in the plane perpendicular to the magnetic field (which is equal to the trap axis). Since the cyclotron frequency given by $\omega_c = qB/m$ (where q is the charge of the ion, m is its mass and B is the external magnetic field) can be written as the sum of both frequencies ω_+ and ω_-, determining the frequency ratio of two ions, one of interest and one of calibration, will allow the measurement of the mass of the first one.

Ion motion can be manipulated by applying azimutal multipole RF fields. A

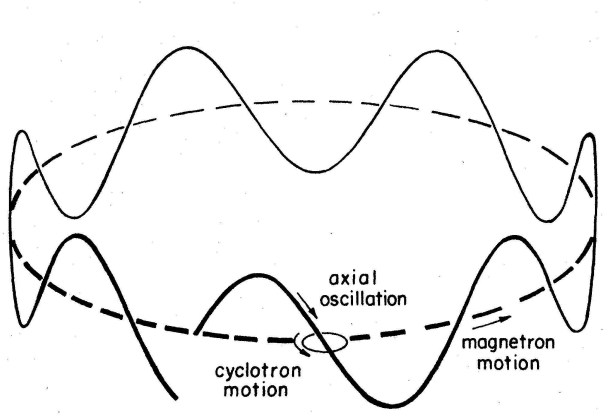

Figure 4.3: The orbit of an ion inside the Penning Trap. The dashed line represents the magnetron component of the motion. The movement produced by the sum of the axial oscillation about the radial plane plus the magnetron component is represented by the solid line. Adding the cyclotron motion to the sum, the total motion of the ion is obtained. The whole movement can be visualized as a cyclotron oscillation about the solid line. (Taken from [70])

dipole field can be used to remove one (or all) of the ion species from the centre of the trap. A quadrupole field can be used to excite the ion motions at sums or differences of the frequencies ω_+ and ω_- and to convert one motion into the other [71]. Since the quadrupole excitation of the cyclotron frequency is strongly mass dependent, it is possible to centre a single ion species and extract it through a small window situated in the central axis of the trap. Also, in the last years, the Ramsey technique [67], which excites the ions with time-separated oscillatory fields, has been introduced to the JYFLTRAP [23]. This has been used to produced isomerically pure beams with mass resolving power greater than 10^5 [23].

4.2 Measuring zirconium with the IGISOL:

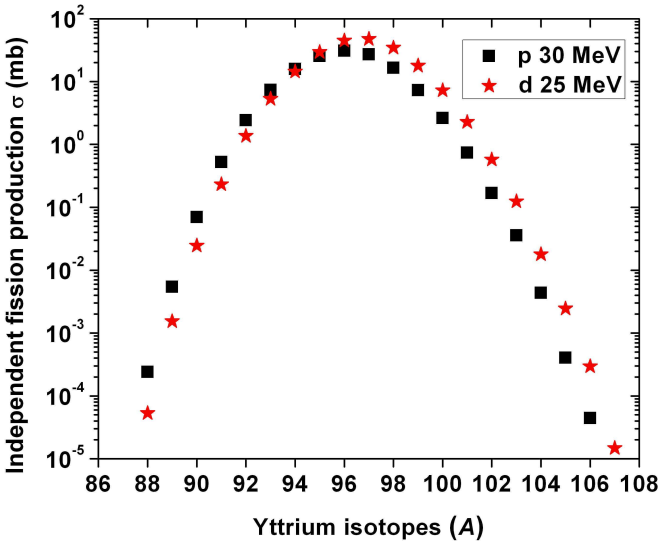

Figure 4.4: A theoretical comparison between the production cross section for proton and deuteron-induced fission for Yttrium isotopes [72].

The first attempt to measure $^{102-106}$Zr at IGISOL III was made in November 2009. Previously to this experiment, the possible rates of production for $^{100-104}$Zr were estimated using a series of calculations by V. A. Rubchenya [72] and yield

measurements of masses A=100, 102, 104.

Fig. 4.4 shows the results of such a calculation for the relative population of Yttrium isotopes. For isotopes with mass number grater than 98, the theoretical predictions indicate an expected increase in the cross section of the fission production, using deuteron-induced fission rather than proton-induced fission. However, the measurements, of the relative production of $^{100-104}$Zr using 30 MeV proton and 25 MeV deuteron-induced fission, did not show relevant difference. In the case of the proton beam, the ratio of the intensities of the $2^+ \rightarrow 0^+$ transitions is 1:0.129:0.007 for A=100, 102, 104 respectively; for deuterons, it is 1:0.104:0.005. Fig. 4.5 shows the spectra collected, after the switchyard, during the yield measurements with the proton beam. The $2^+ \rightarrow 0^+$ gamma-ray transition energies in $^{100-104}$Zr are 212.5, 151.7 and 139.9 keV. The beam current was 5μA and the rate of emitted $2^+ \rightarrow 0^+$ gamma-rays in ^{102}Zr was 600 per second. The diagram shows a clear need for the high resolution cleaning of the Penning trap.

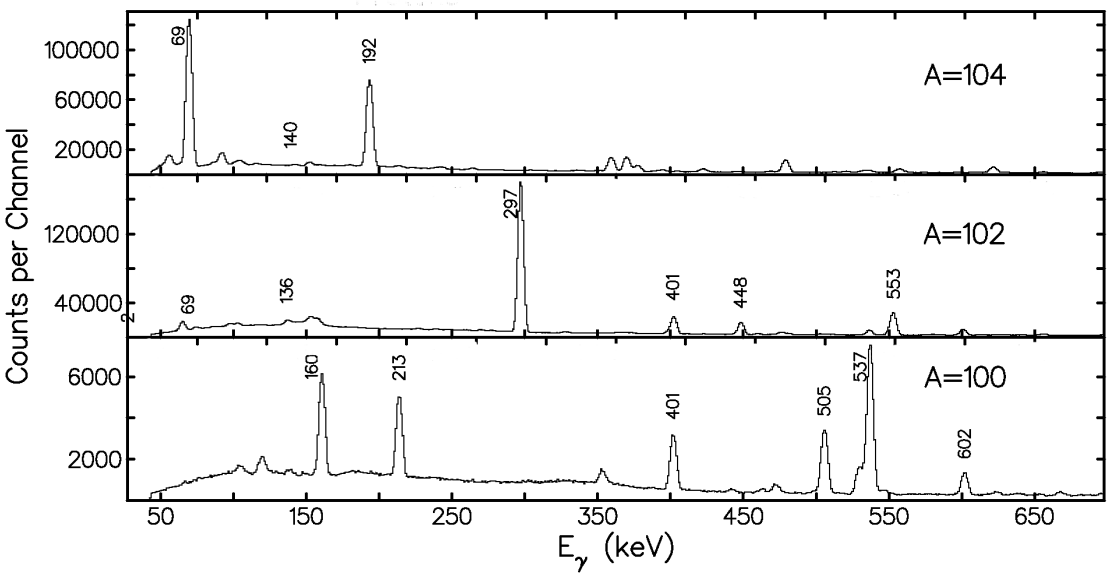

Figure 4.5: Gamma-ray spectra yield measurements for A=100, 102, 104 at IGISOL III [73].

The experimental time to measure ^{102,104}Zr was scheduled at the IGISOL III in November 2009 and February 2010. Unfortunately it was not possible to extract useful intensities of yttrium beam in either experiment. The problem was not discovered until later when, during the transfer of the IGISOL to the new experimental hall, an oil leak in the IGISOL roots blower system was discovered. This caused contamination of the beam line with oil, leading to poisoning of the radioactive species. As yttrium is a highly chemically reactive element, the extraction of yttrium beams with enough intensity to perform the experiment was impossible. In those circumstances, a proof of principle experiment was executed instead. Such an experiment tested the possibility of combining the JYFLTRAP isomer cleaning technique with gamma-spectroscopy, and is explained in detail in the following section.

4.3 Trap-assisted gamma-ray spectroscopy. The ^{100}Mo case

Low-lying levels in ^{100}Mo are known to be populated by beta decay from ground ($J^\pi = 1^+$) and isomeric ($J^\pi = 5^+$) states in ^{100}Nb. Fig. 4.6 shows the decay scheme of ^{100}Nb into ^{100}Mo and contains only the gamma rays measured during this experiment. The β-feeding from both parent states is also indicated. The small energy difference between the two parent states of 313(23) keV [74] and the similarity of their half lives (1.5(2)s [37] for the ground state and 3.0(1)s [75] for the isomer) make it difficult to distinguish experimentally between the two decay paths. Therefore, a technique able to separate the different states of ^{100}Nb is needed and, thus, constitutes an ideal case to test the online post-trap spectroscopy method.

The ^{100}Nb nuclei were produced at the IGISOL via proton induced fission. The proton beam was accelerated to 30 MeV in the K-130 cyclotron and impinged on a Uranium target of effective thickness 123 mg/cm^2. Section 4.1 explains how fission products recoiling from the target were transported out to the gas

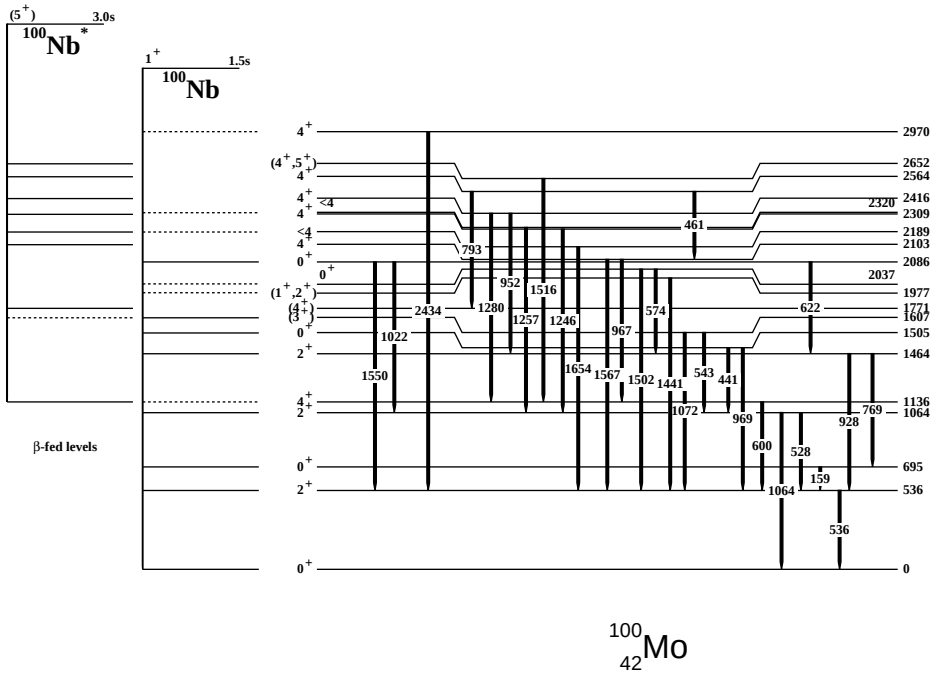

Figure 4.6: A schematic of the beta decay of ^{100}Nb isomeric and ground states into levels in ^{100}Mo. Levels with β-feeding lower than 3% are represented by dotted lines. Spins and energies of the levels are taken from [37].

cell, through the SPIG, to the JYFLTRAP. Fig. 4.7 shows one of the mass-scans performed with the second Penning trap in order to determine the frequency needed to select ions of ^{100}Nb in the ground state and in the isomeric state. In this case, the ^{100}Nb ground state is expected at a frequency of 1075395 Hz, and the ^{100}Nb isomeric state at 1075391 Hz. The Nb and Nb* labels indicate the frequencies at which these masses are expected with the small energy difference (313 keV) corresponding to a separation in the frequency of 3.6 Hz. The A=100 Mo peak is expected a further 74 Hz away but due to the timing pattern used in the Ramsey technique, peaks are repeated every 16 Hz [23]. The Mo peak observed in fig. 4.7 is therefore the fourth 'repeat' peak, expected 10 Hz from the Nb peak. The spectrum shows a clear separation between ^{100}Nb and ^{100}Mo but also, the close proximity of both states in Nb, which makes the experiment difficult. Many frequency scans in the precision trap were performed in order to ascertain the frequency to optimize the extraction of a purified ion sample.

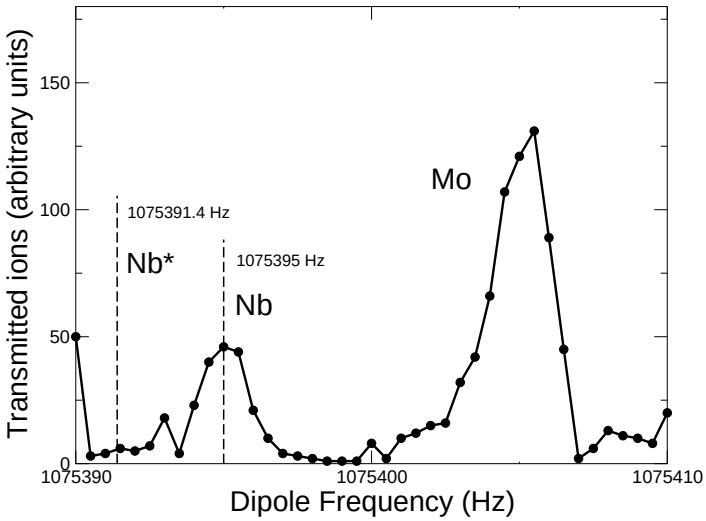

Figure 4.7: The number of transmited ions, in arbitrary units, as a function of dipole frequency in the precision trap. The dotted straight lines show the frequency where nuclei in the ground state (1075395 Hz) and in the isomeric state (1075391.4 Hz) were expected.

The beam exits the JYFLTRAP and is implanted in an aluminium stopper. Since the ions travel down the pipe with very small kinetic energy, they can be stopped in a deposition point. Two separate measurements were performed. One, at 1075395 Hz, where the ions were implanted during 3 s and, allowed to decay for an other 3 s before the reopening of the trap. The other measurement, at 1075391 Hz, was set up with a cycle of 6 s implantation/ 6 s decay.

A 3π cylindrical beta detector and three germanium detectors (two clover detectors at 90° and 270°, and one LOAX at 180°) were placed surrounding the deposition point. The beta detector was a 2 mm thick plastic scintillator.

4.3.1 Gamma-ray spectroscopy

The gamma-ray detectors were energy calibrated using two different sources, each one placed at the deposition point for ten minutes. One source was a mixture of

^{133}Ba and ^{152}Eu. The other was composed of ^{241}Am, ^{139}Ce, ^{60}Co. With these two specimens an energy range from 59 keV to 1408 keV was covered.

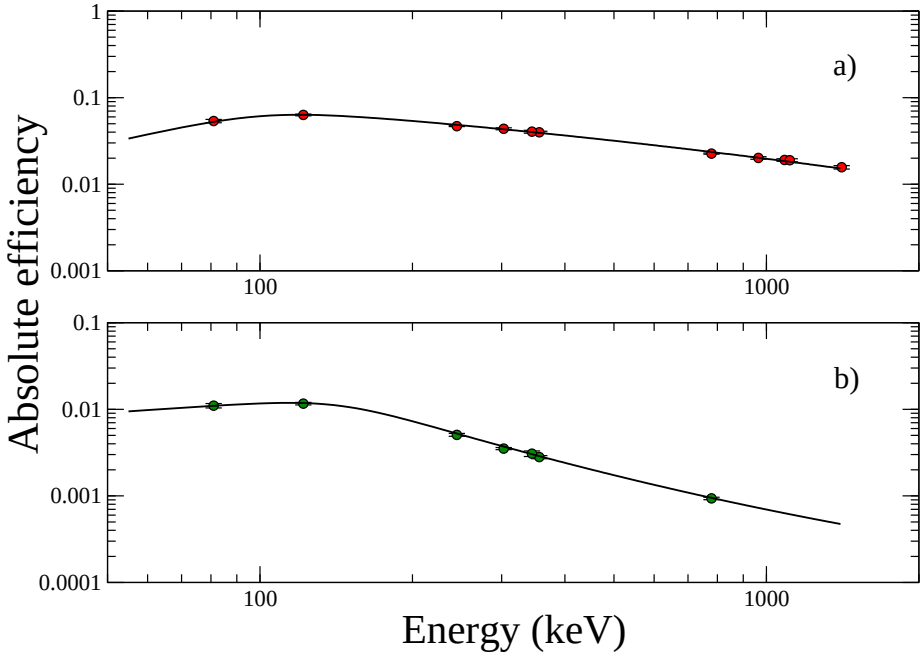

Figure 4.8: The absolute efficiency of a)the clover detector and, b) the Loax detector. The efficiency was calculated using the ^{133}Ba and ^{152}Eu source and including add-back.The lines show the result of the efficiency fitting performed with the RADWARE package, as it is explained in the text.

Efficiency curves were obtained from the ^{133}Ba and ^{152}Eu source. The position and size of the peaks were processed using the RADWARE package to obtain the absolute efficiency. The efficiency data was fitted to the following expression:

$$Eff = exp[((A + Bx + Cx^2)^{-G} + (D + Ex + Fx^2)^{-G}))^{-1/G}] \qquad (4.1)$$

where $x = ln(E_\gamma/100keV)$ and $y = ln(E_\gamma/1MeV)$. Fig. 4.8 shows the abso-

lute efficiency curves, for the clover and loax detectors. Both clover and loax efficiencies have a maximum around an energy of 100 keV.

The 3π beta-detector efficiency was provided by the IGISOL team, from the University of Jyväskylä, and is about $\simeq 70\%$ efficient.

4.3.2 Analysis procedure and results

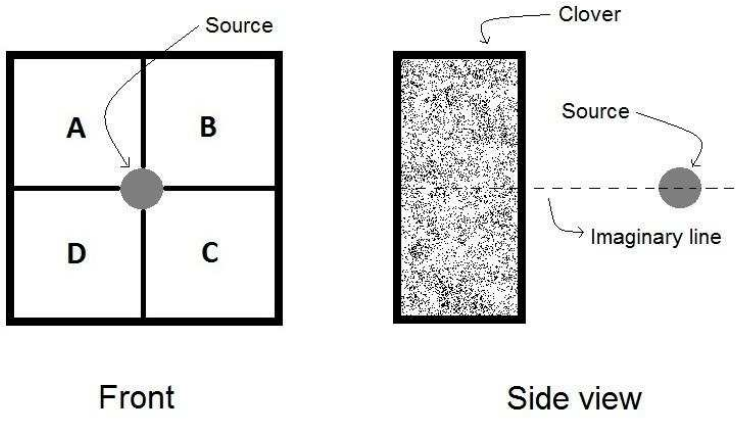

Figure 4.9: .
The relative position of the source with respect to the clover detector. The gamma-ray source is situated perpendicular to the front of the detector (represented on the right side of the figure). The distribution of germanium crystals within a clover detector is shown on the left side of the figure.

The trigger for the data acquisition was either a beta-gamma coincidence or a gamma-gamma coincidence event. Energies from beta and/or gamma decays were recorded in a event-by-event basis for further off-line analysis by two different simultaneous systems; an analog system, MIDAS (Multi Instance Data Acquisition System), and a digital one DAS (Digital Acquisition System).

Each germanium clover detector is composed of four germanium crystals (labelled A, B, C and D) as shown in fig. 4.9. The spatial distribution of the crystals within the clover detectors is shown in fig. 4.9 (left side) as well as the position of the source relative to the detector. Table 4.1 shows the number of single

(only one crystal fired), double (two crystals fired), triple (three crystals fired) and quadruple hits (four crystals fired) for each germanium detector obtained with the ^{133}Ba and ^{152}Eu source. Fig. 4.10 shows that horizontal (A+B, D+C) and vertical (A+D, B+C) events are more likely to occur than diagonal ones (A+C, D+C). This can be explained due to the bigger grater contact area in the first case, leading to the conclusion that double hits are essentially constituted by gamma-rays scattered between the crystals. Therefore add back has been performed. The energy of the photons belonging to these multiple hits has been added to obtain the original energy of the gamma ray emitted from the deposition point. The percentage of double hits is 6.6% for one of the clover detectors and 9.1% for the other, so the add back had a relevant effect in the improvement of the gamma spectra efficiency.

	Clover 1		Clover 2	
	Number of counts	%	Number of counts	%
Singles	6090440	92.7	6161092	90.1
Doubles	436588	6.6	623042	9.1
Triples	43092	0.6	50965	0.7
Quadruples	2163	0.03	2413	0.03

Table 4.1: Measured proportion of single, double, triple and quadruple hits in each germanium detector obtained with the ^{133}Ba and ^{152}Eu source.

During the experiment, two sets of data were measured; one at a trap frequency of 1075395 Hz and the other at 1075391 Hz, where ground and isomeric states of ^{100}Nb respectively are expected to be selected. Fig. 4.11 shows a segment of the measured spectra for trap frequencies of 1075391 Hz and 1075395 Hz. A key signature of the parent state nature is the ratio between the $4_1^+ \rightarrow 2_1^+$ (600.5(1) keV) and the $2_1^+ \rightarrow 0_1^+$ (535.7(1) keV) transition intensities in the daughter nucleus. This ratio is known to be 73(6)% from the isomer decay [74] and 1.2(1)% from the ground state [75]. The reason for this behaviour, is that the ($J^\pi = 4^+$) energy level, which decays via the 600.5 keV gamma ray, is strongly populated by the $J^\pi = 5^+$ ^{100}Nb isomer, but not by the $J^\pi = 1^+$ ^{100}Nb ground state. A similar case is the 461.1 keV gamma ray, whose level of origin is not fed by the

ground state at all. Another significant difference between the two spectra is the change in relative the intensities of the 535.7 keV $2_1^+ \rightarrow 0_1^+$, and 159.1 keV $0_1^+ \rightarrow 2_1^+$ transitions, also due to the different feeding patterns from the isomeric and ground states in ^{100}Nb.

In order to establish which parent state contributes to the creation of each of the measured spectra, measured gamma-ray intensities have been compared to the characteristic gamma rays of ^{100}Mo from ^{100}Nb ground-state [37] and isomeric state decay [76]. This is shown in table 4.2 where the first column lists energies of gamma-rays observed in this work and, the second and third columns show respectively, the measured intensities for each transition from previous studies [37] [76]. The two following columns lists the intensities of the gamma-rays obtained in this experiment, for the frequencies 1075391 Hz and 1075395 Hz normalized for the 535.7 keV transition. Finally, the last column list the calculated isomeric state intensities using the data presented in columns 4 and 5.

Branching ratios have also been calculated, for those cases in which it was possible, and compared to known values [37] [76]. The results are given in table 4.3. This table shows, in column order, from left to right, the energy level of origin of the gamma rays, the gamma-ray energy and the branching ratios calculated in

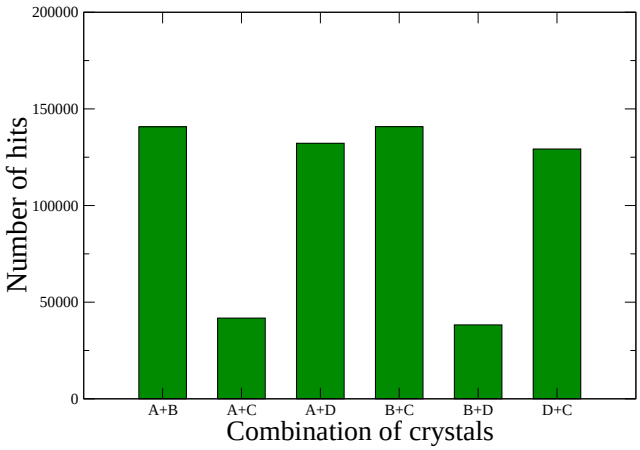

Figure 4.10: Double hits represented as a function of the crystals which have fired for one of the germanium detectors using the ^{133}Ba and ^{152}Eu source .

E_γ (keV)	Ground state I_γ(%) [37]	Isomeric state I_γ(%) [76]	1075395 Hz I_γ(%)	1075391 Hz I_γ(%)	Calculated Isomeric state I_γ(%)
159.5 (1)	19.3 (11)	3.8 (5)	29 (2)	14 (1)	0(3)
440.9 (1)	2.3 (1)		1.9 (2)		
461.1 (2)		8.2 (5)		4.2 (8)	8(2)
528.3 (2)	19.9 (4)	10 (1)	21 (2)	14 (1)	7 (3)
535.7 (1)	100.0 (2)	100	100 (8)	100 (5)	99 (16)
543.5 (1)	0.9 (1)	5.5 (8)		2.6 (5)	5.2 (9)
573.6 (2)	0.6 (1)		0.9 (1)		
600.5 (1)	1.2 (1)	73 (6)	0.8 (1)	37.4 (31)	74 (8)
622.5 (2)	3.3 (7)		3.7 (4)		
768.7 (1)	7.4 (7)	5.2 (5)	8.1 (6)	5 (1)	1 (2)
792.8 (2)		4.2 (6)		1.7 (4)	3.3 (7)
928.3 (1)	5.5 (2)	3.7 (4)	7.3 (6)	5.3 (6)	3 (1)
952.5 (3)		4.9 (6)		2.1 (4)	4.2(8)
967.0 (2)		17 (2)		11 (1)	22 (3)
969.1 (1)	5.7 (7)		5.6 (5)		
1022.5 (3)	10.7 (13)		12 (1)	4.0 (6)	-4.4 (16)*
1063.7 (1)	7.2 (4)	4.4 (9)	8.9 (7)	8 (1)	7(2)
1071.7 (2)	1.1 (2)	3.8 (7)	0.9 (1)	1.8 (3)	2.6 (7)
1246.4 (3)		2.7 (4)		2.9 (7)	6 (1)
1257.0 (6)	2.0 (2)		2.1 (3)		
1280.3 (2)		24 (3)		11 (1)	22 (3)
1441.5 (2)	0.6 (1)		1.2 (2)		
1501.9 (1)	9.6 (7)		13 (1)	6 (1)	-1 (2)*
1516.8 (3)		4.0 (6)		1.6 (4)	3.2 (9)
1550.5 (3)	1.5 (2)		2.3 (2)		
1567.4 (3)		6.0 (9)		3.3 (6)	7 (1)
1653.9 (2)	2.7 (2)		3.0 (4)		
2434.6 (5)	3.0 (2)		3.3 (5)		

* A negative intensity is clearly non physical and will be discussed in the text.

Table 4.2: Gamma-ray energies and intensities for transitions in ^{100}Mo. Columns 2 and 3 list the intensities previously measured following the beta decay of the ground [37] and isomeric [76] states in ^{100}Nb. Columns 4 and 5 list the intensities measured with Penning trap frequencies of 1075395 Hz and 1075391 Hz respectively. Column 6 lists the isomer state intensities calculated using the results of this experiment (columns 4 and 5).

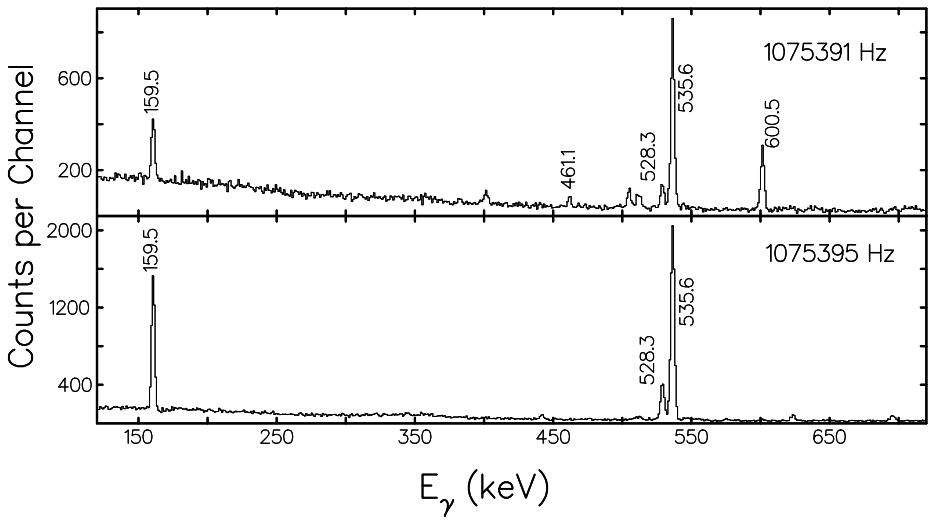

Figure 4.11: The beta-gated gamma-ray spectra measured at frequencies of 1075391 Hz (measured during 3 h and 12 min) and 1075395 Hz (measured during 10 h and 19 min). The upper plot, 1075391 Hz, contains 461.1 keV and 600.5 keV peaks which are missing in the lower plot. There is also a notable difference in the relative intensities of the 159.5 keV and 535.7 keV peaks in the two spectra.

the case of: the ground state [37], the isomeric state [76], the 1075395 Hz data file and the 1075391 Hz data file. All the branching ratios obtained in this experiment are in agreement, within two standard deviations, with those calculated from previous studies [37] [76], except in one case. As one can infer from table 4.3, the branching ratio for the 1607 keV level (543.5(1) and 1071.7(2) keV transitions) is not consistent between the two measurements [37] [76]. Although the measured branching ratio for the 1607 keV level agrees with Suhonen's measurement [76], it has been removed from further calculations.

The percentage of each parent state at each frequency can be calculated using the assumption that the measured intensity for each frequency must be a linear combination of ground and isomeric states. Expressing this idea through an equation:

$$I_i = a_i \cdot I_i^g + b_i \cdot I_i^i \tag{4.2}$$

where the subscript i labels each gamma-ray, I_i^g is the known intensity of the i^{th} gamma-ray from the ground state decay and I_i^i is the known intensity of the i^{th} gamma-ray from the isomer state decay. In addition, since a+b=1, it is possible to express the measured intensity of each measured gamma-ray as a function of one parameter a_i and, therefore, a weighted mean value of a can be calculated using the following equations:

Level (keV)	E_γ (keV)	Ground state [37]	Isomeric state [76]	1075395 Hz	1075391 Hz
1064	528.3 (2)	100 (2)	100 (12)	100 (5)	100 (8)
	1063.7 (1)	36 (2)	42 (10)	42 (4)	57 (10)
1464	768.7 (1)	100 (9)	100 (10)	100 (8)	100 (22)
	928.3 (1)	73 (7)	71 (10)	91 (10)	115 (29)
1505	969.1 (1)	100 (12)		100 (8)	
	440.9 (1)	41 (5)		34 (5)	
1607	543.5 (1)	100 (8)	100 (14)		100 (17)
	1071.7 (2)	117 (21)	69 (16)		69 (2)
2037	151.9 (1)	100 ()		100 ()	
	573.6 (2)	6 (1)		7 (1)	
2086	1022.5 (3)	100 ()		100 ()	
	1550.5 (3)	14 (2)		18 (3)	
	622.5 (2)	31 (7)		30 (4)	
2103	967.0 (2)		100 (11)		100 (11)
	1567.4 (3)		35 (6)		30 (6)
2416	1280.3 (2)		100 (11)		100 (11)
	952.5 (3)		21 (3)		19 (4)
2564	461.1 (2)		100 (6)		100 (19)
	792.8 (2)		51 (8)		40 (12)

Table 4.3: Branching ratios, in increasing order of level energy, observed in decay from the ground state [37], the isomer [76] and for the data collected at frequencies of 1075395 Hz and 1075391 Hz respectively.

$$\bar{a} = \frac{\sum w_i a_i}{\sum w_i}. \tag{4.3}$$

where the individual weights, w_i, are calculated from the errors, Δa_i, for each coefficient a_i:

$$w_i = \left(\frac{1}{\Delta a_i}\right)^2 \tag{4.4}$$

and the weighted error of $\bar{a}$ is given by:

$$\bar{\Delta a} = \frac{1}{\sqrt{\sum w_i^2}} \tag{4.5}$$

This calculation gives the following results: at a frequency of 1075395 Hz the ^{100}Nb ground state was successfully separated, with a purity of about 100%; at a frequency of 1075391 Hz, a mixture between the two states was measured with isomeric state proportion of about 50% ($\bar{a} = 0.50(2)$).

Using the value $\bar{a} = 0.50(2)$ the intensities of the gamma rays populated in the decay of the isomeric state of ^{100}Nb can be obtained. The results of such a calculation are listed in the sixth column of table 4.2 and should be compared with those in column three. 79% of the intensities listed in column six agree within one standard deviation with those in columns three and four, 95% agree within two standard deviations and 100% agree within three standard deviations. The last case (1022.5 keV) with a calculated intensity of $-4.4(16)$ constitutes a problematic interpretation from the physical point of view, since it is a negative intensity even within 2σ. Nonetheless, this could be interpreted from the point of view of the statistical nature of experimental data [77] which says that, for a normal distribution, the true value has $\simeq 68\%$ probability of being within one

standard deviation of the measured value, $\simeq 95\%$ of being within two standard deviations and $\simeq 99.7\%$ of being within three standard deviations. Therefore, the calculated intensities are consistent with those presented in the literature, although the high errors obtained for these calculated intensities highlight the need to improve the separation technique in order to increase its precision.

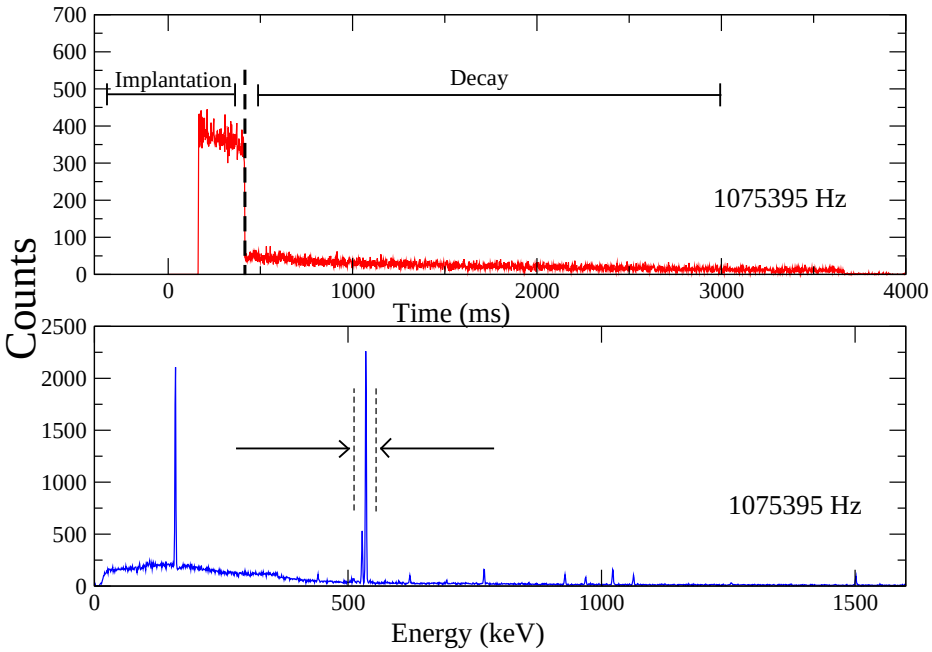

Figure 4.12: Above: The time of the gamma-ray emission relative to trap opening, for the 1075395 Hz data file, showing part of the implantation time as well as the decay time. Below: The gamma-ray spectrum corresponding to the above time spectrum. The dashed lines show how a gate can be set on one of the energy peaks to obtain the time spectra relevant to that peak.

Is also possible to measure the half-life of each state. As stated at the beginning of this section, ions were implanted during 3 s and allowed to decay for another 3 s at the 1075395 Hz frequency; the same procedure in cycles of 6 s implantation/ 6 s decay was used in the case of 1075391 Hz. The data collected using the Digital Acquisition System (DAS) was used for this analysis and sorted into time versus gamma-ray energy matrix. Figure 4.12 shows the projection of this matrix in

the case of a frequency of 1075395 Hz . The top spectrum shows the number of counts relative to the time and shows part of the implantation time as well as the decay time. The spectrum on the bottom of fig. 4.12 represents the recorded gamma-ray energies.

Setting a gate on a gamma-ray peak, as indicated by the dashed lines in the lower diagram of Figure 4.12, allows a background subtracted time spectrum for that peak to be obtained. This time spectrum can be used to calculate the half-life of the state selected at each frequency. Due to the small statistics the final data needed to be rebinned in order to minimize the spectra fluctuations, and was fitted to the exponential law of radioactive decay:

$$N(t) = N_o e^{-\lambda t}. \tag{4.6}$$

In the case of the data collected at 1075395 Hz, time spectra obtained by gating on the peaks: 159.5(1), 535.7(1) and 1022.5(3) keV have been added together. The final spectrum was rebinned by 100, 200 and 300 and fitted to de equation 4.6. The half-life obtained, by performing a weighted mean of the three sets, is $T_{1/2}^{1075395} = 1.40(2)$ s. This result is close to the expected 1.5(2) s [37] reported in previous studies and is consistent with the hypothesis of 100% ^{100}Nb ground state data.

The 1075391.4 Hz time spectrum was made by adding the individual time spectra obtained by gating on the peaks: 535.7(1), 600.5(1) and 1022.5 (3) keV rebinned by 300, 500 and 700. In this case, the analysis of the intensities, discussed above, indicates that the decay should comprise 50%-50% of the ground and isomeric states. So it is logical to expect the half-life fit to have two components. The radioactive decay law for this particular case is:

$$N(t) = N_1 e^{-\lambda_1 t} + N_2 e^{-\lambda_2 t} \tag{4.7}$$

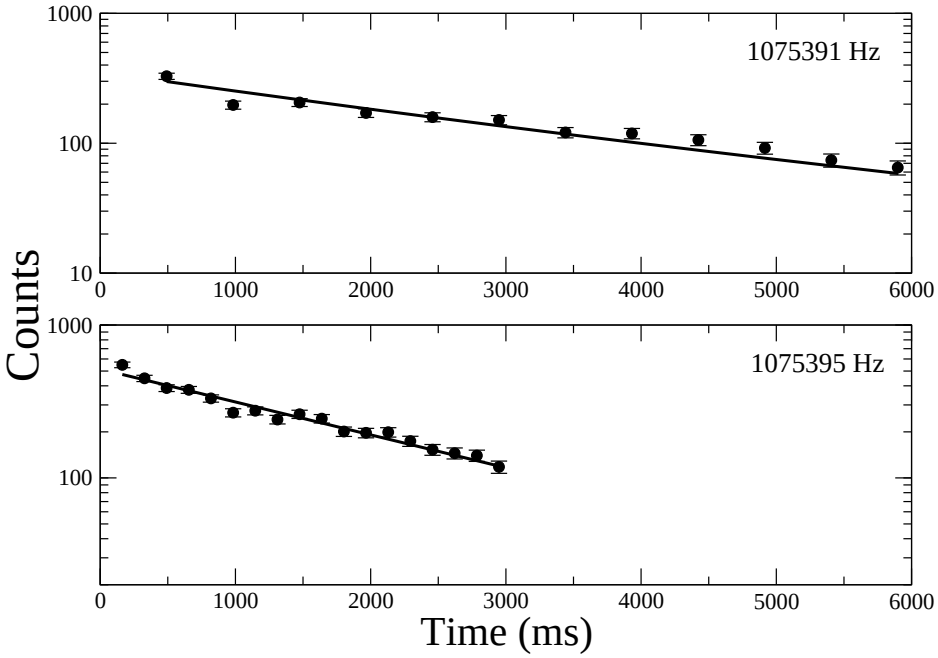

Figure 4.13: Below: the time profile of 159.5(1), 535.7(1) and 1022.5(3) keV gamma rays measured at a frequency of 1075395 Hz . Above: the time profile of 535.7(1), 600.5(1) and 1022.5 (3) keV gamma rays measured at a frequency of 1075391.4 Hz. The solid line shows the results of a constrained fit to the exponential decay law, performed assuming equal initial populations of both states of ^{100}Nb and known half-lives (1.5(2) s [37] and 3.0(1)s [75]).

where the subscripts 1 and 2 refer to the ground and isomeric states of ^{100}Nb. However, the low statistics in this case made it impossible to separate the two components, and the best possible fit calculated one exponential function with a resulting half-life dominated by the isomeric state ($T_{1/2}^{1075391} = 2.7(1)$, χ^2=2.76). Constraining the fit, such that the value of the decay constants relates to half-lives of 1.5 and 3.0 s and that the initial populations of both parent states are equal, gives a reduced χ^2=3.02. Fig 4.13 shows the fit of the to the radioactive decay law. The lower graph shows the fit for the spectra collected at 1075395 Hz. The upper picture represents the constrained fitting for the 1075391 Hz case, showing that the data is consistent with the results obtained in the calculation

of the percentages of the parent state population previously explained.

Chapter 5

IGISOL IV

The upgrade from IGISOL III to IGISOL IV started with the acquisition of the MCC30 light ion cyclotron. The previous facility was moved to a new building adjacent to the existing one, which was constructed in order to house the new accelerator and IGISOL IV. As a consequence, a new layout was designed to adapt the IGISOL to the new experimental hall and to include several improvements which will be discussed in this section.

The MCC30 light ion cyclotron provides proton (30 MeV, 100 μA) and deuteron (15 MeV, 50 μA) beams and is capable of producing two beam simultaneously [78]. In addition it will be used only by the IGISOL facility and ^{18}F production to make a compound called FDG, used for PET. The IGISOL will also have access to the K130 heavy ion cyclotron but, since IGISOL is mainly using light ion induced fission reactions, the annual beam time of the facility is expected to be increased up to 4000 hours [79]; and longer experimental runs will also be possible. The use of neutron converter targets (currently being designed) will enable the creation of primary neutron beams for neutron induced fission reactions. The combination of proton, deuteron and neutron beams with several actinide targets and optimized gas cells will expand the limits of the production of neutron-rich nuclei beyond the limits of IGISOL III.

Since no significant modifications have been made to the IGISOL front-end, the

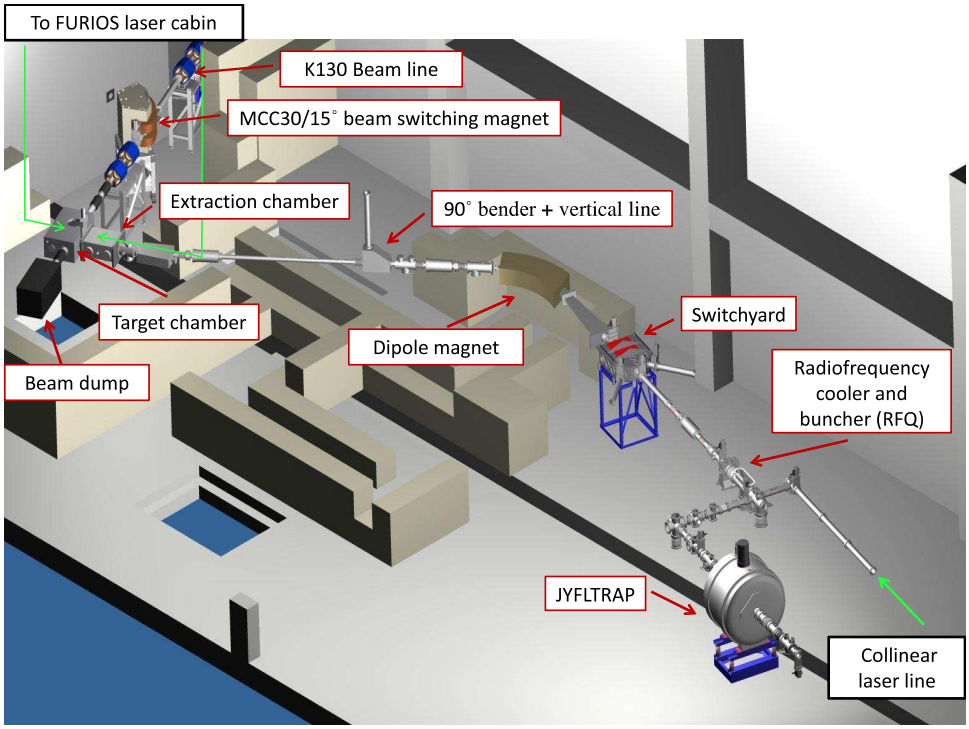

Figure 5.1: A 3D sketch of the new hall where the main components of IGISOL IV have been labelled. The green arrows indicate the access of the pulsed lasers to the target chamber from the FURIOS cabin and of the collinear laser to the RFQ from the collinear laser hut [68].

upgrade of the layout does not affect the efficiency of the IGISOL technique. Fig. 5.1 represents a 3D sketch of the new experimental area. Beam lines of access from both accelerators are shown inside the IGISOL cave. A beam switching magnet provides access to the primary beam from the MCC30 cyclotron, which is situated behind the cave back wall. The two green arrows, from the FURIOS laser cabin (situated above the cave) to the target cave, show the laser paths for the LIS (laser ion source)and LIST (laser ion source trap) methods [80]. The access of the laser light to the IGISOL front-end has been considerably improved by the new outline. In the new design a 15° bender, situated after the extraction chamber, gives direct access of the laser light to the SPIG [64]. This set-up allows high selectivity RIB (radioactive ion beam) production through a novel technique

in which laser ionization is performed within the expanding gas jet immediately following the gas cell [81].

Following the beam line beyond the target chamber the next important change is the existence of a vertical line as shown in fig. 5.1. A 90° degree bender can be used to get off-line beam into the main beam line from an off-line source situated upstairs. A series of off-line sources (e.g. discharge source, alpha-decay recoil source, carbon cluster source) are commonly used to tune the beam line and for mass measurement calibrations [82], as will be explained in section 5.1. The IGISOL beam line often needs to be tested between experiments so the vertical line provides a way to avoid the high radiation levels in the cave. After the 90° degree bender the line continues into the switchyard, through the mass selecting dipole magnet. The new switchyard has been designed in order to switch between three different lines: the main beam line, a permanent monitoring station and, a third line for spectroscopy experiments [79]. Fig. 5.1 shows how the main beam line continues to the Radiofrequency cooler and buncher (RFQ) [65] and, from there to the JYFLTRAP [66]. Given that the RFQ is exactly the same as before, a similar performance is expected. The JYFLTRAP is also the same one but, as a consequence of the increased space after the trap, bigger and more complex detector setups can be built to perform trap-assisted measurements. The beam transfer line from the RFQ to the collinear laser spectroscopy hut is indicated by an arrow in fig. 5.1. In the new configuration, this line is shorter and, the visibility to the optical axis of the RFQ improves the optical manipulation of the ionic ensemble, used to populate metastable states which are subsequently used in the collinear experiments [83]. Furthermore, the trap and the RFQ are electrically isolated from each other, which permits the independent operation of both devices affording more flexibility on operation.

Despite all these changes, there is no expected significant improvement in the upgrade of the IGISOL facility regarding the ^{102}Zr measurements. The principal elements of the old IGISOL (SPIG, cooler-buncher, Penning trap) are the same, with most of the changes being a matter of layout, and the main improvements (vertical line for offline sources, optimization of the pulsed laser line, radiation safety, etc) not affecting the isomeric cleaning. On the other hand, from laser

measurements, an improvement by a factor of 5/3 in the fission yield have been observed. This might be due to better extraction optics in the front end (IGISOL IV has two extractor electrodes where, in the past, there was only one, and the apertures of the electrodes have been opened up so it may have less losses in transmission to the mass separator).

5.1 First beamline tests at IGISOL IV

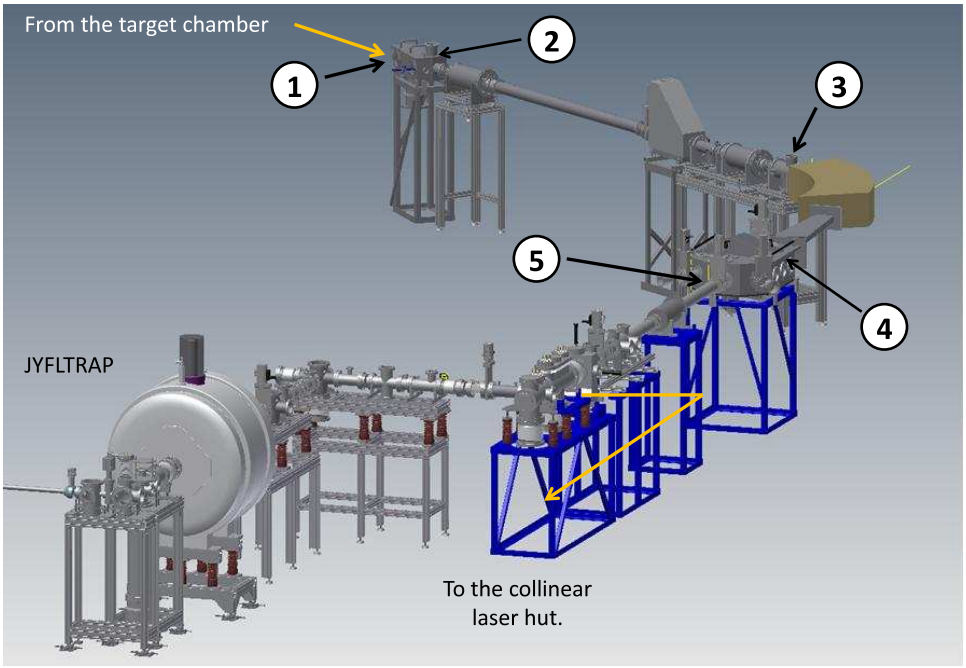

Figure 5.2: The placement of the Faraday cups, fluorescence panels and silicon detectors used in the first test of the IGISOL IV beam line. Faraday cups are placed at positions 1 to 5. Fluorescence panels were also situated in spots 2 to 5. Finally, 3 silicon detectors were used at 2, 3 and 5.

The first tests of IGISOL IV were performed in February 2012 and measured the performance of the facility from the target chamber to the switchyard. At that moment, the vacuum level in the beam line was 10^{-5} mbar and the gas lines

were not completed. Therefore, the tests were performed by injecting the buffer gas into the ion guide directly from a gas bottle.

Originally, a spark source placed at the ion guide site was used to create an ionic beam. A spark source is a method used to produce ions from a solid sample. The prepared solid sample is vaporized and partially ionized by an intermittent discharge or spark. In this particular case, within the gas cell, an electrical pulse (spark) between two copper electrodes is used to vaporize and ionize surface atoms. These ions are stopped in the gas cell which contains the electrodes and are then extracted by the gas flow and are guided through the radio frequency sextupole into the beam line of the mass separator (see section 4.1.1). The produced current was used to tune the beam settings and give an initial estimation of the performance of the beamline. Fig. 5.2 shows the positions along the beam line in which a series of fluorescence panels and Faraday Cups were placed in order to measure the current and shape of the stable ion beam. This set up allowed the tuning of the focusing and directional elements of the facility in different stages, facilitating the optimization of its current and intensity. The results were similar to the ones obtained for IGISOL III. About 400 nA were measured after the SPIG (position labelled as 1 in fig. 5.2) and 100 nA in the beam line about 32 cm after the switchyard (5 in fig. 5.2). It is convenient to remark that these numbers should not be taken as an estimation of the transmission efficiency since the Faraday Cups used have different sizes.

Following the discharge source test, an alpha recoil source was used to study the efficiency of the IGISOL, which is the main performance criterion of the facility. In order to detect the ions, the Faraday cups were replaced by silicon detectors in the locations tagged as 2,3 and 5 in fig. 5.2.

The ^{223}Ra α-decay recoil source used for these measurements was made using a ^{227}Ac source by the method described in [84]. The efficiency was recorded by measuring the alpha-particles emitted by the first daughter in the decay chain, ^{219}Rn, using a silicon detector. Fig. 5.3 shows the ^{227}Ac decay chain, where the nuclei of interest are highlighted.

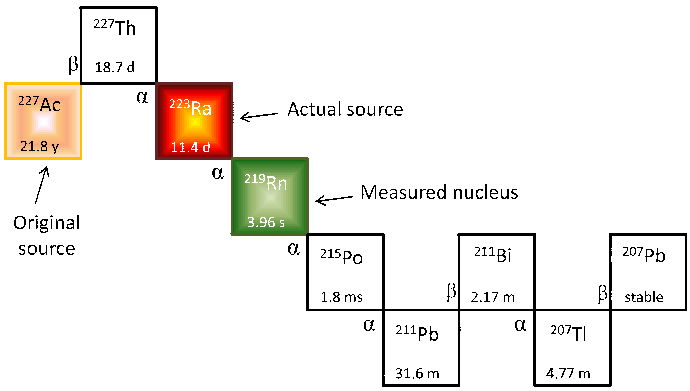

Figure 5.3: The ^{227}Ac decay chain.

For the purpose of measuring the efficiency of the beam line, the ^{223}Ra alpha-decay needle tip source was placed in an ion guide installed within the target chamber in a transverse position with respect to the extraction axis of the ion guide. A silicon detector used to measure the recoils from the α source, was located after the switchyard (position 5 in fig. 5.2). The signal from the detector was amplified and manipulated by a computer program so that the rate of α-particles from ^{219}Rn with energy 6819.1(3) keV were the only ones used to perform the efficiency measurements. Fig. 5.4 shows the relative transmission efficiency as function of the He pressure with different voltage settings for the SPIG and different distances between the repeller and the ion guide exit hole. All the tuning elements along the beam line were also used in order to maximize the measured yield. The behaviour of the efficiency, shown in fig. 5.4, can be explained by the change of the gas flow field caused by the transverse position of the alpha source with respect to the beam line [84]. The best efficiency is obtained in case b), at a He pressure of 38 mbar, distance between the repeller and the exit hole of the ion guide is 12(1) mm and the SPIG voltages are optimized for such a distance. Fig. 5.5 was taken from [84], and shows the first results obtained for a previous SPIG in comparison with ones for the skimmer at IGISOL II. Is possible to see that the results in the case of a broken axial symmetry shown in fig. 5.5 a) are in good agreement with the ones presented in fig. 5.4; while in the case of full axial

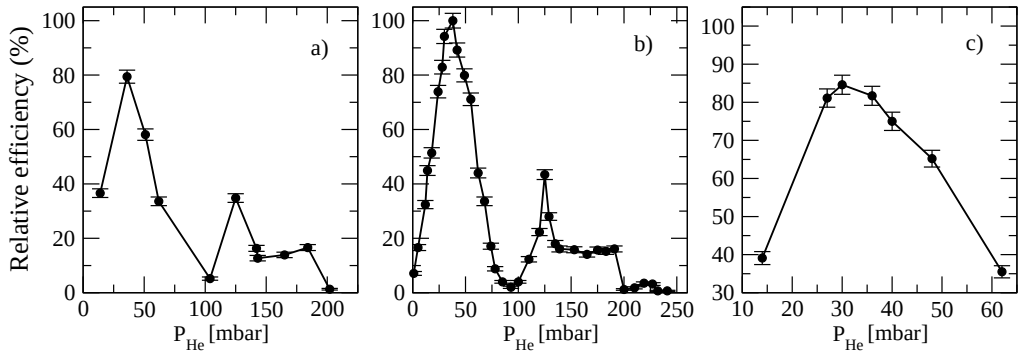

Figure 5.4: The relative efficiency, measured using the alpha recoil source, as a function of He pressure. The three graphs show the response obtained with the transverse α recoil source a)Initial SPIG voltage settings [64]. Distance between the repeller and the exit hole of the ion guide d=12(1) mm; b)Optimized voltage settings, d=12(1) mm; c) Same voltages as in b), d=5(1) mm.

symmetry, fig. 5.5 b), there is a smoother pattern, with no secondary maxima. The measurements reported in [84] were obtained for a different chamber with different volume, shape, distances and voltages. Therefore, the change in the position of the maxima and the relative efficiency, as well as the different pressure range are not unexpected. No simulations have been done to study the influence of a source placed in a transverse position over the gas flow inside the ion guide, but comparing the results in fig. 5.4 and in fig. 5.5 a) it is clear that they show a similar pattern. In both cases, the efficiency curve shows an absolute maximum, a deep minimum and a secondary maximum.

The results of the alpha-source experiments gave an overall efficiency of 1% measured at the silicon detector placed at position 5 in fig. 5.2, and a transport efficiency of about 50% from the ion guide to the silicon detector situated after the switchyard.

Finally, the light ion guide was tested on line using the reactions ^{58}Ni(p,n)^{58}Cu and ^{54}Fe(p,n)^{54}Co. The measurements of the Cu atoms were performed with the same silicon detectors. He and Ar gases were separately employed in an attempt to increase the efficiency. The transport efficiency of the system using He as the buffer gas was similar to that obtained in the case of the alpha recoil source (50%

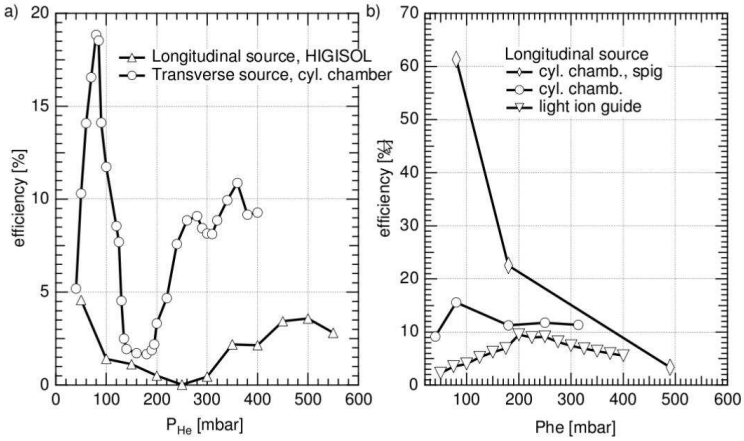

Figure 5.5: Taken from [84]. The efficiency, measured with the alpha recoil source as a function of He pressure, for different ion guide set-ups at IGISOL II. a) Axial symmetry broken; b) Full axial symmetry. The acronym HIGISOL means heavy-ion ion guide isotope separator on-line and is different from the light ion guide used for the 2012 tests.

transmission efficiency). No significant differences were perceived by replacing the He with Ar.

5.2 Further experiments:

Between February and August 2012 several improvements were performed at the facility, such as the construction of the gas feeding lines, new alignments, the addition of new beam-line tuning elements, etc. The first experiment at IGISOL IV was scheduled for the last week of August 2012. As a consequence a series of new tests and fine tuning were carried out to the IGISOL IV front end. Fig. 5.6 shows a schematic view of the beam line used in these experiments, from the target chamber to the switchyard, and the spectroscopy set up consisting of one 4π scintillator and two germanium detectors at the deposition point. Fig. 5.6 show the set up used in all the test mentioned in this section so, in the following, all the descriptions of the set up will refer to different devices shown in this figure.

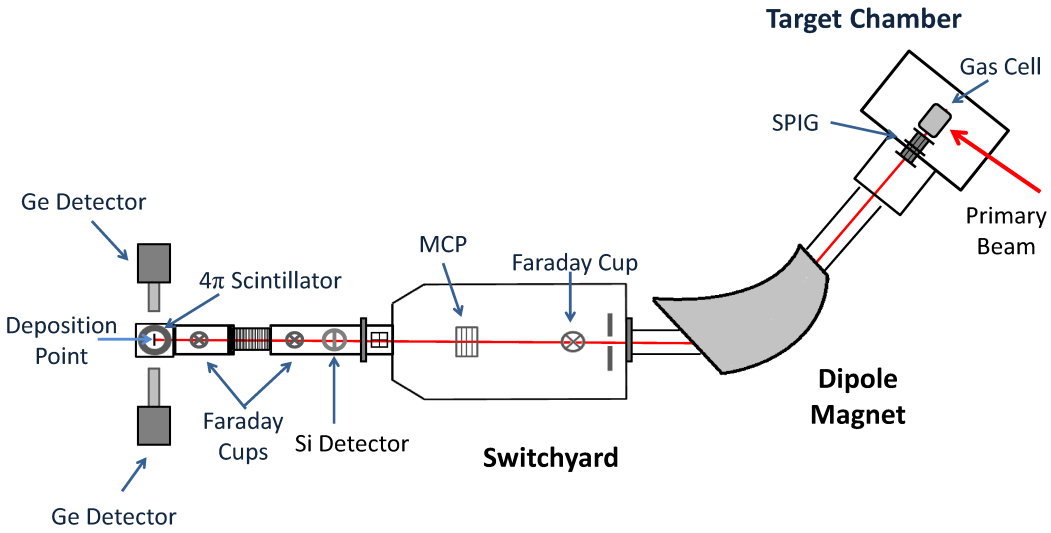

Figure 5.6: A schematic view of the IGISOL IV beam line used in the test run during August 2012.The beam produced in the target chamber (ion guide) is transported through the SPIG to the mass separator and directed to the dipole magnet. In the magnet a single mass is selected and injected into the switchyard through a slit. Several detection devices are placed between the slit and the deposition point, allowing different kind of measurements depending on the test realized.

The first study consisted of the testing of the dipole magnet and its mass calibration. For that purpose the discharge source was placed in the target chamber, inside the ion guide. Also, a small amount of Xe gas was introduced into the ion guide along with helium. A mixture of stable isotopes of Xe gas, with masses between 124 and 136 u, was used. The mass separation of the accelerated nuclei is done using an electrical dipole magnet that splits the trajectory of the ions according to their mass to charge ratio.

The mass resolution of the magnet, is its ability to distinguish between close masses and, is defined as the ratio between the full width at half maximum (FWHM) and the centroid of the peak. The smaller the figure for the resolution the better the magnet will be able to distinguish between two nuclei with adja-

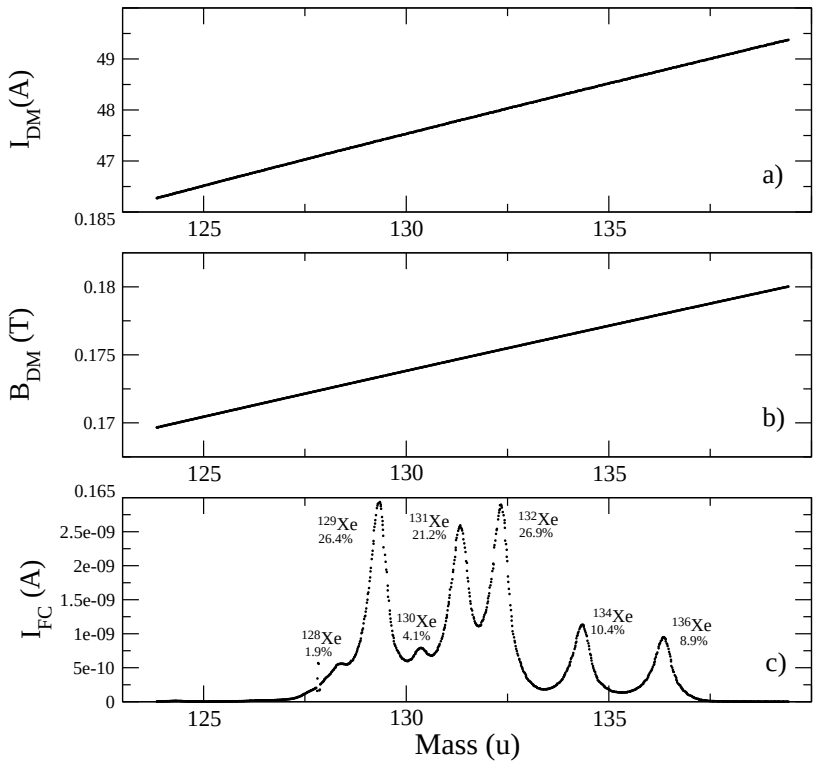

Figure 5.7: The resolution of a Xe mass scan with a 3.1 mm slit: a) the current of the dipole magnet; b) the magnetic field of the dipole magnet; and c), the measured current at the switchyard Faraday cup (see fig. 5.6), as a function of the atomic mass. Xenon isotopic abundances are labelled accordingly.

cent masses. Different m/q ratios correspond to different curvature radii in the magnetic field, so that a beam of desired m/q ratio is selected by a slit located at the entrance of the switchyard, as can be seen in fig. 5.6. By varying the magnetic field inside the magnet it is possible to perform a mass scan in order to see the different masses produced at the ion guide. Fig. 5.7 shows a mass scan performed for the Xe isotopes using a 3.1 mm slit. In the bottom graph, c), the y axis shows the current collected at the Faraday cup situated inside the switchyard (see fig. 5.6) in A per 1.341 s, while the x axis shows the approximate mass unit. The size of each peak is proportional to the particular Xe isotope abundance and, the resolution is clearly not enough to separate adjacent masses. Fig. 5.7 a) and b) show, respectively, the current of the dipole magnet and the magnetic field

of the dipole magnet as a function of the mass. Both relations are linear and, assuming that the straight line "magnetic field versus mass" goes though zero, one can do a calibration with a single known mass. This figure can be compared with fig. 4.7 which shows the much higher resolution of the double Penning Trap. The mass scan for molybdenum performed with JYFLTRAP presents a clear separation between masses with one unit of difference, while fig. 5.7 shows a clear overlapping between those.

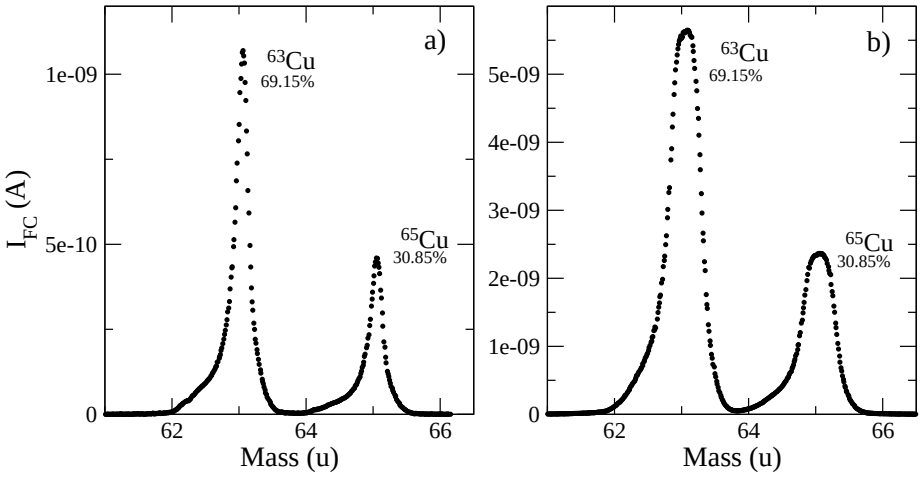

Figure 5.8: A Cu mass scan for two different slit widths: a) 1.2 mm; b)10.4 mm

Similar to optical spectroscopy, low resolution is achieved using wide slits while high resolution is attained employing narrow slits. This behaviour is illustrated in fig. 5.8 which shows two mass scans corresponding to two different slit widths for ^{63,65}Cu. Fig. 5.8 a) shows a mass scan for a slit width of 1.2 mm and, presenting a characteristic triangular peak with a low mass tale while, fig. 5.8 b) used a width of 10.4 mm and illustrates a lower resolution with a flatter top peak.

The mass resolution of the dipole magnet for different slit widths is shown in Fig. 5.9 a) calculated for the cases of ^{134}Xe and ^{136}Xe. For both masses, it is

possible to see how the resolution increases as the width decreases. However, it should be emphasized that as the resolution increases the transmission decreases, as can be seen in fig. 5.9 b); where the transmission is taken as the number of counts in 1.341s at the central mass for each peak. So in order to get a reasonable number of ions for a particular experiment it is necessary to find a compromise between these two limitations.

Finally, in order to compare these results with the performance of IGISOL III, it is convenient to define the mass resolving power: $MRP = M/\Delta M$. For IGISOL III, it has been established that the MRP was 300 between the dipole magnet and the SPIG for a slit width of 7 mm [85]. In the present case, the MRP varies from a value close to 300, for a slit width of 1.2 mm, to less than 200 for a slit width of 5.6 mm. Considering these results, it is natural to conclude that the MRP after the dipole magnet could still be improved by manipulating the beam. As the MRP depends on the quality of the beam, i. e. of the beam emittance, further adjustments in the beam tuning implemented with the SPIG and the different focusing elements, or any changes affecting the beam (like alignment modifications), could result in a better resolution.

5.2.1 The light ion guide

Once the dipole magnet was ready, the discharge source was replaced by the light ion guide. A primary beam of 18 MeV protons impinged onto a ^{58}Ni target (thickness 1.8 mg/cm^2) to produce ^{58}Cu via the ^{58}Ni(p,n) reaction. For a pressure of 128 mbar, the maximum count rate was found for a magnetic field of 1160 G. Fig. 5.10 shows a pressure test conducted with the light ion guide with the magnetic field of the dipole magnet fixed at this value. The number of ions detected by the silicon detectors after the switchyard during a period of time of 30 s is plotted against the pressure inside the light ion guide. The plot shows a region of saturation between 150 and 200 mbar, thus this region appears to be suitable for optimal running.

The pressure was then set at 200 mbar, the magnetic field at the dipole mag-

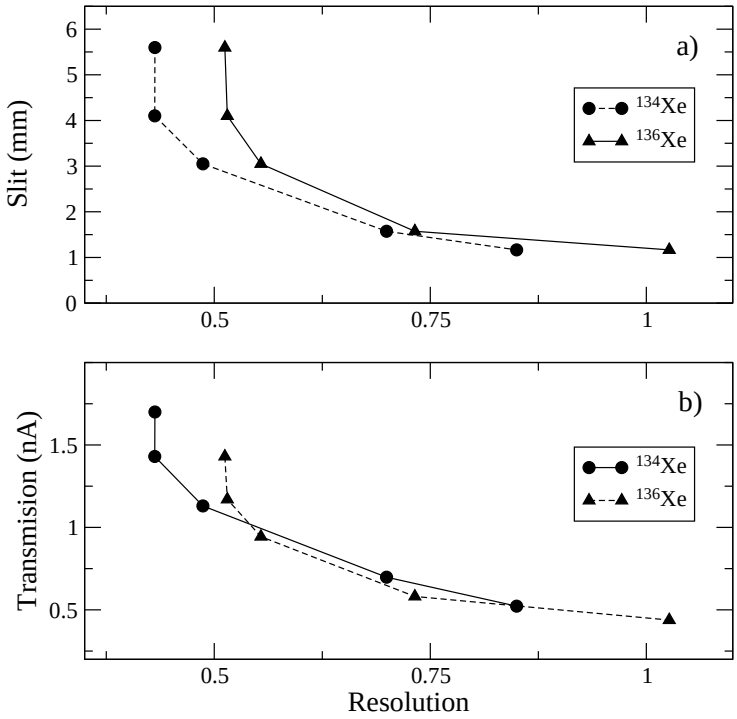

Figure 5.9: The resolution and transmission of the dipole magnet in the case of ^{134}Xe and ^{136}Xe: a) Slit width VS resolution; b) Transmission VS resolution.

net was chosen to select mass 58 (1160.82 G) and all the beam line elements were tuned to maximize the current of the small Faraday cup located before the spectroscopy set up (see fig. 5.6). In IGISOL III, indirect measurements of ^{58}Cu performed with a similar set-up, a primary current of 1μA resulted in a measured yield of 6850 ions/s. In the present case measurements were taken using a primary beam of 500 pA. Ions were implanted in an aluminium foil in front of the silicon detector, resulting in a rate of 17500 ions/30s. Given that the efficiency of such a detector using the foil is 33%, the actual rate per second is 1750 ions, which extrapolates to about 3500 ions/s for a primary beam of 1 μA. This is two times lower than in the case of IGISOL III, which is a reasonable result at this stage. Finally, the γ-ray spectrum of the ^{58}Cu was measured with the spectroscopy set up. The results are shown in fig. 5.11 where the key ^{58}Cu gamma-rays, 1321.2, 1448.2 and 1454.45 keV are clearly visible, proving that the

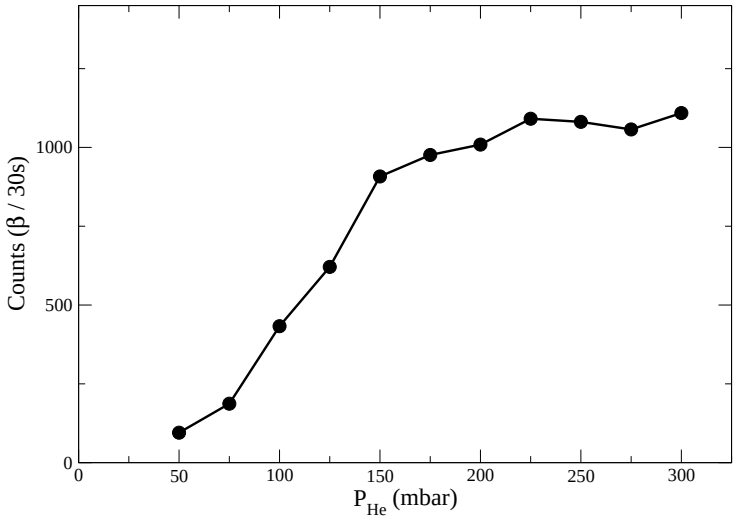

Figure 5.10: The number of ^{58}Cu ions observed in 30 s in function of the pressure inside the ion guide.

IGISOL IV is able to provide mass selected radioactive ion beams.

Work on the IGISOL facility has continued since the test experiments described in this section. Currently the trap line is finished and transmission efficiencies have been measured all the way through the line [86]. Also, some test have been performed using the JYFLTRAP proving that both traps are working. Nonetheless, all results are preliminary. The transmission through the trap beam line is to be refined, the transport between both traps needs to be improved, a characterization of the JYFLTRAP settings is needed, etc.

The off-line preparation of the collinear laser spectroscopy set-up has been completed. On-line beams produced via proton-induced fission have been delivered to the collinear laser line with similar spectroscopy efficiencies to the ones obtained for IGISOL III [87]. Also some advances in the status of the FURIOS laser system have been accomplished and are reported in [88].

In addition to the ongoing work in the construction and refinement of the IGISOL IV facility, the first beam time proposals have already been performed at the

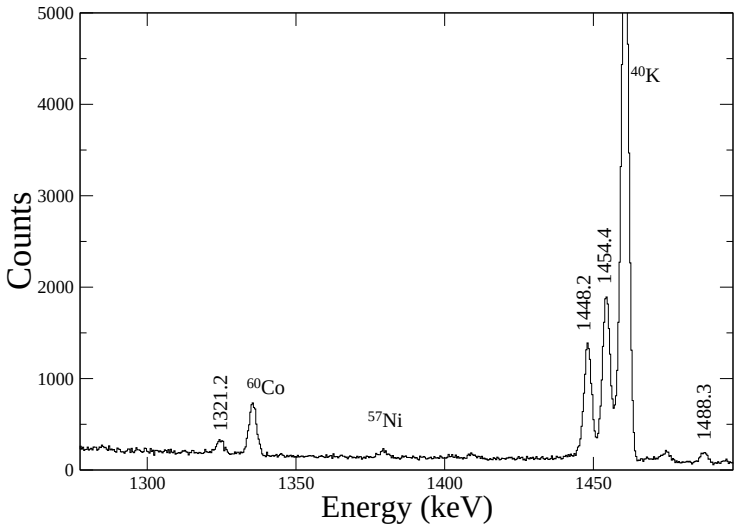

Figure 5.11: The ^{58}Cu gamma-ray spectrum.

laboratory. These were all rather simple implantation experiments which did not need the trap which is currently being prepared for first experiments [86].

Chapter 6

Conclusions

The information presented in this thesis shows the importance of study the structure of neutron-rich zirconium isotopes. Strong deformation, predicted shape coexistence and isomerism are key phenomena in the study of nuclear physics. The calculations performed within the IBM-1 model, have provided a set of four-term Hamiltonians, all of them including a term proportional to the quadrupole moment, responsible for deformation. This is consistent with the known rotational behaviour of the ground state bands of zirconium nuclei. Despite the present results being too broad to provide a real understanding of the structure in this region, there are four possible Hamiltonians which are consistent with the systematics shown in Chapter 1. The zirconium nuclei have greater deformation than the rest of the ones used in these calculations, so the procedure employed in this thesis might not be the most appropriate. It would be interesting to repeat the calculations for the isotopic chain when a increased amount of experimental data becomes available; Especially data regarding the transition probabilities which are currently almost completely unknown in the case of zirconium. It would also be interesting to compare the calculations for ^{108}Zr with new data, given that the experimental level scheme used is only tentatively known.

The online post-trap spectroscopy method developed at IGISOL III and explained in chapter 4, will provide the opportunity to measure new low-lying states in ^{102,104,106}Zr, study the separated decay of the ^{102}Zr isomeric state and, in general,

find new information about these nuclei which will help us to understand their structure and behaviour. A paper on this method has been published [18] and it is the hope of the author, that it will prove a useful technique, not only in the study of zirconium, but for general research of nuclear isomerism. It also might be that, in the future, the new IGISOL IV facility will be able to produce even more neutron-rich zirconium nuclei and, with it, develop a further understanding of deformed atomic nuclei.

Appendix A

	Isobars (A=102)				
Transition	H_2	H_3	H_7	H_9	H_{19}
B[E2; 2(1)–> 0(1)]	0.2347	0.3464	0.3320	0.4119	0.4585
B[E2; 4(1)–> 2(1)]	0.3385	0.5144	0.5022	0.5940	0.6431
B[E2; 6(1)–> 4(1)]	0.3588	0.5672	0.5635	0.6453	0.6819
B[E2; 2(2)–> 0(2)]	0.0703	0.1318	0.0517	0.0312	0.0794
B[E2; 4(2)–> 2(2)]	0.1372	0.1517	0.1842	0.2091	0.2544
B[E2; 6(2)–> 4(2)]	0.2412	0.3276	0.3467	0.3876	0.4245
B[E2; 0(3)–> 2(3)]	0.0451	0.0915	0.1025	0.1082	0.0579
B[E2; 4(3)–> 2(3)]	0.1789	0.2136	0.3197	0.3761	0.3872
B[E2; 6(3)–> 4(3)]	0.2304	0.3459	0.3614	0.3899	0.4368
B[E2; 2(2)–> 0(1)]	0.0349	0.0095	0.0182	0.0146	0.0095
B[E2; 0(2)–> 2(1)]	0.0486	0.1034	0.1109	0.0522	0.0047
B[E2; 4(2)–> 2(1)]	0.0210	0.0130	0.0107	0.0085	0.0045
B[E2; 6(2)–> 4(1)]	0.0156	0.0140	0.0106	0.0084	0.0030
B[E2; 2(3)–> 0(2)]	0.1021	0.0962	0.2020	0.2501	0.2389
B[E2; 0(3)–> 2(2)]	0.0446	0.0974	0.0089	0.0088	0.0054
B[E2; 4(3)–> 2(2)]	0.0481	0.1150	0.0118	0.0043	0.0179
B[E2; 6(3)–> 4(2)]	0.0120	0.0149	0.0087	0.0052	0.0049
B[E2; 2(3)–> 0(1)]	0.0059	0.0087	0.0015	0.0005	0.00001
B[E2; 0(3)–> 2(1)]	0.0012	0.0014	0.0013	0.0039	0.0089
B[E2; 4(3)–> 2(1)]	0.0002	0.00002	0.0001	0.00005	0.0025
B[E2; 6(3)–> 4(1)]	0.0011	0.0006	0.00003	0.0007	0.0055
B[E2; 4(2)–> 2(3)]	0.0038	0.0265	0.0055	0.0055	0.0029
B[E2; 6(2)–> 4(3)]	0.0003	0.0011	0.0006	0.0012	0.0010

Table 1: Experimental and theoretical B(E2) values (in units of e^2b^2) for transitions in ^{102}Zr. The table shows the results calculated by fitting the parameters of the Hamiltonians using the experimental data available in the isobaric chain. A value of $e_b = 0.11$ eb is used in all the cases.

Transition	Isotones (N=62)				
	H_2	H_3	H_7	H_9	H_{19}
B[E2; 2(1)–> 0(1)]	0.2536	0.3727	0.3777	0.4529	0.4387
B[E2; 4(1)–> 2(1)]	0.3567	0.5389	0.5432	0.6354	0.6108
B[E2; 6(1)–> 4(1)]	0.3777	0.5896	0.5915	0.6738	0.6421
B[E2; 0(2)–> 2(2)]	0.1914	0.1653		0.0441	0.0382
B[E2; 2(2)–> 0(2)]			0.0263		
B[E2; 4(2)–> 2(2)]	0.1498	0.1882	0.1855	0.1996	0.1951
B[E2; 6(2)–> 4(2)]	0.2701	0.3588	0.3540	0.3669	0.3608
B[E2; 0(3)–> 2(3)]	0.0172	0.0529	0.0850	0.0161	0.00002
B[E2; 4(3)–> 2(3)]	0.2651	0.3528	0.3524	0.2568	0.4183
B[E2; 6(3)–> 4(3)]	0.2775	0.3747	0.3777	0.1394	0.4256
B[E2; 2(2)–> 0(1)]	0.0438	0.0175	0.0166	0.0094	0.0045
B[E2; 0(2)–> 2(1)]	0.0076	0.0337	0.0390	0.0025	0.0069
B[E2; 4(2)–> 2(1)]	0.0204	0.0098	0.0109	0.0063	0.0020
B[E2; 6(2)–> 4(1)]	0.0142	0.0096	0.0108	0.0068	0.0013
B[E2; 2(3)–> 0(2)]	0.1905	0.2441	0.2357	0.2203	0.3072
B[E2; 0(3)–> 2(2)]	0.0061	0.0009	0.0052	0.0005	0.0095
B[E2; 4(3)–> 2(2)]	0.0049	0.0040	0.0027	0.0018	0.0001
B[E2; 6(3)–> 4(2)]	0.0056	0.0053	0.0045	0.0002	0.0007
B[E2; 2(3)–> 0(1)]	0.0001	0.0005	0.0010	0.00008	0.0032
B[E2; 0(3)–> 2(1)]	0.0003	0.0008	0.0010	0.0061	0.0017
B[E2; 4(3)–> 2(1)]	0.00002	0.00002	0.0001	0.0014	0.0069
B[E2; 6(3)–> 4(1)]	0.0001	0.00008	0.00004	0.0015	0.0097
B[E2; 4(2)–> 2(3)]	0.0181	0.0099	0.0069	0.0012	0.0065
B[E2; 6(2)–> 4(3)]	0.0145	0.0032	0.0025	0.0050	0.0041

Table 2: Experimental and theoretical B(E2) values (in units of e^2b^2) for transitions in ^{102}Zr. The table shows the values obtained using the known data in the isotonic chain. A value of $e_b = 0.11$ eb is used in all the cases.

Transition	^{110}Pd	^{108}Ru	^{106}Mo	^{104}Zr	^{104}Mo	^{104}Ru
$2_1^+ \rightarrow 0_1^+$	0.1769(28)	0.1891(157)	0.3059(10)	0.5301(796)	0.2231(184)	0.1713(30)
$4_1^+ \rightarrow 2_1^+$	0.2828(21)	0.3134(234)	0.4217(846)	_	0.3208(90)	0.2414(258)
$6_1^+ \rightarrow 4_1^+$	0.3415(34)	_	0.3874(1660)	_	0.3183(100)	_
$8_1^+ \rightarrow 6_1^+$	_	_	0.2664(362)	_	_	_
$0_2^+ \rightarrow 2_1^+$	_	_	_	_	_	0.07229(82)

Table 3: Experimental B(E2) values (in units e^2b^2) used in the calculations of e_b for the ^{104}Zr [41] [39] [40] .

Nucleus	J^π	E_1	E_2	E_3	Nucleus	J^π	E_1	E_2	E_3
^{110}Pd	0^+	0	947						
(N=9)	2^+	374	813	1214					
	3^+	1212							
	4^+	0921	1398						
	5^+								
	6^+	1574	2061						
	7^+								
	8^+								
	9^+								
	10^+								
^{108}Ru	0^+	0	976		^{104}Ru	0^+	0	988	
(N=10)	2^+	242	710	1249	(N= 8)	2^+	358	893	
	3^+	975				3^+	1242		
	4^+	665	1068			4^+	888	1503	2080
	5^+					5^+	1872		
	6^+	1240	1761			6^+	1556	2196	
	8^+					8^+	2320		
	10^+					10^+	3112		
^{106}Mo	0^+	0	956		^{104}Mo	0^+	0	886	
(N=11)	2^+	171	710	1150	(N= 10)	2^+	192	812	
	3^+	885				3^+	1028		
	4^+	522	1068			4^+	561	1215	1583
	5^+					5^+	1476		
	6^+	1033	1563			6^+	1080	1724	
	8^+					8^+	1722		
	10^+					10^+	2455		
^{104}Zr	0^+	0			^{104}Zr	0^+	0		
(N=12)	2^+	139			(N=12)	2^+	139		
	3^+					3^+			
	4^+	452				4^+	452		
	5^+					5^+			
	6^+	926				6^+	926		

Table 4: Experimental energies (in keV) for levels in neutron-rich A=104 isobaric and N=64 isotonic chains [41] [39] [40] used in the characterization of the parameters for ^{104}Zr.

	$\hat{n_d}$	$\hat{P}^\dagger\hat{P}$	$\hat{Q}^\chi\hat{Q}^\chi$	$\hat{L}\hat{L}$	$\hat{T}_3\hat{T}_3$	$\hat{T}_4\hat{T}_4$	$\hat{n_d}^2$	$\Delta(E)_N$ (keV)	$\Delta(E2)_N$ (me^2b^2)	$\Delta(E)_A$ (keV)	$\Delta(E2)_A$ (me^2b^2)
1	X	X	X			X		104	112		
2	X	X	X	X				133	100		
3	X	X	X		X			80	84	76	80
4	X	X		X	X			273	320		
5	X	X		X		X		357	328		
6	X	X			X	X		102	103	106	-
7	X		X	X	X			79	83	67	78
8	X		X	X		X		129	108		
9	X		X		X	X		80	83	73	84
10	X			X	X	X		193	184		
11		X	X	X		X		167	124		
12		X	X	X	X			192	118		
13		X		X	X	X		164	113		
14			X	X	X	X		169	88		
15		X	X		X	X		142	196		
16	X	X	X				X	143	108		
17	X	X		X			X	147	120		
18	X	X			X		X	157	128		
19	X		X	X			X	80	90	54	80
20	X		X		X		X	79	84	63	73
21	X			X	X		X	193	184		
22		X	X	X			X	250	231		
23		X		X	X		X	251	217		
24			X	X	X		X	250	231		
25		X	X		X		X	242	230		

Table 5: The root mean square values obtained by fitting different Hamiltonians. From left to right: the first column assigns a number to each Hamiltonian; columns two to the eight indicate which terms of the general Hamiltonian are considered in a particular calculation; finally, the last four columns show the root mean square for the energy levels and B(E2) values, the first two for the isobaric (A=104) chain and the last two for the isotonic (N=64) chain.

	Isobars (A=104)				
Transition	H_3	H_7	H_9	H_{19}	H_{20}
B[E2; 2(1)–> 0(1)]	0.3297	0.3384	0.3192	0.3569	0.3558
B[E2; 4(1)–> 2(1)]	0.4797	0.4863	0.4641	0.4974	0.5078
B[E2; 6(1)–> 4(1)]	0.5326	0.5330	0.5158	0.5241	0.5516
B[E2; 0(2)–> 2(2)]	0.2731	0.2011	0.2698	0.0717	0.1583
B[E2; 4(2)–> 2(2)]	0.2008	0.1854	0.1933	0.1688	0.1870
B[E2; 6(2)–> 4(2)]	0.3656	0.3524	0.3555	0.3138	0.3554
B[E2; 0(3)–> 2(3)]	0.0271	0.0277	0.0206	0.0004	0.0279
B[E2; 2(3)–> 0(3)]	0.0054	0.0055	0.0041	0.0001	0.0056
B[E2; 4(3)–> 2(3)]	0.0962	0.2659	0.0788	0.3147	0.3506
B[E2; 6(3)–> 4(3)]	0.2270	0.3167	0.2124	0.3160	0.3741
B[E2; 2(2)–> 0(1)]	0.0222	0.0218	0.0226	0.0114	0.0205
B[E2; 0(2)–> 2(1)]	0.0310	0.0165	0.0244	0.0034	0.0117
B[E2; 4(2)–> 2(1)]	0.0071	0.0090	0.0074	0.0040	0.0093
B[E2; 6(2)–> 4(1)]	0.0044	0.0065	0.0044	0.0024	0.0074
B[E2; 2(3)–> 0(2)]	0.2244	0.2380	0.2212	0.2404	0.2509
B[E2; 0(3)–> 2(2)]	0.0014	0.0011	0.0014	0.0108	0.0003
B[E2; 4(3)–> 2(2)]	0.0442	0.0215	0.0466	0.0009	0.0039
B[E2; 6(3)–> 4(2)]	0.0122	0.0092	0.0121	0.0018	0.0044
B[E2; 2(3)–> 0(1)]	0.0016	0.0007	0.0016	0.0024	0.0003
B[E2; 0(3)–> 2(1)]	0.0000	0.0000	0.00007	0.0099	0.0004
B[E2; 4(3)–> 2(1)]	0.0003	0.0001	0.0002	0.0046	0.000005
B[E2; 6(3)–> 4(1)]	0.0001	0.0000	0.0001	0.0065	0.00005
B[E2; 2(2)–> 0(3)]	0.0003	0.0002	0.0003	0.0021	0.00007
B[E2; 4(2)–> 2(3)]	0.0225	0.0189	0.0231	0.0119	0.0161
B[E2; 6(2)–> 4(3)]	0.0009	0.0069	0.0008	0.0084	0.0085
B[E2; 2(3)–> 4(2)]	0.0405	0.0341	0.0415	0.0215	0.0290

Table 6: Experimental and theoretical B(E2) values (in units of e^2b^2) for transitions in ^{104}Zr. The table shows the results calculated by fitting the parameters to the isobaric chain. A value of $e_b = 0.1$ has been used in all the cases.

	Isotones (N=64)				
Transition	H_3	H_7	H_9	H_{19}	H_{20}
B[E2; 2(1)–> 0(1)]	0.3508	0.3473	0.3399	0.2592	0.3499
B[E2; 4(1)–> 2(1)]	0.4932	0.4881	0.4781	0.3564	0.4929
B[E2; 6(1)–> 4(1)]	0.5248	0.5189	0.5090	0.3654	0.5253
B[E2; 0(2)–> 2(2)]			0.0466	0.0069	0.0071
B[E2; 2(2)–> 0(2)]	0.0026	0.0016			
B[E2; 4(2)–> 2(2)]	0.1667	0.1071	0.1628	0.0884	0.1593
B[E2; 6(2)–> 4(2)]	0.3038	0.1564	0.2997	0.1630	0.2394
B[E2; 2(3)–> 0(3)]	0.1292	0.0899	0.0107	0.0367	0.1117
B[E2; 4(3)–> 2(3)]	0.0859	0.0387	0.2769	0.0493	0.0475
B[E2; 6(3)–> 4(3)]	0.0196	0.0033	0.2412	0.0008	0.0007
B[E2; 2(2)–> 0(1)]	0.0158	0.0151	0.0161	0.0039	0.0159
B[E2; 0(2)–> 2(1)]	0.00002	0.000004	0.0009	0.0009	0.000002
B[E2; 4(2)–> 2(1)]	0.0110	0.0070	0.0121	0.0012	0.0102
B[E2; 6(2)–> 4(1)]	0.0112	0.0087	0.0126	0.0010	0.0091
B[E2; 2(3)–> 0(2)]	0.0569	0.0310	0.2043	0.0777	0.0316
B[E2; 0(3)–> 2(2)]	0.0388	0.0360	0.0028	0.0143	0.0450
B[E2; 4(3)–> 2(2)]	0.0018	0.0564	0.0015	0.0012	0.0081
B[E2; 6(3)–> 4(2)]	0.0003	0.0488	0.0044	0.0002	0.0395
B[E2; 2(3)–> 0(1)]	0.00003	0.0000	0.00002	0.0017	0.000001
B[E2; 0(3)–> 2(1)]	0.0006	0.0008	0.0003	0.0823	0.0016
B[E2; 4(3)–> 2(1)]	0.0002	0.0039	0.0004	0.00006	0.0006
B[E2; 6(3)–> 4(1)]	0.0001	0.0010	0.0009	0.000001	0.0007
B[E2; 2(2)–> 0(3)]	0.0078	0.0072	0.0006	0.0028	0.0090
B[E2; 4(2)–> 2(3)]	0.0021	0.0093	0.0024	0.0063	0.00002
B[E2; 6(2)–> 4(3)]	0.0008	0.0612	0.0004	0.0003	0.0067
B[E2; 2(3)–> 4(2)]	0.0037	0.0168	0.0043	0.0114	0.00004

Table 7: Experimental and theoretical B(E2) values (in units of e^2b^2) for transitions in ^{104}Zr. The table shows the results calculated by fitting the parameters to the isotonic chain. A value of $e_b = 0.1$ has been used in all the cases.

Transition	^{112}Pd	^{110}Ru	^{108}Mo	^{106}Zr	^{106}Mo	^{106}Ru
$2_1^+ \rightarrow 0_1^+$	0.1310(22)	0.2197(137)	0.4276(256)	_	0.3059(1)	0.1976(29)
$4_1^+ \rightarrow 2_1^+$	_	0.2291(211)	_	_	0.4217(84)	_
$6_1^+ \rightarrow 4_1^+$	_	0.3743(155)	_	_	0.3875(160)	_
$8_1^+ \rightarrow 6_1^+$	_	_	_	_	0.2664(361)	_

Table 8: Experimental B(E2) values (in units e^2b^2) used in the (A=104) isobaric and isotonic (N=64) chains calculations [41] [39] [40] for the ^{106}Zr.

Nucleus	J^π	E_1	E_2	E_3	Nucleus	J^π	E_1	E_2	E_3
^{112}Pd	0^+	0							
(N=10)	2^+	348	736						
	3^+	1096							
	4^+	883	1362						
	5^+	1759							
	6^+	1550	2002						
	7^+	2483							
	8^+	2318							
	9^+	3085							
	10^+	3049							
^{110}Ru	0^+	0			^{106}Ru	0^+	0	991	
(N=11)	2^+	241	613		(N= 9)	2^+	270	792	1392
	3^+	860				3^+	1092		
	4^+	663	1084			4^+	715	1307	
	5^+	1375				5^+	1641		
	6^+	1239	1684			6^+	1296	1908	
	7^+	2021				7^+	2284		
	8^+	1945	2397			8^+	1973	2960	
	9^+	2777				9^+			
	10^+	2759	3225			10^+	2705		
^{108}Mo	0^+	0			^{106}Mo	0^+	0	956	
(N=12)	2^+	193	586		(N= 11)	2^+	171	710	1150
	3^+	783				3^+	885		
	4^+	564	978			4^+	522	1068	
	5^+	1232				5^+	1307		
	6^+	1090	1508			6^+	1033	1563	
	7^+	1817				7^+	1868		
	8^+	1753	2170			8^+	1688	2194	
	9^+	2524				9^+			
	10^+	2529	2950			10^+	2474		
^{106}Zr	0^+	0			^{106}Zr	0^+	0		
(N=13)	2^+	152	607		(N=13)	2^+	152	607	
	3^+					3^+			
	4^+	476				4^+	476		

Table 9: Experimental energies (in keV) for levels in neutron-rich A=106 isobaric and N=66 isotonic chains [41] [39] [40] used in the characterization of the parameters for ^{106}Zr.

	$\hat{n_d}$	$\hat{P}^\dagger\hat{P}$	$\hat{Q}^\chi\hat{Q}^\chi$	$\hat{L}\hat{L}$	$\hat{T}_3\hat{T}_3$	$\hat{T}_4\hat{T}_4$	$\hat{n_d}^2$	$\Delta(E)_N$ (keV)	$\Delta(E2)_N$ (me^2b^2)	$\Delta(E)_A$ (keV)	$\Delta(E2)_A$ (me^2b^2)
1	X	X	X			X		73	145	109	165
2	X	X	X	X				68	143	88	138
3	X	X	X		X			64	148	86	152
4	X	X		X	X			84	145	130	145
5	X	X		X		X		82	163		
6	X	X			X	X		81	164		
7	X		X	X	X			62	145	87	150
8	X		X	X		X		92	155		
9	X		X		X	X		56	166	89	149
10	X			X	X	X		196	168		
11		X	X	X		X		175	179		
12		X	X	X	X			232	260		
13		X		X	X	X		88	156		
14			X	X	X	X		71	159		
15		X	X		X	X		171	270		
16	X	X	X				X	279	266		
17	X	X		X			X	83	161		
18	X	X			X		X	85	140	128	140
19	X		X	X			X	53	164	98	121
20	X		X		X		X	61	142	87	151
21	X			X	X		X	169	168		
22		X	X	X			X	236	160		
23		X		X	X		X	246	267		
24			X	X	X		X	223	149		
25		X	X		X		X	239	145		

Table 10: The root mean square values obtained by fitting different Hamiltonians. From left to right: the first column assigns a number to each Hamiltonian; columns two to the eight indicate which terms of the general Hamiltonian are considered in a particular calculation; finally, the last four columns show the root mean square for the energy levels and B(E2) values, the first two for the isobaric (A=106) chain and the last two for the isotonic (N=66) chain.

J^π	E_{exp}	E_{H3}	E_{H7}	E_{H9}
2^+	174	132	151	208
4^+	522	435	470	580
6^+	1000	899	940	1091
8^+	1642	1517	1550	1725

Table 11: Experimental [17] and theoretical energy levels (in keV) ^{108}Zr.

Transition	Isobars (A=106)					
	H_2	H_3	H_7	H_9	H_{19}	H_{20}
B[E2; 2(1)–> 0(1)]	0.2708	0.3353	0.3273	0.3211	0.2066	0.3302
B[E2; 4(1)–> 2(1)]	0.3814	0.4767	0.4656	0.4574	0.2856	0.4697
B[E2; 6(1)–> 4(1)]	0.4086	0.5182	0.5059	0.4982	0.2970	0.5102
B[E2; 0(2)–> 2(2)]	0.1436	0.1314	0.1124	0.1224	0.0095	0.1130
B[E2; 4(2)–> 2(2)]	0.1452	0.1744	0.1685	0.1662	0.0747	0.1702
B[E2; 6(2)–> 4(2)]	0.2768	0.3383	0.3264	0.3239	0.1327	0.3293
B[E2; 0(3)–> 2(3)]	0.0005	0.0154	0.0201	0.0227	0.0149	0.0200
B[E2; 2(3)–> 0(3)]	0.0001	0.0031	0.0040	0.0045	0.0030	0.0040
B[E2; 4(3)–> 2(3)]	0.2955	0.3241	0.3346	0.3285	0.0194	0.3372
B[E2; 6(3)–> 4(3)]	0.3109	0.3498	0.3611	0.3580	0.0049	0.3632
B[E2; 2(2)–> 0(1)]	0.0277	0.0184	0.0179	0.0185	0.0017	0.0178
B[E2; 0(2)–> 2(1)]	0.0001	0.0037	0.0057	0.0064	0.0017	0.0057
B[E2; 4(2)–> 2(1)]	0.0137	0.0083	0.0091	0.0092	0.0009	0.0089
B[E2; 6(2)–> 4(1)]	0.0098	0.0058	0.0072	0.0069	0.0004	0.0071
B[E2; 2(3)–> 0(2)]	0.2124	0.2418	0.2349	0.2297	0.0607	0.2372
B[E2; 0(3)–> 2(2)]	0.00001	0.0004	0.0005	0.0010	0.0164	0.0004
B[E2; 4(3)–> 2(2)]	0.0011	0.0059	0.0012	0.0017	0.0001	0.0012
B[E2; 6(3)–> 4(2)]	0.0027	0.0049	0.0024	0.0027	0.0001	0.0025
B[E2; 2(3)–> 0(1)]	0.000002	0.0002	0.0003	0.0004	0.00001	0.0002
B[E2; 0(3)–> 2(1)]	0.00002	0.00001	0.0001	0.00003	0.0914	0.0002
B[E2; 4(3)–> 2(1)]	0.00003	0.0001	0.00005	0.0001	0.00002	0.00004
B[E2; 6(3)–> 4(1)]	0.0001	0.00001	0.00000	0.00002	0.0000	0.000003
B[E2; 2(2)–> 0(3)]	0.000001	0.0001	0.0001	0.0002	0.0033	0.0001
B[E2; 4(2)–> 2(3)]	0.0195	0.0172	0.0135	0.0148	0.0000	0.0136
B[E2; 6(2)–> 4(3)]	0.0166	0.0116	0.0087	0.0099	0.0010	0.0087
B[E2; 2(3)–> 4(2)]	0.0351	0.0310	0.0243	0.0267	0.0000	0.0244

Table 12: Calculated B(E2) values (in units of e^2b^2) for transitions in ^{106}Zr. The table shows the calculations made with the isobaric chain data. A value of $eb = 0.09$ eb was used in all the cases.

	Isotones (N=66)					
Transition	H_2	H_3	H_7	H_9	H_{19}	H_{20}
B[E2; 2(1)–> 0(1)]	0.2360	0.3015	0.2829	0.3579	0.3522	0.2628
B[E2; 4(1)–> 2(1)]	0.3433	0.4396	0.4173	0.5028	0.4949	0.3920
B[E2; 6(1)–> 4(1)]	0.3754	0.4883	0.4642	0.5350	0.5262	0.4397
B[E2; 0(2)–> 2(2)]		0.2301	0.1697	0.0764		0.1854
B[E2; 2(2)–> 0(2)]	0.0322				0.0212	
B[E2; 4(2)–> 2(2)]	0.1401	0.1789	0.1591	0.1781	0.1846	0.1515
B[E2; 6(2)–> 4(2)]	0.2556	0.3271	0.2985	0.3281	0.3328	0.2861
B[E2; 0(3)–> 2(3)]	0.0312	0.0278	0.0180	0.0108	0.000001	0.0521
B[E2; 2(3)–> 0(3)]	0.0062	0.0056	0.0036	0.0022	0.0000	0.0104
B[E2; 4(3)–> 2(3)]	0.2527	0.1696	0.0034	0.3257	0.3262	0.2850
B[E2; 6(3)–> 4(3)]	0.2578	0.2245	0.0012	0.2800	0.3394	0.3061
B[E2; 0(2)–> 2(1)]	0.0298	0.0232	0.0399	0.0021	0.0038	0.0458
B[E2; 4(2)–> 2(1)]	0.0144	0.0075	0.0100	0.0054	0.0055	0.0106
B[E2; 6(2)–> 4(1)]	0.0120	0.0067	0.0099	0.0039	0.0035	0.0106
B[E2; 2(3)–> 0(2)]	0.1761	0.2211	0.2015	0.2430	0.2334	0.1935
B[E2; 0(3)–> 2(2)]	0.0012	0.000001	0.00001	0.0088	0.0532	0.0003
B[E2; 4(3)–> 2(2)]	0.0048	0.0348	0.00001	0.0007	0.0015	0.0067
B[E2; 6(3)–> 4(2)]	0.0053	0.0105	0.0008	0.0016	0.0018	0.0064
B[E2; 2(3)–> 0(1)]	0.0001	0.0003	0.0002	0.0009	0.0013	0.0003
B[E2; 0(3)–> 2(1)]	0.0011	0.0003	0.0004	0.0011	0.0011	0.0011
B[E2; 4(3)–> 2(1)]	0.0001	0.000001	0.0000	0.0031	0.0055	0.00001
B[E2; 6(3)–> 4(1)]	0.0005	0.0001	0.00005	0.0037	0.0090	0.0003
B[E2; 2(2)–> 0(3)]	0.0002	0.0000	0.0000	0.0018	0.0106	0.0001
B[E2; 4(2)–> 2(3)]	0.0081	0.0168	0.0077	0.0095	0.0096	0.0076
B[E2; 6(2)–> 4(3)]	0.0032	0.0010	0.0001	0.0054	0.0044	0.0013
B[E2; 2(2)–> 0(2)]	0.0322	0.0460	0.0339	0.0153	0.0212	0.0371
B[E2; 2(3)–> 4(2)]	0.0147	0.0302	0.0138	0.0171	0.0173	0.0136

Table 13: Calculated B(E2) values (in units of e^2b^2) for transitions in ^{106}Zr. The table shows the calculations made with the isotonic chain data. A value of $eb = 0.09$ eb was used in all the cases.

References

[1] O. Haxel *et al.*, Phys. Rev. **75**, 1766 (1949). 1

[2] B. Bastin *et al.*, Phys. Rev. Lett. **99, No. 2**, 022503 (2007). 2

[3] L. Gaudefroy *et al.*, Phys. Rev. Lett. **102, No. 9**, 092501 (2009). 2

[4] S. Grevy *et al.*, Phys. Lett. **B, No. 594**, 252 (2004). 2

[5] A. Bohr and B. R. Mottelson, K. Dan. Vidensk. Selsk. Mat-Fys. **27**, 16 (1953). 2, 5

[6] F. Iachello and A. Arima, Phys. Rev. Lett **35**, 1069 (1975). 2, 19

[7] M. B*öyü*kata, P. V. Isacker, and *İ*. Uluer, J. Phys. G **C, No. 37**, 105102 (2010). 2, 19, 25

[8] R. F. Casten and J. Cisewski, Nucl. Phys. **A, 309**, 477 (1978). 2, 18

[9] O. Scholten *et al.*, Ann. Phys. NY. **115**, 321 (1978). 2, 18

[10] C. Hutter *et al.*, Phys. Rev. **C, 67**, 054315 (2003). 2, 18, 19

[11] F. C. Charlwood *et al.*, Phys. Lett. B **674**, 23 (2009). 3, 16, 17

[12] R. Rodríguez-Guzmán *et al.*, Phys. Lett. **B, 691**, 202 (2010). 3

[13] H. Mach *et al.*, Nucl. Phys. **A, 523**, 197 (1991). 3

[14] C. Goodin *et al.*, Nucl. Phys. **A, 787**, 231 (2007). 3

[15] W. Urban *et al.*, Nucl. Phys. **A, 689**, 605 (2001). 3

[16] H. Hua *et al.*, Phys. Rev. **C, No. 69**, 014317 (2004). 3, 49

[17] D. Kameda *et al.*, Phys. Rev. C **86** (2012). 3, 45, 46, 48, 98

[18] C. Rodríguez-Triguero *et al.*, J. Phys. G. **39**, 015101 (2012). 3, 49, 87

[19] P. Walker and G. Dracoulis, Nature **399**, 35 (2005). 3

[20] T. Sumikama, Acta Phys. Pol. B **44, No. 3** (2013). 3, 47

[21] A. M. Bruce *et al.*, J. Phys. G **381**, 012053 (2012). 3, 49

[22] J. Skalsky *et al.*, Nucl. Phys. **A, No. 617**, 282 (1997). 3, 11, 16

[23] T. Eronen *et al.*, Nucl. Inst. Meth. **B, No. 266**, 4527 (2008). 3, 49, 52, 54, 57

[24] T. S. et al, Phy. Rev. **106, No. 20** (2011). 3

[25] N. Bohr and F. Kalckar, K. Dan. Vidensk. Selsk. Mat-Fys. **14**, 10 (1937). 4

[26] J. Rainwatter, Phys. Rev. **79**, 432 (1950). 5

[27] A. Bohr, K. Dan. Vidensk. Selsk. Mat-Fys. **26**, 14 (1952). 5

[28] M. A. Preston and R. Bhaduri, *Structure of the Nucleus* (Addison-Wesley Publishing Company, Reading, Massachusetts, 1975). 5

[29] W. Greiner and J. A. Maruhn, *Nuclear Models* (Springer, Berlin Heidelberg, 1996). 9

[30] A. Bohr and B. R. Mottelson, *Nuclear Structure* (World Scientific, Singapore, 1975). 9

[31] `http://www.nndc.bnl.gov/`, Accesed: May 2012. 11

[32] L. Grodzins, Phys. Lett. **2, No. 2**, 88 (1962). 13

[33] W. D. Hamilton, *The Electromagnetic Interaction In Nuclear Spectroscopy* (North-Holland Publishing Company, Amsterdam, Oxford, 1975). 14

[34] R. F. Casten, *Nuclear Structure from a Simple Perspective* (Oxford University Press, New York, 1990). 14, 15, 23

[35] D. Abriola and A. A. Sonzogni, N. Data Sheets **109**, 2501 (2008). 15

[36] B. Singh and Z. Hu, N. Data Sheets **98**, 335 (2003). 15

[37] B. Singh, N. Data Sheets **109**, 297 (2008). 15, 56, 57, 62, 63, 64, 65, 68, 69

[38] D. D. Frenne, N. Data Sheets **110**, 1745 (2009). 15, 24, 26

[39] D. D. Frenne and A. Negret, N. Data Sheets **109**, 943 (2008). 15, 24, 26, 91, 92, 96, 97

[40] J. Blachot, N. Data Sheets **90**, 135 (2000). 15, 24, 26, 91, 92, 96, 97

[41] D. D. Frenne and E. Jacobs, N. Data Sheets **89**, 481 (2000). 15, 91, 92, 96, 97

[42] B. Cheal *et al.*, Phys. Lett. B **645**, 133 (2007). 16, 17

[43] M. Keim *et al.*, Nucl. Phys. A **586**, 219 (1995). 16, 17

[44] C.Thibault *et al.*, Phys. Rev. C **23**, 2720 (1981). 16, 17

[45] F.Buchinger *et al.*, Phys. Rev. C **41**, 2883 (1990). 16, 17

[46] P. Lievens *et al.*, Phys. Lett. B **256**, 141 (1991). 16, 17

[47] P. Campbell *et al.*, Phys. Rev. Lett. **89**, 082501 (2002). 16, 17

[48] R. J. Chasman, Z. Phys. **A, No. 339**, 111 (1991). 17

[49] F. R. Xu *et al.*, Phys. Rev. **C, No. 65**, 021303(R) (2002). 17, 47

[50] P. V. Isacker and G. Puddu, Nucl. Phys **A, No. 29**, 125 (1980). 19

[51] S. Lalkovski and P. V. Isacker, Phys. Rev. **C, No. 79**, 044307 (2009). 19, 23, 25

[52] F. Iachello and A. Arima, *The interacting Boson Model* (Cambridge University Press, New York, New Rochelle, Melbourne, Sydney, 1987). 19, 21

[53] D. D. Warner and R. F. Casten, Rev. Mod. Phys. **60**, 398 (1988). 20, 22

[54] X.-W. Pang *et al.*, Phys. Lett. **B, 287**, 1 (1992). 21

[55] D. D. Warner and R. F. Casten, Phys. Rev. C **28**, 1798 (1983). 21

[56] Y. Shi *et al.*, Phys. Rev.C **85** (2012). 47

[57] J. C. Hill *et al.*, Phys. Rev. **C, No. 43**, 2591 (1991). 49

[58] K. Shizuma *et al.*, Phys. Rev. **C, No. 27**, 2869 (1983). 49

[59] T. A. Khan *et al.*, Nucl. Phys. **A, No. 205**, 488 (1973). 49

[60] Cheifetz *et al.*, Phys. Rev. **C, No. 4**, 1913 (1971). 49

[61] J. L. Durell *et al.*, Phys. Rev. **C, No. 52**, R2306 (1995). 49

[62] S. Rinta-Antila, PhD thesis, University of *Jyväskylä*, 2006. 50

[63] J. *Äystö*, Nucl. Inst. Meth. **A, No. 693**, 477 (2001). 50

[64] P. Karvonen *et al.*, Nucl. Instrum. Methods B **No. 266**, 4794 (2008). 50, 52, 72, 77

[65] A. Nieminen *et al.*, Nucl. Inst. Meth. **A, No. 469**, 244 (2001). 51, 52, 73

[66] V. S. Kolhinon *et al.*, Nucl. Inst. Meth. **A, No. 528**, 776 (2004). 51, 52, 53, 73

[67] N. F. Ramsey, Rev. Mod. Phys. **62**, 3 (1990). 51, 54

[68] Igisol group, 2012, University of *Jyväskylä*. 51, 72

[69] G. Savard *et al.*, Phys. Lett. **A, No. 158**, 247 (1991). 52, 53

[70] L. S. Brown and G. Gabrielse, Rev. Mod. Phys. **58, No. 1**, 233 (1986). 53

[71] T. Eronen, PhD thesis, University of *Jyväskylä*, 2008. 54

[72] V. A. Rubchenya, Phys. Rev. C **75**, 054601 (2007). 54

[73] A. M. Bruce, Private comunication 2013. 55

[74] S. Rinta-Antila *et al.*, Eur. Phys. **A, No. 31**, 1 (2007). 56, 61

[75] G. Menzen *et al.*, Z. Phys. **A, No. 327**, 119 (1987). 56, 61, 69

[76] J. Suhonen and G. Lhersonneau, Phys. Rev. **C, No. 64**, 014315 (2001). 62, 63, 64, 65

[77] W. R. Leo, *Techniques for Nuclear and Particle Physics Experiments. A How to Approach* (Springer-Verlag, Berlin, Heidelberg, New York, 1987). 66

[78] `https://www.jyu.fi/fysiikka/en/research/accelerator/accelerator/index_html/mcc30`, Accesed: March 2013. 71

[79] H. Penttilä *et al.*, J. Korean Phys. Soc. **59, No. 2**, 1589 (2010). 71, 73

[80] P. Karvonen *et al.*, Eur. Phys. J-Spec. Top. **102**, 283 (2007). 72

[81] M. Reponen *et al.*, Nucl. Instrum. Methods A **635**, 24 (2011). 73

[82] V.-V. Elomaa *et al.*, Nucl. Instrum. Methods B **266**, 4425 (2008). 73

[83] B. Cheal *et al.*, Phys. Rev. Lett. **102**, 222501 (2009). 73

[84] J. Huikari, PhD thesis, University of *Jyväskylä*, 2003. 75, 76, 77, 78

[85] P. Karvonen, PhD thesis, University of *Jyväskylä*, 2010. 82

[86] V. Kolhinen *et al.*, Nucl. Instrum. Methods B (2013), To be published. 84, 85

[87] I. D. Moore *et al.*, Nucl. Instrum. Methods B (2013), To be published. 84

[88] M. Reponen *et al.*, Nucl. Instrum. Methods B (2013), To be published. 84